

Measuring Trapped Ion Qudits

by

Brendan Bramman

A thesis
presented to the University of Waterloo
in fulfillment of the
thesis requirement for the degree of
Master of Science
in
Physics - Quantum Information

Waterloo, Ontario, Canada, 2019

© Brendan Bramman 2019

Author's Declaration

I hereby declare that I am the sole author of this thesis. This is a true copy of the thesis, including any required final revisions, as accepted by my examiners.

I understand that my thesis may be made electronically available to the public.

Abstract

Quantum information has typically focused on using 2-level qubits to perform simulation and computation. We propose to expand the number of levels for computation using qudits, where $d > 2$. Doing so could be a viable option for making trapped ion systems scalable for quantum computation. Our group in particular will use Barium ions because of some energy features and convenient laser wavelengths. This thesis presents much of the necessary background needed to work with Barium as a qudit for quantum computation. Energy structure, branching ratios, and saturation intensities are derived and presented. In addition, a method for selecting different isotopes of Barium for trapping is discussed. A method for measuring out the state of a Barium qudit is presented, with error rates estimated to be under 1% for up to 5-level qudits. Finally, various optics projects which were necessary for building up our first ion trap are outlined.

Acknowledgements

Thank you to my supervisor, Dr. Crystal Senko, for bringing me into the group and giving me the chance to build an ion trap and become a better scientist in the process. Thank you to all of the team members in both Senkolab and Dr. Rajibul Islam's group, QITlab, for helping build up the trap and having good conversations about the physics. Thank you to my family, especially my step-dad, Keith White, for being a step above as a father (forgive me for the pun). Finally, thank you to my roommates, Andy Ding and Noah Greenberg, for all of the movie nights and memories.

Table of Contents

List of Figures	vii
List of Tables	ix
1 Introduction	1
2 Barium Ions	3
2.1 Energy Structure	3
2.2 Transition Branching Ratios/Strengths	14
2.2.1 Dipole Transitions	19
2.2.2 Quadrupole Transitions	22
2.3 Saturation Intensity	28
2.4 Isotope Selectivity	30
3 Qudit Measurement	33
3.1 Shelving	33
3.2 Errors	37
4 Four-Rod Paul Trap Optics	42
4.1 Lasers and Optics	42
4.1.1 Lasers	42

4.1.2 Optics Paths	43
4.2 Frequency Locking	50
4.3 RF sources	52
5 Conclusion	54
References	56
A Appendix	61
A.1 Dipole Transition Branching Ratios/Strengths	61
A.2 Quadrupole Transition Branching Ratios/Strengths	68

List of Figures

1.1	Qubit vs qudit encoding	2
2.1	Hydrogen energy structure	4
2.2	Thomas precession	6
2.3	$^{137}\text{Ba}^+$ energy structure	8
2.4	$^{137}\text{Ba}^+$ $6S_{1/2}$ level hyperfine splitting with magnetic field	12
2.5	$^{137}\text{Ba}^+$ $5D_{5/2}$ state hyperfine splitting with magnetic field	13
2.6	Quadrupole transition laser orientation	23
2.7	Quadrupole geometrical constants	25
2.8	Quadrupole useful orientations	25
2.9	Natural barium transition spectrum	32
3.1	Shelving procedure	34
3.2	Adiabatic passage	36
3.3	Adiabatic passage triangle	36
3.4	Shelving adiabatic passage and measurement error	38
4.1	Overall beam paths	44
4.2	EOM transition frequencies	45
4.3	Lasers enclosure	46
4.4	493 nm optics enclosure picture	47

4.5	493 nm enclosure	48
4.6	650 nm and 553 nm enclosures	49
4.7	Frequency locking setup	50
4.8	Wavelength meter frequency locking	51
4.9	PLL frequency sources	53
5.1	We were able to trap $^{137}\text{Ba}^+$ with our four-rod trap! It took a lot of brainstorming and stabbing in the dark to overcome many challenges along the way, but we finally managed to trap ions! This is all thanks to the concerted effort of everybody in Senkolab - especially those that helped with the bring-up of the four-rod trap including Pei Jiang Low, Rich Rademacher, Noah Greenberg, and Matthew Day. Acknowledgement is also owed to Nigel Anderson and of course our PI Dr. Crystal Senko, who helped us in coming up with new directions when we inevitably found ourselves fumbling around in the dark.	55

List of Tables

2.1	Characteristics of $^{137}\text{Ba}^+$	9
2.2	Block form atomic hamiltonian	10
2.3	$^{135}\text{Ba}^+ / ^{137}\text{Ba}^+$ dipole branching ratios: $6S_{1/2} \leftrightarrow 6P_{1/2}, q = +1$	21
2.4	$^{135}\text{Ba}^+ / ^{137}\text{Ba}^+$ dipole branching ratios: $6S_{1/2} \leftrightarrow 6P_{1/2}, q = -1$	21
2.5	$^{135}\text{Ba}^+ / ^{137}\text{Ba}^+$ dipole branching ratios: $6S_{1/2} \leftrightarrow 6P_{1/2}, q = 0$	22
2.6	$^{135}\text{Ba}^+ / ^{137}\text{Ba}^+$ quadrupole branching ratios: XZ orientation	27
2.7	Neutral barium ionization energy levels	31
2.8	Ionization selectivity	32
3.1	Shelving transitions	35
4.1	Wavelength meter PID settings	51
A.1	$^{133}\text{Ba}^+$ dipole branching ratios: $6S_{1/2} \leftrightarrow 6P_{1/2}, q = +1$	61
A.2	$^{133}\text{Ba}^+$ dipole branching ratios: $6S_{1/2} \leftrightarrow 6P_{1/2}, q = -1$	61
A.3	$^{133}\text{Ba}^+$ dipole branching ratios: $6S_{1/2} \leftrightarrow 6P_{1/2}, q = 0$	62
A.4	$^{133}\text{Ba}^+$ dipole branching ratios: $6S_{1/2} \leftrightarrow 6P_{3/2}, q = +1$	62
A.5	$^{133}\text{Ba}^+$ dipole branching ratios: $6S_{1/2} \leftrightarrow 6P_{3/2}, q = -1$	62
A.6	$^{133}\text{Ba}^+$ dipole branching ratios: $6S_{1/2} \leftrightarrow 6P_{3/2}, q = 0$	63
A.10	$^{135}\text{Ba}^+ / ^{137}\text{Ba}^+$ dipole branching ratios: $6S_{1/2} \leftrightarrow 6P_{3/2}, q = +1$	66
A.11	$^{135}\text{Ba}^+ / ^{137}\text{Ba}^+$ dipole branching ratios: $6S_{1/2} \leftrightarrow 6P_{3/2}, q = -1$	67

A.12	$^{135}\text{Ba}^+ / ^{137}\text{Ba}^+$ dipole branching ratios: $6S_{1/2} \leftrightarrow 6P_{3/2}$, $q = 0$	68
A.13	$^{133}\text{Ba}^+$ quadrupole branching ratios: $6S_{1/2} \leftrightarrow 5D_{3/2}$ averaged	69
A.14	$^{133}\text{Ba}^+$ quadrupole branching ratios: $6S_{1/2} \leftrightarrow 5D_{5/2}$ averaged	69
A.15	$^{135}\text{Ba}^+ / ^{137}\text{Ba}^+$ quadrupole branching ratios: $6S_{1/2} \leftrightarrow 5D_{3/2}$ averaged	70
A.16	$^{135}\text{Ba}^+ / ^{137}\text{Ba}^+$ quadrupole branching ratios: $6S_{1/2} \leftrightarrow 5D_{5/2}$ averaged	71
A.17	$^{133}\text{Ba}^+$ quadrupole branching ratios: $6S_{1/2} \leftrightarrow 5D_{3/2}$ orthogonal orientation	72
A.18	$^{133}\text{Ba}^+$ quadrupole branching ratios: $6S_{1/2} \leftrightarrow 5D_{5/2}$ orthogonal orientation	72
A.19	$^{135}\text{Ba}^+ / ^{137}\text{Ba}^+$ quadrupole branching ratios: $6S_{1/2} \leftrightarrow 5D_{3/2}$ orthogonal orientation	73
A.20	$^{135}\text{Ba}^+ / ^{137}\text{Ba}^+$ quadrupole branching ratios: $6S_{1/2} \leftrightarrow 5D_{5/2}$ orthogonal orientation	74
A.21	$^{133}\text{Ba}^+$ quadrupole branching ratios: $6S_{1/2} \leftrightarrow 5D_{3/2}$ XZ orientation	75
A.22	$^{133}\text{Ba}^+$ quadrupole branching ratios: $6S_{1/2} \leftrightarrow 5D_{5/2}$ XZ orientation	75
A.23	$^{135}\text{Ba}^+ / ^{137}\text{Ba}^+$ quadrupole branching ratios: $6S_{1/2} \leftrightarrow 5D_{3/2}$ XZ orientation	76

CHAPTER 1

Introduction

For the past 30 years, we’ve seen quantum information flourish and become one of the most active areas of modern physics. Quantum computers and simulators of today are just starting to get to a point where they can solve some interesting problems. It’s recently been shown that an amount of just 50 qubits is enough to exceed the capabilities of classical computing for emulating physical systems [1], reaching the so-called “Quantum Supremacy” threshold. We’re beginning to see trapped ion systems with control over 50-100 ions [2, 3]. This amount of qubits can allow us to simulate interesting chemistry, or to investigate the behavior of solid-state systems better than classical computers. While they are already immediately useful for some problems, scaling up remains an immensely important issue to solve. The ultimate quantum information system will incorporate quantum error correction to allow us to do fully fault tolerant quantum computing. These error correction schemes tend to require much overhead; theoretically, arbitrary errors on a single logical qubit can be faithfully corrected using at least 5 extra physical qubits [4]. There is much emphasis on the “at least”, because in practice many more qubits than this are needed. There are many different approaches to take in attempting to scale up to qubit numbers more reasonable for error correction, such as shuttling ions to different positions in one dimension [5, 6] or two dimensions [7], or by connecting multiple ion traps together through photon buses [8]. In our group, the solution we explore is to utilize the higher Hilbert space afforded by ion energy structure; i.e. using qudits with $d > 2$ levels rather than qubits with just 2 levels.

As shown in Figure 1.1, the commonly used $I = 3/2$ hyperfine qubit has many more energy levels than the two used to define a qubit. Typically, steps are taken to essentially exclude these other states, so that only the energy levels of the qubit are occupied. We propose to take advantage of these energy levels, so that we can do more with fewer ions.

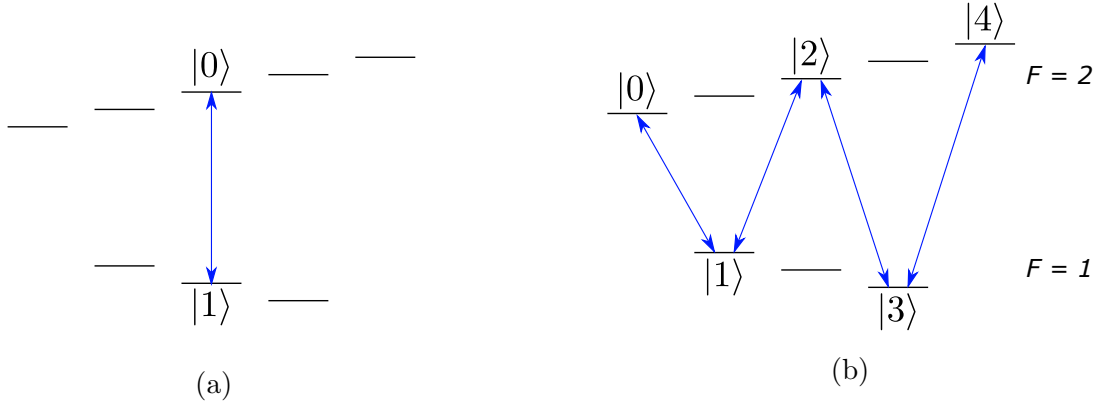


Figure 1.1: Qubit vs qudit encoding: (a) qubit encoding using only two levels and (b) 5-level qudit encoding.

By extending to more levels, we gain several scaling advantages. Lanyon et. al. [9] showed that the number of gates needed to implement a Toffoli gate reduced by more than half by using qutrits rather than qubits. Recently it was shown that qutrits can dramatically improve the circuit depth scaling compared to both qubits and qubits with an additional ancilla [10]. Furthermore, there are indications that the error threshold necessary for fault-tolerant quantum computation is higher for qudits than for qubits [11–13]; i.e. the requirement is more friendly and we can correct all errors more easily.

For exploring qudits, our lab plans to use trapped barium ions. We chose this ion for its long-lived metastable $5D_{5/2}$ state (useful for the shelving scheme presented in chapter 3), and because most of the lasers we need are in the visible range (see Figure 2.3), simplifying some of the optics involved.

This thesis is structured as follows. In chapter 2, I discuss my work on characterizing our ion of choice - $^{137}\text{Ba}^+$ - in preparation for using it to explore qudits. The properties I explore include energy structure, transitions strengths, saturation intensity, and isotope selectivity. In chapter 3, I introduce and explore a shelving technique we propose to use for state readout of qudits. Estimated error rates for this proposed scheme are presented. In the final chapter, I discuss some of the various infrastructural optics projects I completed in order to bring up our lab’s first ion trap, a four-rod Paul trap. The optics for each beam path is laid out, a method for frequency locking the lasers is presented, and a cost-saving rf sources solution for providing rf to various optics components is outlined.

In this chapter, I describe how to calculate the complicated energy structure of $^{137}\text{Ba}^+$, and how to add a magnetic field perturbation. I then discuss calculations of the branching ratios between these energy levels. The energy structure and branching ratios are important for later chapters, especially chapter 3. Next, I present the derivation for saturation intensity of dipole transitions. Finally, I introduce our method for loading specific isotopes of Ba^+ , and how we can proactively choose which one we would like to trap.

2.1 Energy Structure

As our ability to measure atomic spectra has improved and the theory of these spectra has become more refined, we have discovered more interactions which shift the spectra from what was previously expected. One of the first instances of this was Bohr's important discovery that the energy levels of hydrogen are given by

$$E_n = -\frac{E_0}{n^2}, \quad (2.1)$$

where n is the principal quantum number, and $E_0 = 13.6\text{ eV}$ is the energy of the lowest level. Bohr's model predicted the energy levels of hydrogen better than any previous theories. However, this model was only telling a fraction of the story. Solving Schrödinger's equation agrees with Bohr's model in energy, but it tells us that there are actually multiple degenerate states l within these levels, each with different angular momenta.

The theory was modified when the Stern-Gerlach experiment revealed a discrepancy in energy level splittings under an applied magnetic field. A new quantum number, spin, was

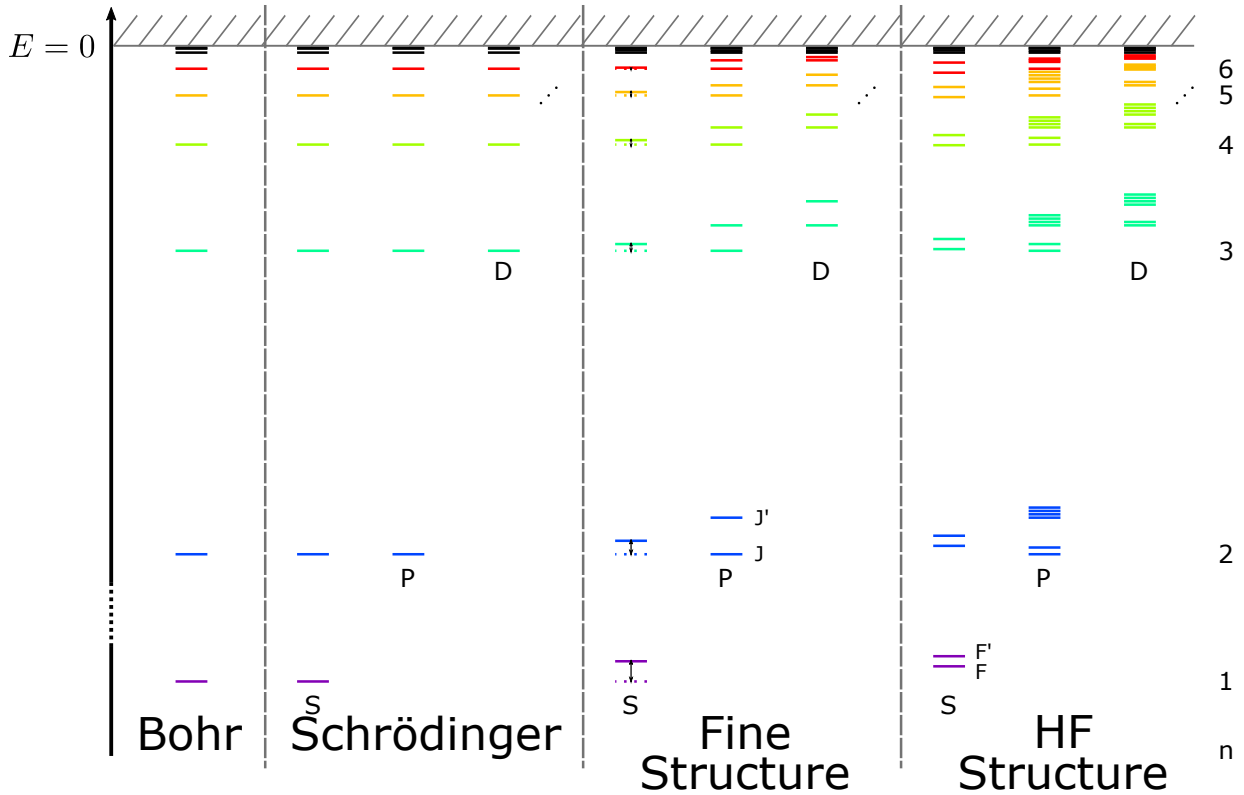


Figure 2.1: Hydrogen energy structure: smaller interactions are considered as we move to the right. Bohr’s model predicted only the different principal energy levels n . Solving Schrödinger’s equation results in many degenerate angular momentum levels within each principal level. When the interaction between the electron spin and the angular momentum is considered, we see fine structure, where each $l \neq 0$ level splits into two levels; we also see a Lamb Shift indicated by the arrows. Finally, we include the interaction of the nuclear spin to get hyperfine structure splitting.

introduced, which gave rise to the fine structure of atoms. This fine structure comes from the electron spin $s = 1/2$ interacting with the electron’s angular momentum l . For $l \neq 0$, each level is split into two fine levels J and J' . Eventually, Schrödinger’s equation was fixed to include this spin and interaction, along with relativity, in the Dirac equation. Fine structure is on the order of $10^{-4} - 10^{-1}eV$.

It was soon discovered that nuclei too have an intrinsic angular momentum, called nuclear spin. The interaction of nuclear spin with the composite angular momentum J leads to an additional hyperfine splitting of each J level into F levels. For hyperfine structure, this splitting can have a higher multiplicity, since the nuclear spin can be any integer or half-integer. Hyperfine structure is on the order of $10^{-7} - 10^{-4}eV$. Figure 2.1 illustrates this progression of insight in the hydrogen atom, from Bohr’s energy levels to hyperfine structure.

The inclusion of electromagnetic fields brings even more richness to the energy structure of atoms. An external magnetic field splits each F level into multitudes of magnetic sub-levels. Applying external electric fields leads to the a shifting of energy levels called the Stark effect. Internal fields complicate the situation immensely, with electron screening and isotope shifts shifting the energy levels by large amounts in some cases. For example, the $4S$ energy level has a lower energy than the $3D$ level in multi-electron atoms, completely contradicting the Bohr model.

Needless to say, theoretically calculating the energy levels of electron orbitals is a tricky business. For anything higher than the helium atom, we have to resort to using various approximations and simplifications. One of the most common methods of simplification is to use perturbation theory; this method allows one to calculate the energies without additional interactions, then introduce further effects afterwards as a perturbation. Using perturbation theory, we are able to look at fine structure and hyperfine structure as small perturbations on the Schrödinger's equation solution and thus calculate their approximate effects.

For fine structure, we must reconsider the motion of the electrons. Relativity says that their kinetic energy is given by

$$KE = (p^2 c^2 + m_0^2 c^4)^{1/2} = m_0 c^2 + \frac{p^2}{2m_0} - \frac{p^4}{8m_0^3 c^2} + \dots, \quad (2.2)$$

where p is momentum, c is the speed of light, and m_0 is the electron rest mass. The first two terms of the series are the mass energy and non-relativistic kinetic energies, which are included in the Schrödinger formulation; the other terms are relativistic terms, which we can treat as perturbations. Using perturbation theory on the first relativistic term, we end up with an energy shift of

$$\Delta E_r = -\frac{\alpha^2 Z^2}{n^2} E_n \left(\frac{3}{4} - \frac{n}{l + 1/2} \right), \quad (2.3)$$

where $\alpha = \frac{c}{4\pi\epsilon_0\hbar}$ is the fine structure constant, ϵ_0 is the permeability of free space, \hbar is Planck's constant, Z is the proton number, and E_n is given by the Bohr energy (Equation 2.1).

The next fine structure effect to consider is the motion of the negatively charged electron around a positively charged nucleus. The electron effectively sees a moving positive charge which imposes an effective magnetic field \vec{B}_{eff} in the same direction as the angular momentum \vec{L} (see Figure 2.2). This effect is called Thomas precession, and the net result is an energy change of

$$\Delta E_s = -\frac{\alpha^2 Z^2}{2n^2} E_n \left(\frac{n(J(J+1) - l(l+1) - s(s+1))}{l(l+1/2)(l+1)} \right) \quad (l \neq 0), \quad (2.4)$$

where J , l , s are the projections of $\vec{J} = \vec{L} + \vec{S}$, \vec{L} , and \vec{S} onto the z axis (\vec{S} is the electron spin vector). Note that this term only applies for $l \neq 0$, since the electron needs an angular momentum to couple to the effective magnetic field created by the nucleus.

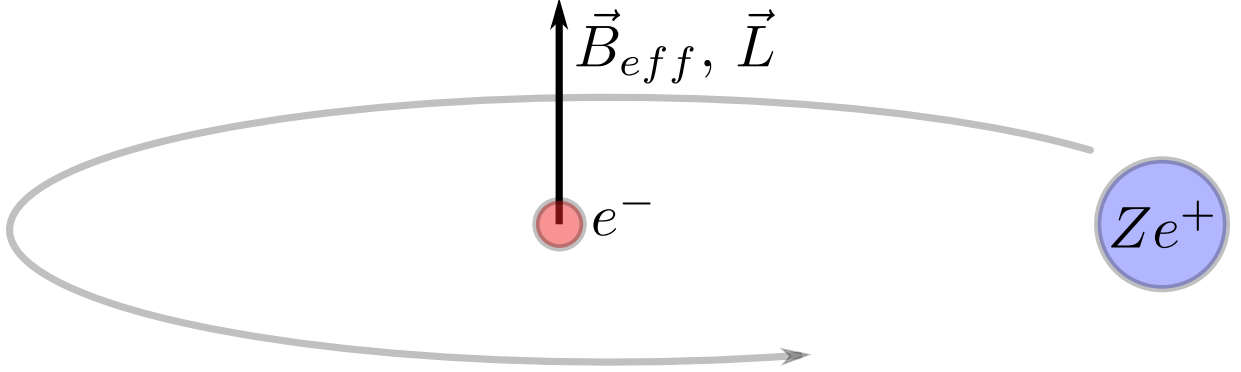


Figure 2.2: Thomas precession: the electron sees a positive charge spinning around it, which induces a magnetic field in the same direction as the electron angular momentum.

In the Dirac equation, there is an extra term which we haven't yet considered called the Darwin Term. This term is nonzero only for electrons with a nonzero wavefunction at the origin: $l = 0$. This term gives an energy shift of

$$\Delta E_D = \frac{2nE_n^2}{m_0^2} \quad (l = 0). \quad (2.5)$$

If we add all of these shifts together, we end up with a surprisingly simple energy shift of

$$\Delta E = -\frac{\alpha^2 Z^2}{n^2} E_n \left(\frac{3}{4} - \frac{n}{J + 1/2} \right). \quad (2.6)$$

Note that this equation works for any angular momentum l .

A final effect typically classified as fine structure is the Lamb Shift. The Lamb Shift comes from quantum electrodynamics; it essentially results from the electron interacting with the vacuum of free space. Electron wavefunctions at the origin are effectively smeared out, shifting the energies up. This has the following effect on energy [14]:

$$\Delta E_{LS} = \frac{8}{6\pi} \frac{Z^4 \alpha^5 m}{n^3} \left(\ln \frac{1}{Z\alpha} \right) \quad (l = 0). \quad (2.7)$$

Again, since the Lamb Shift needs a nonzero wavefunction at the origin, this effect is only relevant for $l = 0$ orbitals.

Next, we discuss hyperfine structure [15]. There is only one effect considered for hyperfine structure: the electromagnetic interaction between a nonzero nuclear spin \vec{I} and the electron angular momentum \vec{J} . We use multipole expansion to get many different interaction terms. By symmetry, we only have magnetic dipole, electric quadrupole, magnetic octupole... For $l = 0$ electrons, the quadrupole contribution is negligible compared to the dipole contribution. However, for $l \neq 0$ electrons, these are comparable. The octupole and

higher order terms are very small for all electrons, and are rarely considered. The magnetic dipole term results in an energy splitting of

$$\Delta E_{md1} = A(F(F+1) - I(I+1) - J(J+1)) = AK \quad (l \neq 0) \quad (2.8)$$

$$\Delta E_{md2} = \frac{A}{2}(F(F+1) - I(I+1) - J(J+1)) = \frac{AK}{2} \quad (l = 0), \quad (2.9)$$

where $A = \frac{2\mu_I\mu_0\mu_B g_s}{3I} \langle \frac{1}{r^3} \rangle$ is the dipole hyperfine constant, μ_I is the nuclear spin magnetic moment, μ_0 is the permeability of free space, μ_B is the Bohr magneton, g_s is the electron spin g-factor, F is the projection of $\vec{F} = \vec{I} + \vec{J}$ onto the z axis, r is the position of the electron, and $K = (F(F+1) - I(I+1) - J(J+1))$.

For the electric quadrupole interaction, we get an energy splitting of

$$\Delta E_{eq} = eQ \left\langle \frac{\delta^2 V_e}{\delta r^2} \right\rangle \frac{\frac{3}{4}K(K+1) - I(I+1)j(j-1)}{2I(2I-1)J(2J-1)} = \frac{B}{4} \frac{\frac{3}{2}K(K+1) - 2I(I+1)J(J+1)}{2I(2I-1)J(2J-1)}, \quad (2.10)$$

where Q is the nuclear electric quadrupole and V_e is the electric potential experienced by the electron from the nucleus.

Finally, we must consider what happens when we apply an external magnetic field \vec{B}_e to our atom, inducing something called Zeeman splitting. This applied field splits our hyperfine levels into magnetic sub-levels of shifted energies given by

$$\Delta E_z = g_J \frac{(F(F+1) + J(J+1) - I(I+1))}{2F(F+1)} \mu_B m_F B_e = g_F \mu_B m_F B_e, \quad (2.11)$$

where $g_J = g_l + \frac{J(J+1) + s(s+1) - l(l+1)}{2J(J+1)}$ is the fine g-factor ($g_l = 1$ is the angular momentum g-factor), m_F is the magnetic hyperfine quantum number, B_e is the magnitude of the magnetic field, and $g_F = g_J \frac{(F(F+1) + J(J+1) - I(I+1))}{2F(F+1)}$ is the hyperfine g-factor. Overall, our hyperfine energy splitting is given by

$$\Delta E_{HF} = \frac{AK}{2} + \frac{B}{4} \frac{\frac{3}{2}K(K+1) - 2I(I+1)J(J+1)}{2I(2I-1)J(2J-1)} + g_F \mu_B m_F B_e. \quad (2.12)$$

In practice, rather than going through this lengthy calculation, it's much easier and more accurate to simply measure the energies using spectroscopy techniques. Spectroscopy was precise enough to measure hyperfine structure as early as the 1920's, and there is an abundance of data on the energy levels of atoms and molecules. Experimentalists use spectroscopy measurements as a starting point, then use perturbation theory to find the effects of applied electromagnetic fields. The motivation for discussing how to calculate the exact solutions was to understand where these overall splittings and shifts come from.

In the literature, fine levels nl_J are cited as wavenumbers in the literature, while hyperfine structure is described by measured hyperfine constants A and B for each fine level

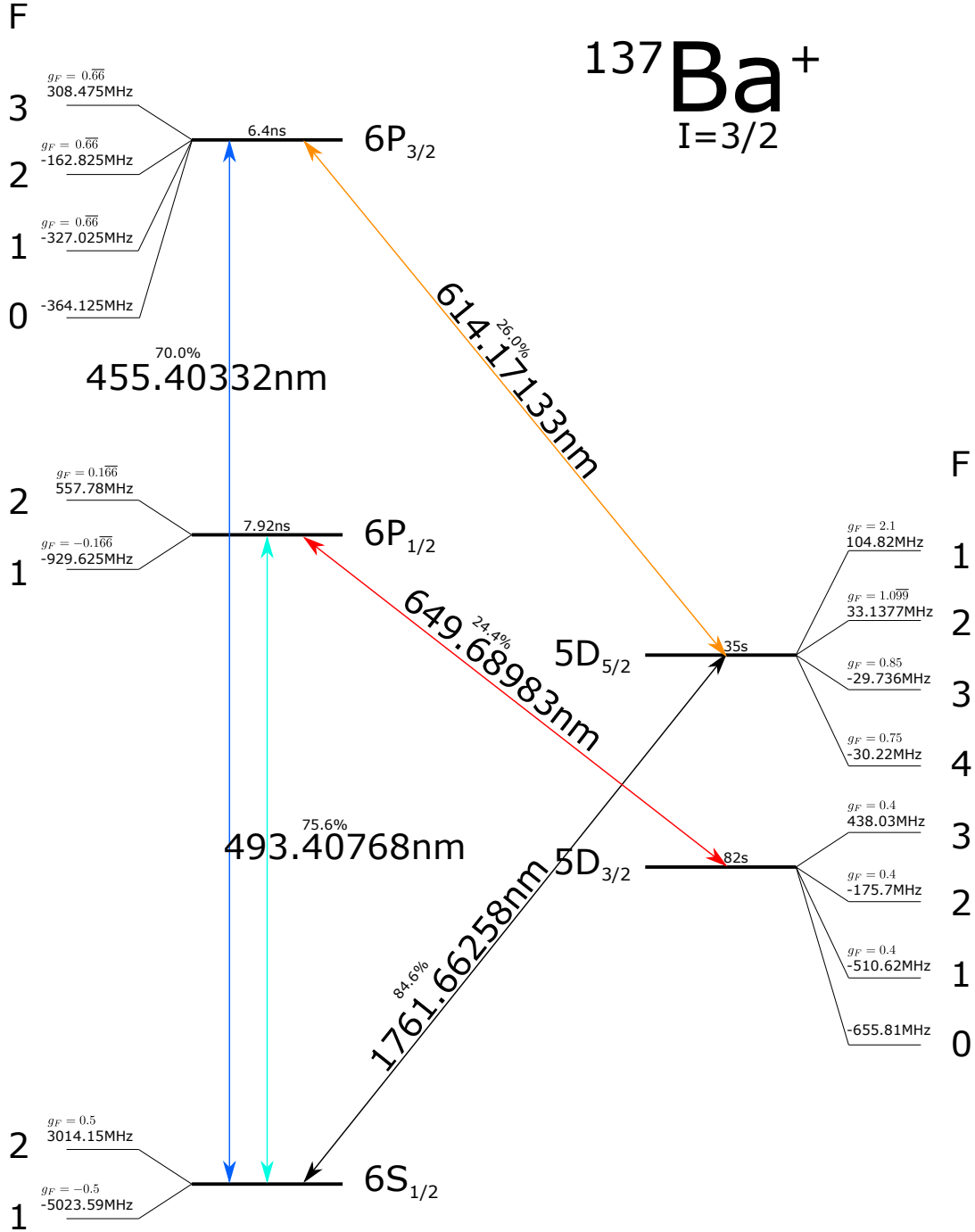


Figure 2.3: $^{137}\text{Ba}^+$ energy structure: [16] the $6S_{1/2} \leftrightarrow 6P_{1/2}$ optical transition is used for optical pumping, Doppler cooling, and fluorescence measurement. The $6S_{1/2} \leftrightarrow 5D_{5/2}$ transition is used to shelve qudit states. The $5D_{3/2} \leftrightarrow 6P_{1/2}$ transition is used to re-pump dark states back into the cooling/fluorescence cycle. The $5D_{5/2} \leftrightarrow 6P_{3/2}$ transition is used to empty the $5D_{5/2}$ state. Because of its nuclear spin $3/2$, each level is split into hyperfine levels: the frequencies of these levels are shown [17–19].

Level	F	g_F	A [18–20]	B [18, 19]	Lifetime [21–23]	Branching Ratios [24–26]	
$6S_{1/2}$	1	-0.5	4018.871	0			
	2	0.5					
$6P_{1/2}$	1	$-0.1\overline{66}$	743.7	0	792ns	$6S_{1/2}$	0.756
	2	$0.1\overline{66}$				$5D_{3/2}$	0.244
$6P_{3/2}$	0	0	127.2	59	64ns	$6S_{1/2}$	0.756
	1	$0.6\overline{6}$				$5D_{3/2}$	0.029
	2	$0.6\overline{6}$				$5D_{5/2}$	0.215
	3	$0.6\overline{6}$					
$5D_{3/2}$	0	0	189.7296	44.5408	82s	$6S_{1/2}$	1
	1	0.4					
	2	0.4					
	3	0.4					
$5D_{5/2}$	1	2.1	-12.028	59.533	35s	$6S_{1/2}$	0.846
	2	1.099				$5D_{3/2}$	0.154
	3	0.85					
	4	0.75					

Table 2.1: Characteristics of $^{137}\text{Ba}^+$: g_F is the hyperfine g-factor, A is the hyperfine constant, B is the quadrupole hyperfine constant.

nl_J . Figure 2.3 shows the energy structure of one of the ions our lab is most interested in: $^{137}\text{Ba}^+$. Other various characteristics of $^{137}\text{Ba}^+$ are given in Table 2.1.

To trap ions and utilize the magnetic sublevels, we apply an external magnetic field \vec{B}_e . Equation 2.12 is exact when there are no external fields, however when we apply a magnetic field, it couples to both the angular momentum and the nuclear spin - \vec{F} ceases to be a good quantum number for the system. For an exact solution, we must go back to using just \vec{I} and \vec{J} . The overall hyperfine Hamiltonian with an applied magnetic field is

$$\vec{H} = A\vec{I} \cdot \vec{J} + B \frac{3(\vec{I} \cdot \vec{J})^2 + \frac{3}{2}\vec{I} \cdot \vec{J} - I(I+1)J(J+1)}{2I(2I-1)J(2J-1)} + \frac{\mu_B}{\hbar}(g_J m_J B_e + g_I m_I B_e). \quad (2.13)$$

Expanding the dot products in terms of ladder operators \vec{K}_{\pm} gives us the following matrix elements of the Hamiltonian

$$\begin{aligned} \langle \vec{H} \rangle &= A m_I m_J + \frac{\mu_B}{\hbar}(g_J m_J B_e + g_I m_I B_e) + \frac{B}{2I(2I-1)J(2J-1)} \\ &\times \left[\frac{3}{2} m_I m_J + 3 m_I^2 m_J^2 + \left\langle \frac{I_- I_+ J_+ J_-}{4} \right\rangle + \left\langle \frac{I_+ I_- J_- J_+}{4} \right\rangle - I(I+1)J(J+1) \right] \end{aligned} \quad (2.14)$$

		$-\frac{3}{2}$	$-\frac{1}{2}$	$\frac{1}{2}$	$\frac{3}{2}$	$-\frac{1}{2}$	$\frac{1}{2}$	$\frac{3}{2}$	$\frac{1}{2}$	$\frac{3}{2}$	$\frac{3}{2}$	$-\frac{3}{2}$	$-\frac{1}{2}$	$\frac{1}{2}$	$-\frac{3}{2}$	$-\frac{1}{2}$	$-\frac{3}{2}$
m_J	m_I	$\frac{3}{2}$	$\frac{1}{2}$	$-\frac{1}{2}$	$-\frac{3}{2}$	$\frac{3}{2}$	$\frac{1}{2}$	$-\frac{1}{2}$	$\frac{3}{2}$	$\frac{1}{2}$	$\frac{3}{2}$	$-\frac{1}{2}$	$-\frac{1}{2}$	$-\frac{3}{2}$	$-\frac{1}{2}$	$-\frac{3}{2}$	$-\frac{3}{2}$
$-\frac{3}{2}$	$\frac{3}{2}$	D	\bar{A}	B	0	0	0	0	0	0	0	0	0	0	0	0	0
$-\frac{1}{2}$	$\frac{1}{2}$	A	D	\bar{A}	B	0	0	0	0	0	0	0	0	0	0	0	0
$\frac{1}{2}$	$-\frac{1}{2}$	\bar{B}	A	D	\bar{A}	0	0	0	0	0	0	0	0	0	0	0	0
$\frac{3}{2}$	$-\frac{3}{2}$	0	\bar{B}	A	D	0	0	0	0	0	0	0	0	0	0	0	0
$-\frac{1}{2}$	$\frac{3}{2}$	0	0	0	0	D	\bar{A}	B	0	0	0	0	0	0	0	0	0
$\frac{1}{2}$	$\frac{1}{2}$	0	0	0	0	A	D	\bar{A}	0	0	0	0	0	0	0	0	0
$\frac{3}{2}$	$-\frac{1}{2}$	0	0	0	0	\bar{B}	A	D	0	0	0	0	0	0	0	0	0
$\frac{1}{2}$	$\frac{3}{2}$	0	0	0	0	0	0	0	D	\bar{A}	0	0	0	0	0	0	0
$\frac{3}{2}$	$\frac{1}{2}$	0	0	0	0	0	0	0	A	D	0	0	0	0	0	0	0
$\frac{3}{2}$	$\frac{3}{2}$	0	0	0	0	0	0	0	0	0	D	0	0	0	0	0	0
$-\frac{3}{2}$	$-\frac{1}{2}$	0	0	0	0	0	0	0	0	0	0	D	\bar{A}	B	0	0	0
$-\frac{1}{2}$	$-\frac{1}{2}$	0	0	0	0	0	0	0	0	0	0	A	D	\bar{A}	0	0	0
$\frac{1}{2}$	$-\frac{3}{2}$	0	0	0	0	0	0	0	0	0	0	\bar{B}	A	D	0	0	0
$-\frac{3}{2}$	$-\frac{1}{2}$	0	0	0	0	0	0	0	0	0	0	0	0	0	D	\bar{A}	0
$-\frac{1}{2}$	$-\frac{3}{2}$	0	0	0	0	0	0	0	0	0	0	0	0	0	A	D	0
$-\frac{3}{2}$	$-\frac{3}{2}$	0	0	0	0	0	0	0	0	0	0	0	0	0	0	0	D

Table 2.2: Block form atomic hamiltonian: an example of a Hamiltonian put into block diagonal form by rearranging the states $|m_I, m_J\rangle$. Elements $A(\bar{A})$ and $B(\bar{B})$ are given by Equations 2.15 and 2.16 in the text, respectively; D is given by Equation 2.14 in the text.

$$2\langle m_J \pm 1, m_I \mp 1 | \vec{H} \rangle = \left[A + \frac{B}{2I(2I-1)(J(2J-1))} \left(\frac{3}{2} + 3(m_I \mp 1)(m_J \pm 1) + m_I m_J \right) \right] \langle m_J \pm 1, m_I \mp 1 | I_{\mp} J_{\pm} \rangle \quad (2.15)$$

$$\langle m_J \pm 2, m_I \mp 2 | \vec{H} \rangle = \frac{3B}{8I(2I-1)(J(2J-1))} \langle m_J \pm 2, m_I \mp 2 | I_{\mp} I_{\mp} J_{\pm} J_{\pm} \rangle, \quad (2.16)$$

where

$$\begin{aligned} \langle I_{\mp} I_{\pm} J_{\pm} J_{\mp} \rangle &= [I(I+1) - m_I(m_I \pm 1)] [J(J+1) - m_J(m_J \mp 1)] \\ \langle m_J \pm 1, m_I \mp 1 | I_{\mp} J_{\pm} \rangle &= \sqrt{[J(J+1) - m_J(m_J \pm 1)] [I(I+1) - m_I(m_I \mp 1)]} \\ \langle m_J \pm 2, m_I \mp 2 | I_{\mp} I_{\mp} J_{\pm} J_{\pm} \rangle &= \sqrt{[I(I+1) - m_I(m_I \mp 1)] [I(I+1) - (m_I \mp 1)(m_I \mp 2)]} \\ &\quad \times \sqrt{[J(J+1) - m_J(m_J \pm 1)] [J(J+1) - (m_J \pm 1)(m_J \pm 2)]}. \end{aligned} \quad (2.17)$$

To calculate the energy levels, we just have to build this Hamiltonian for our energy level $n l_J$ and magnetic field B_e , then diagonalize it. Diagonalization of this matrix can be

computationally difficult unless we arrange the energy levels cleverly. If we arrange the energy levels $|m_J, m_I\rangle$ so that $m_F = m_I + m_J$ levels are grouped, as follows:

$$\begin{aligned}
& |m_{J,min}, m_{I,max}\rangle, |m_{J,min} + 1, m_{I,max} - 1\rangle, \dots |m_{J,max}, m_{I,min}\rangle, \\
& |m_{J,min} + 1, m_{I,max}\rangle, |m_{J,min} + 2, m_{I,max} - 1\rangle \dots |m_{J,max}, m_{I,min} + 1\rangle, \\
& \vdots \\
& |m_{J,max}, m_{I,max}\rangle, \\
& |m_{J,min}, m_{I,max} - 1\rangle, |m_{J,min} + 1, m_{I,max} - 2\rangle \dots |m_{J,max} - 1, m_{I,min}\rangle, \\
& |m_{J,min}, m_{I,max} - 2\rangle, |m_{J,min} + 1, m_{I,max} - 3\rangle \dots |m_{J,max} - 2, m_{I,min}\rangle, \\
& \vdots \\
& |m_{J,min}, m_{I,min}\rangle,
\end{aligned} \tag{2.18}$$

then the result is a block diagonal matrix as shown in Table 2.2. With this matrix, we can diagonalize each block individually to get all of the energy levels.

$^{137}\text{Ba}^+ - 6S_{1/2}$ Energy Levels

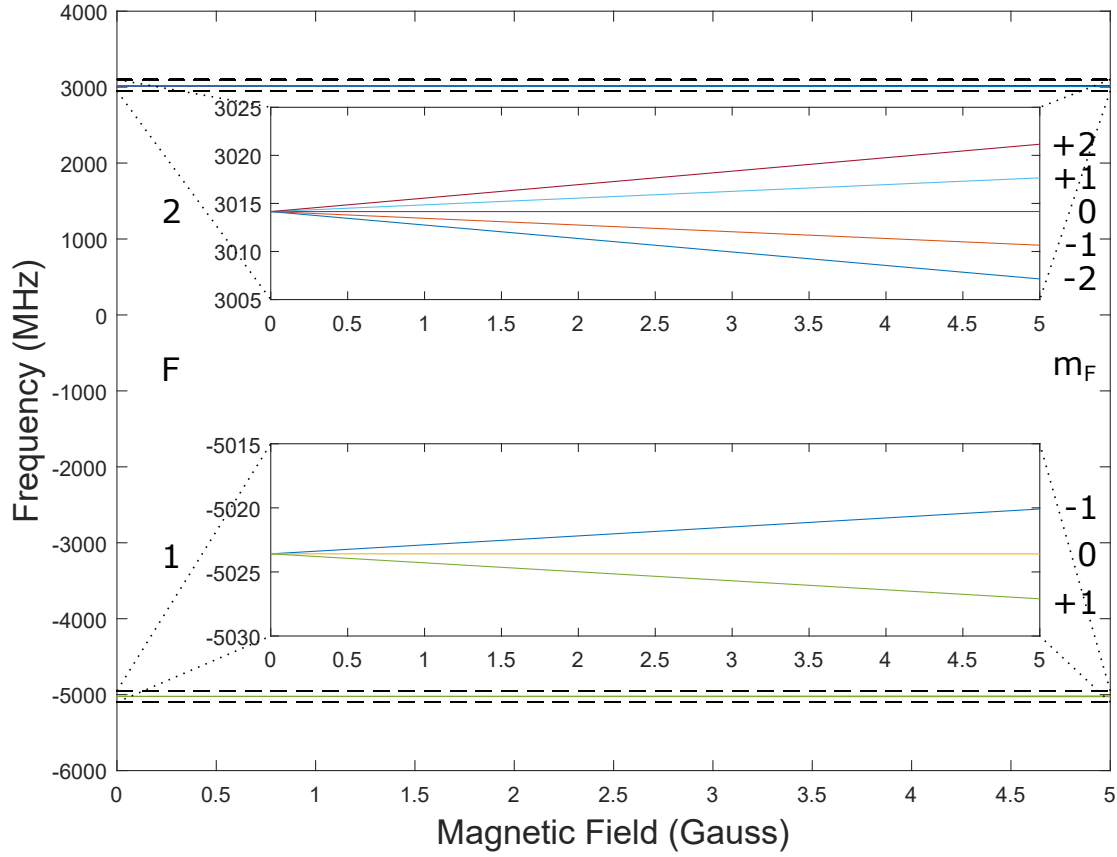


Figure 2.4: $^{137}\text{Ba}^+ - 6S_{1/2}$ state hyperfine splitting with magnetic field: applying a magnetic field lifts the degeneracy, allowing m_F levels to be resolved. Obtained by solving Equation 2.13 for each magnetic field B_e .

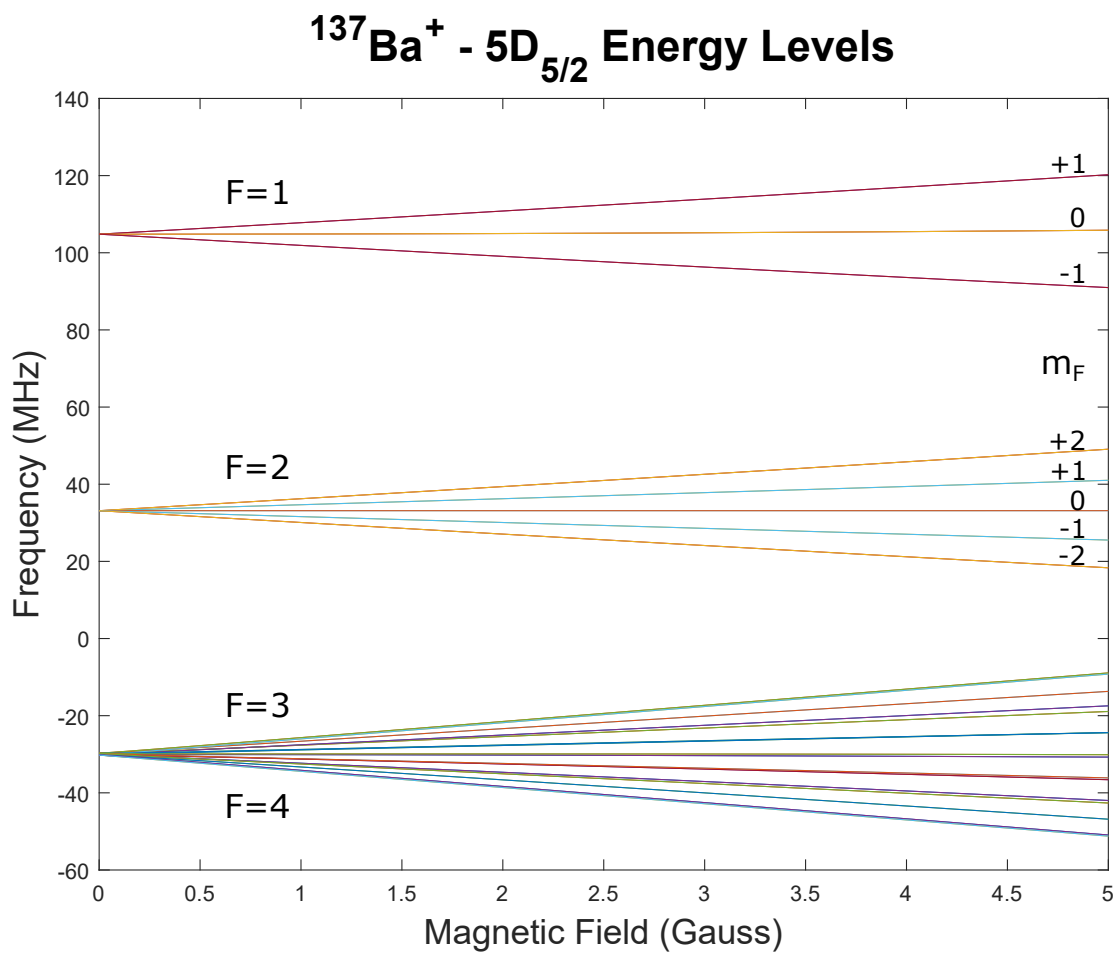


Figure 2.5: $^{137}\text{Ba}^+ 5D_{5/2}$ state hyperfine splitting with magnetic field: the $F = 3, 4$ levels are very close to one another, so we choose to use only $F = 1, 2$.

2.2 Transition Branching Ratios/Strengths

The next useful data we need are the branching ratios/transition strengths of the various dipole and quadrupole transitions we plan to use in $^{137}\text{Ba}^+$. To build up to this, we must first discuss Clebsch Gordan coefficients.

Say we have two angular momenta \vec{J}_1 and \vec{J}_2 . We add them to get the new basis $\vec{J} = \vec{J}_1 + \vec{J}_2$. Our new basis is $|J_1, J_2; J, m\rangle$, which we can simplify to $|J_1, J_2; J, m\rangle = |J, m\rangle$ if we specify J_1 and J_2 . The eigenvalues in our new basis can easily be shown to be

$$\begin{aligned}\vec{J}_1^2 |J, m\rangle &= J_1(J_1 + 1)\hbar^2 |J, m\rangle \\ \vec{J}_2^2 |J, m\rangle &= J_2(J_2 + 1)\hbar^2 |J, m\rangle \\ \vec{J}^2 |J, m\rangle &= J(J + 1)\hbar^2 |J, m\rangle \\ \vec{J}_z |J, m\rangle &= m\hbar |J, m\rangle.\end{aligned}\tag{2.19}$$

We can multiply this state by the identity to get a transformation between the two bases:

$$\begin{aligned}|J, m\rangle &= \sum_{J'_1, J'_2, m_1, m_2} |J'_1, m_1; J'_2, m_2\rangle \underline{\langle J'_1, m_1; J'_2, m_2 | J, m\rangle} \\ |J_1, m_1; J_2, m_2\rangle &= \sum_{J', J', m} |J', J'; J, m\rangle \underline{\langle J', J'; J, m | J_1, m_1; J_2, m_2\rangle},\end{aligned}\tag{2.20}$$

where the underlined brackets are called Clebsch Gordan Coefficients. These coefficients essentially tell us how much each sub-state makes up the overall composite state.

If we apply the operators \vec{J}_1^2 , \vec{J}_2^2 and \vec{J}_z , it can be easily shown that $J'_i = J_i$ and $m = m_1 + m_2$, leaving us with

$$\begin{aligned}|J, m\rangle &= \sum_{J_1, J_2, m_1, m_2} |J_1, m_1; J_2, m_2\rangle \underline{\langle J_1, m_1; J_2, m_2 | J, m\rangle} \\ |J_1, m_1; J_2, m_2\rangle &= \sum_{J, m} |J, m\rangle \underline{\langle J, m | J_1, m_1; J_2, m_2\rangle}.\end{aligned}\tag{2.21}$$

Using the constraint $m = m_1 + m_2$, and setting the total number of states we have in each basis equal, we find the following limit for composite states J :

$$|J_1 - J_2| \leq J \leq J_1 + J_2.\tag{2.22}$$

Multiplying the kets in Equation 2.21 by the bra $\langle J', m' |$, we get the orthogonality relations

$$\begin{aligned}\sum_{J, m} \langle J_1, m'_1; J_2, m'_2 | J, m\rangle \langle J, m | J_1, m_1; J_2, m_2\rangle &= \delta_{m_1, m'_1} \delta_{m, m'} \\ \sum_{m_1, m_2} \langle J, m | J_1, m_1; J_2, m_2\rangle \langle J_1, m_1; J_2, m_2 | J', m'\rangle &= \delta_{J, J'} \delta_{m, m'}.\end{aligned}\tag{2.23}$$

There is only one state for which J is the highest possible value $J_1 + J_2$, so the Clebsch Gordan coefficient is unity. From there, we use the ladder operator $\vec{J}_\pm = \vec{J}_{1\pm} + \vec{J}_{2\pm}$ to find the others, making use of the relation

$$J_\pm |J, m\rangle = \hbar \sqrt{J(J+1) - m(m \pm 1)} |J, m \pm 1\rangle. \quad (2.24)$$

Example: $l = 2, s = 1$

The maximal angular momentum state is $J = l + s = 2 + 1 = 3$ with $m = m_l + m_s = 2 + 1 = 3$. Next, we apply the \vec{J}_- operator to the $|J, m\rangle$ state, the $\vec{L}_- + \vec{S}_-$ operator to the $|l, m_l; s, m_s\rangle$ state, and set these expressions equal to each other.

$$\vec{J}_- |3, 3\rangle = \hbar \sqrt{3(3+1) - 3(3-1)} |3, 2\rangle = \sqrt{6} |3, 2\rangle$$

$$\begin{aligned} \vec{L}_- + \vec{S}_- |2, 2; 1, 1\rangle &= \sqrt{2(2+1) - 2(2-1)} |2, 1; 1, 1\rangle + \sqrt{1(1+1) - 1(1-1)} |2, 2; 1, 0\rangle \\ &= 2 |2, 1; 1, 1\rangle + \sqrt{2} |2, 2; 1, 0\rangle. \end{aligned}$$

Equating these, we can solve for the Clebsch Gordan coefficients (underlined)

$$|3, 2\rangle = \frac{2}{\sqrt{6}} |2, 1; 1, 1\rangle + \sqrt{\frac{2}{6}} |2, 2; 1, 0\rangle.$$

To get the coefficients for different J values, we use orthogonality (Equation 2.23):

$$\langle 3, 2 | 2, 2 \rangle = 0$$

$$\begin{aligned} \langle 3, 2 | 2, 2 \rangle &= \left(\frac{2}{\sqrt{6}} \langle 2, 1; 1, 1 | + \sqrt{\frac{2}{6}} \langle 2, 2; 1, 0 | \right) (a |2, 1; 1, 1\rangle + b |2, 2; 1, 0\rangle) \\ &= \frac{2}{\sqrt{6}} a + \frac{1}{\sqrt{3}} b = 0, \end{aligned}$$

along with the completeness relation $a^2 + b^2 = 1$, where a and b are the Clebsch Gordan coefficients. We find that $a = \frac{1}{\sqrt{3}}$ and $b = \frac{2}{\sqrt{6}}$, so that

$$|2, 2\rangle = \frac{1}{\sqrt{3}} |2, 1; 1, 1\rangle + \frac{2}{\sqrt{6}} |2, 2; 1, 0\rangle.$$

From here we continue to apply ladder operators and orthogonality with the completeness relation to find the remaining Clebsch Gordan coefficients.

Here are several useful symmetry relations for the Clebsch Gordan coefficients:

$$\langle J_1, m_1; J_2, m_2 | J_3, m_3 \rangle = (-1)^{J_1+J_2-J_3} \langle J_2, m_2; J_1, m_1 | J_3, m_3 \rangle \quad (2.25)$$

$$\langle J_1, m_1; J_2, m_2 | J_3, m_3 \rangle = (-1)^{J_1-m_1} \sqrt{\frac{2J_3+1}{2J_2+1}} \langle J_3, m_3; J_1, -m_1 | J_2, m_2 \rangle \quad (2.26)$$

$$\langle J_1, m_1; J_2, m_2 | J_3, m_3 \rangle = (-1)^{J_2+m_2} \sqrt{\frac{2J_3+1}{2J_1+1}} \langle J_2, -m_2; J_3, m_3 | J_1, m_1 \rangle \quad (2.27)$$

$$\langle J_1, m_1; J_2, m_2 | J_3, m_3 \rangle = (-1)^{J_1+J_2-J_3} \langle J_1, -m_1; J_2, -m_2 | J_3, -m_3 \rangle. \quad (2.28)$$

Finally, it's useful to define the Wigner 3j symbol:

$$\begin{pmatrix} J_1 & J_2 & J_3 \\ m_1 & m_2 & m_3 \end{pmatrix} = \frac{(-1)^{J_1+J_2-J_3}}{\sqrt{2J_3+1}} \langle J_1, m_1; J_2, m_2 | J_3, -m_3 \rangle \quad (2.29)$$

and the Wigner 6j symbol:

$$\left\{ \begin{matrix} J_1 & J_2 & J_{12} \\ J_3 & -J & J_{23} \end{matrix} \right\} = \frac{(-1)^{J_1+J_2+J_3+J}}{\sqrt{(2J_{12}+1)(2J_{23}+1)}} \langle J_1, J_{23}; J, m | J_{12}, J_3; J, m \rangle. \quad (2.30)$$

Next, we define a spherical tensor operator as a set of $2k+1$ operators which transform among themselves under rotation just like angular momentum states $|J, m\rangle$ do ($J=k$). Rotation on an angular momentum state looks like

$$R(\zeta)|J, m\rangle = \sum_{m'=-J}^J |J, m'\rangle \langle J, m' | R(\zeta) | J, m \rangle = \sum_{m'=-J}^J |J, m'\rangle d_{m',m}^{(j)}(\zeta) \quad (2.31)$$

$$d_{m',m}^{(j)}(\zeta) = \langle J, m' | R(\zeta) | J, m \rangle. \quad (2.32)$$

So for a spherical tensor operator, this rotation looks like

$$R(\zeta)T_q^{(k)}R^\dagger(\zeta) = \sum_{q'=-k}^k T_{q'}^{(k)} d_{q',q}^{(k)}(\zeta). \quad (2.33)$$

Now, we apply a tensor operator to an angular momentum state

$$T_q^{(k)}|\alpha', J', m'\rangle,$$

where α' contains all non-angular momentum quantum numbers (radial). If we rotate by $R(\zeta)$ and multiply by the identity, we see that they rotate separately,

$$R(\zeta)T_q^{(k)}|\alpha', J', m'\rangle = R(\zeta)T_q^{(k)}R^\dagger(\zeta)R(\zeta)|\alpha', J', m'\rangle.$$

The ket rotates as $|J', m'\rangle$ and the operator rotates as $|k, q\rangle$. So overall, it rotates as $|k, q; J', m'\rangle$. Without the tensor operator, this would look like

$$|k, q; J', m'\rangle = \sum_{k', q'} |k', q'\rangle \langle k', q' | J', m'; k, q \rangle.$$

Similarly, with the tensor operator,

$$T_q^{(k)}|\alpha', J', m'\rangle = \sum_{k', q'} |\tilde{\alpha}, k', q'\rangle \langle k', q' | J', m'; k, q \rangle.$$

Finally, multiplying by a bra on the left and only keeping the non-zero terms, we have

$$\begin{aligned}\langle \alpha, J, m | T_q^{(k)} | \alpha', J', m' \rangle &= \sum_{k', q'} \langle \alpha, J, m | \tilde{\alpha}, k', q' \rangle \langle k', q' | J', m'; k, q \rangle \\ &= (-1)^{2k} \langle \alpha, J || T^{(k)} || \alpha', J' \rangle \langle J, m | J', m'; k, q \rangle,\end{aligned}\quad (2.34)$$

where we introduced the Reduced Matrix Element, an m -independent scalar:

$$\langle \alpha, J || T^{(k)} || \alpha', J' \rangle = (-1)^{2k} \langle \alpha, J, m | \tilde{\alpha}, J, m \rangle. \quad (2.35)$$

This statement is called the Wigner-Eckart Theorem. We can also use the orthogonality relation (Equation 2.23) to get the inverse of the Wigner-Eckart Theorem for a different expression for the Reduced Matrix Element:

$$\langle \alpha, J || T^{(k)} || \alpha', J' \rangle = (-1)^{2k} \sum_{m', q} \langle \alpha, J, m | T_q^{(k)} | \alpha', J', m' \rangle \langle J, m | J', m'; k, q \rangle. \quad (2.36)$$

In the case where a tensor operator only acts on a subspace of the angular momentum, say J_1 , we can decompose the Reduced Matrix Element. We start with the Inverse Wigner Eckart Theorem we just derived, multiplying by the identity twice with bases J_1, m_1, J_2, m_2 and J'_1, m'_1, J'_2, m'_2 :

$$\begin{aligned}\langle J || T^{(k)} || J' \rangle &= (-1)^{2k} \sum_{m', q} \langle J, m | T_q^{(k)} | J', m' \rangle \langle J, m | J', m'; k, q \rangle \\ &= (-1)^{2k} \sum_{m', q, m_1, m_2, m'_1, m'_2} \langle J, m | J_1, m_1; J_2, m_2 \rangle \langle J_1, m_1; J_2, m_2 | T_q^{(k)} | J'_1, m'_1; J'_2, m'_2 \rangle \\ &\quad \times \langle J'_1, m'_1; J'_2, m'_2 | J', m' \rangle \langle J, m | J', m'; k, q \rangle.\end{aligned}$$

The operator only acts on the J_1, m_1 subspace, so we can pull the bracket $\langle J_2, m_2 | J'_2, m'_2 \rangle$ out of the operator term. Now the only nonzero terms occur when $J_2 = J'_2$ and $m_2 = m'_2$:

$$\begin{aligned}\langle J || T^{(k)} || J' \rangle &= (-1)^{2k} \sum_{m', q, m_1, m_2, m'_1, m'_2} \langle J, m | J_1, m_1; J_2, m_2 \rangle \langle J'_1, m'_1; J'_2, m'_2 | J', m' \rangle \langle J, m | J', m'; k, q \rangle \\ &\quad \times \langle J_1, m_1 | T_q^{(k)} | J'_1, m'_1 \rangle \delta_{J_2, J'_2} \delta_{m_2, m'_2} \\ &= (-1)^{2k} \sum_{m', q, m_1, m_2, m'_1} \langle J, m | J_1, m_1; J_2, m_2 \rangle \langle J'_1, m'_1; J_2, m_2 | J', m' \rangle \langle J, m | J', m'; k, q \rangle \\ &\quad \times \langle J_1, m_1 | T_q^{(k)} | J'_1, m'_1 \rangle.\end{aligned}\quad (2.37)$$

Next, we use the Wigner-Eckart Theorem:

$$\langle J || T^{(k)} || J' \rangle = (-1)^{2k} \sum_{m', q, m_1, m_2, m'_1} \langle J, m | J_1, m_1; J_2, m_2 \rangle \langle J'_1, m'_1; J_2, m_2 | J', m' \rangle \langle J, m | J', m'; k, q \rangle$$

$$\begin{aligned}
& \times (-1)^{2k} \langle J_1 || T^k || J_1 \rangle \langle J_1, m_1 | J'_1, m'_1; k, q \rangle \\
& = \sum_{m', q, m_1, m_2, m'_1} \langle J_1, m_1; J_2, m_2 | J, m \rangle \langle J'_1, m'_1; J_2, m_2 | J', m' \rangle \langle J, m | J', m'; k, q \rangle \\
& \quad \times \langle J_1, m_1 | J'_1, m'_1; k, q \rangle \langle J_1 || T^k || J_1 \rangle,
\end{aligned}$$

where we conjugated the first Clebsch Gordan coefficient, canceled the $(-1)^{2k}$ s and rearranged the equation. Now, we apply the symmetry relation 2.25 to the two Clebsch Gordan coefficients in line 2, giving us

$$\begin{aligned}
\langle J || T^{(k)} || J' \rangle & = \sum_{m', q, m_1, m_2, m'_1} \langle J_1, m_1; J_2, m_2 | J, m \rangle \langle J'_1, m'_1; J_2, m_2 | J', m' \rangle \\
& \times (-1)^{J'+k-J} (-1)^{J'_1+k-J_1} \langle k, q; J', m' | J, m \rangle \langle k, q; J'_1, m'_1 | J_1, m_1 \rangle \langle J_1 || T^k || J_1 \rangle.
\end{aligned}$$

The explicit form for the Wigner 6j symbol, which we did not explore here, is [27]

$$\begin{aligned}
\left\{ \begin{matrix} J_1 & J_2 & J_{12} \\ J_3 & -J & J_{23} \end{matrix} \right\} & = \frac{(-1)^{J_1+J_2+J_3+J}}{\sqrt{(2J_{12}+1)(2J_{23}+1)}} \sum_{m_1, m_2, m_3, m_{12}, m_{23}} \langle J_{12}, m_{12}; J_3, m_3 | J, m \rangle \\
& \times \langle J_1, m_1; J_2, m_2 | J_{12}, m_{12} \rangle \langle J_1, m_1; J_{23}, m_{23} | J, m \rangle \langle J_2, m_2; J_3, m_3 | J_{23}, m_{23} \rangle. \quad (2.38)
\end{aligned}$$

Our current four Clebsch Gordan coefficients have this form, with $J_1 \rightarrow k$, $J_2 \rightarrow J'_1$, $J_3 \rightarrow J_3$, $J \rightarrow J$, J_{12} . So we can write this as a 6j symbol as follows:

$$\begin{aligned}
& \sum_{m', q, m_1, m_2, m'_1} \langle J_1, m_1; J_2, m_2 | J, m \rangle \langle J'_1, m'_1; J_2, m_2 | J', m' \rangle \langle k, q; J', m' | J, m \rangle \langle k, q; J'_1, m'_1 | J_1, m_1 \rangle \\
& = (-1)^{-k-J'_1-J_2-J} \sqrt{(2J_1+1)(2J'+1)} \left\{ \begin{matrix} k & J'_1 & J_1 \\ J_2 & J & J' \end{matrix} \right\}.
\end{aligned}$$

Now we can finalize our decomposed equation:

$$\begin{aligned}
\langle J || T^{(k)} || J' \rangle & = (-1)^{J'+k-J} (-1)^{J'_1+k-J_1} (-1)^{-k-J'_1-J_2-J} \\
& \quad \times \sqrt{(2J_1+1)(2J'+1)} \left\{ \begin{matrix} k & J'_1 & J_1 \\ J_2 & J & J' \end{matrix} \right\} \langle J_1 || T^k || J_1 \rangle \\
& = (-1)^{J'+k-J_1-J_2-2J} \sqrt{(2J_1+1)(2J'+1)} \left\{ \begin{matrix} k & J'_1 & J_1 \\ J_2 & J & J' \end{matrix} \right\} \langle J_1 || T^k || J_1 \rangle \\
& = (-1)^{J'+k+J_1+J_2} \sqrt{(2J_1+1)(2J'+1)} \left\{ \begin{matrix} k & J'_1 & J_1 \\ J_2 & J & J' \end{matrix} \right\} \langle J_1 || T^k || J_1 \rangle, \quad (2.39)
\end{aligned}$$

where in the last step, we used the fact that $J_1 + J_2 + J$ is an integer, so that $(-1)^{2(J_1+J_2+J)} = 1$. Then we multiplied by the identity to arrive at the form shown in Equation 2.39.

2.2.1 Dipole Transitions

We'll start out by looking at dipole fine structure and hyperfine structure matrix elements. The dipole is a vector operator of rank 1, so $k = 1$. For fine structure ($\vec{J} = \vec{L} + \vec{S}$), we first apply the Wigner-Eckart Theorem to the dipole operator:

$$\langle J, m_J | d_q | J', m'_J \rangle = \langle J || d || J' \rangle \langle J, m_J | J', m'_J; k = 1, q \rangle. \quad (2.40)$$

Next, we use the symmetry relation from Equation 2.27:

$$\langle J_1, m_1; J_2, m_2 | J_3, m_3 \rangle = (-1)^{J_2+m_2} \sqrt{\frac{2J_3+1}{2J_1+1}} \langle J_2, -m_2; J_3, m_3 | J_1, m_1 \rangle,$$

with the correspondences $J_1 \rightarrow k = 1$, $J_2 \rightarrow J$, $J_3 \rightarrow J'$, resulting in

$$\begin{aligned} \langle J, m_J | d_q | J', m'_J \rangle &= \langle J || d || J' \rangle (-1)^{1+q+1+J-J'} \sqrt{\frac{2J+1}{2J'+1}} \langle J', m'_J | J, m_J; k = 1, -q \rangle \\ &= \langle J || d || J' \rangle (-1)^{J-J'+q} \sqrt{\frac{2J+1}{2J'+1}} \langle J', m'_J | J, m_J; k = 1, -q \rangle. \end{aligned}$$

Also, remember that in addition of angular momenta, we have $m = m_1 + m_2$. In this case, $m_J = m'_J + q$:

$$\begin{aligned} \langle J, m_J | d_q | J', m'_J \rangle &= \langle J || d || J' \rangle \langle J, m_J | J', m'_J; k = 1, q \rangle \\ &= \langle J || d || J' \rangle (-1)^{J-J'+m_J-m'_J} \sqrt{\frac{2J+1}{2J'+1}} \langle J', m'_J | J, m_J; k = 1, -q \rangle. \end{aligned} \quad (2.41)$$

Now, let's express the dipole matrix element in terms of the Wigner 3j symbol. In terms of Equation 2.29, we have the following correspondences with Equation 2.40: $J_1 \rightarrow J'$, $J_2 \rightarrow k = 1$, $J_3 \rightarrow J$. So we can rewrite this as

$$\begin{aligned} \langle J, m_J | d_q | J', m'_J \rangle &= \langle J || d || J' \rangle \langle J, m_J | J', m'_J; k = 1, q \rangle \\ &= \langle J || d || J' \rangle (-1)^{1-m_J-J'} \sqrt{2J+1} \begin{pmatrix} J' & 1 & J \\ m'_J & q & -m_J \end{pmatrix}. \end{aligned} \quad (2.42)$$

Since the dipole operator doesn't effect spin, we can decompose this Reduced Matrix via Equation 2.39:

$$\langle J || d || J' \rangle = (-1)^{J'+l+s+1} \sqrt{(2J'+1)(2l+1)} \left\{ \begin{matrix} l & l' & 1 \\ J' & J & s \end{matrix} \right\} \langle l || d || l' \rangle, \quad (2.43)$$

where we swapped the columns of the 6-j symbol from the symmetry relations for 6-j symbols [27].

Similarly, for hyperfine structure we have

$$\langle F, m_F | d_q | F', m'_F \rangle = \langle F || d || F' \rangle (-1)^{1-m_F-F'} \sqrt{2F+1} \begin{pmatrix} F' & 1 & F \\ m'_F & q & -m_F \end{pmatrix} \quad (2.44)$$

$$\langle F||d||F' \rangle = (-1)^{F'+J+I+1} \sqrt{(2F'+1)(2J+1)} \begin{Bmatrix} J & J' & 1 \\ F' & F & I \end{Bmatrix} \langle J||d||J' \rangle. \quad (2.45)$$

We're interested in looking at a single $J \rightarrow J'$ transition at a time, so that $\langle J||d||J' \rangle$ is the same for all of them. So overall we need to look at the coefficient

$$(-1)^{1-m_F-F'} (-1)^{F'+J+I+1} \sqrt{(2J+1)(2F'+1)(2F+1)} \begin{Bmatrix} J & J' & 1 \\ F' & F & I \end{Bmatrix} \begin{pmatrix} F' & 1 & F \\ m'_F & q & -m_F \end{pmatrix}. \quad (2.46)$$

Now, for each $J \rightarrow J', F \rightarrow F'$ transition, we have the following part of the coefficient as a constant:

$$S_{FF'}(J, J') = \sqrt{(2F'+1)(2F+1)(2J+1)} \begin{Bmatrix} J & J' & 1 \\ F' & F & I \end{Bmatrix}. \quad (2.47)$$

Our coefficient turns into

$$S_{FF'}(J, J') (-1)^{J+I-m_F} \begin{pmatrix} F' & 1 & F \\ m'_F & q & -m_F \end{pmatrix}. \quad (2.48)$$

The square of this value is the relative probability of that particular transition happening. So for each $J \rightarrow J', F \rightarrow F'$ transition, we calculate the overall strength $S_{FF'}(J, J')$. We then look at the strength of the different $m_F \rightarrow m'_F$ transitions given different light polarizations q . The most important transition for us is the cooling/pumping transition $S_{1/2} \rightarrow P_{1/2}$. The branching ratios for this transition are given in Tables 2.3 through 2.5. For $^{133}\text{Ba}^+$ and $^{135}\text{Ba}^+ / ^{137}\text{Ba}^+$, all of the branching ratios are given in Tables A.1 through A.12.

Dipole Selection Rules

There are several situations where the Clebsch Gordan coefficients are zero, making these particular transitions impossible. These situations define the Selection Rules: constraints which give us the possible dipole transitions.

For fine structure dipole transitions, we are adding angular momenta $|J, m_J\rangle$ and $|k=1, q\rangle$. From Equation 2.22, we get the selection rule $J' = J$ or $J' = J \pm 1$.

Recalling that $m = m_1 + m_2$ for addition of angular momenta, we infer the selection rule: $m'_J = m_J$ or $m'_J = \pm m_J$.

Next, the Clebsch Gordan coefficient $\langle J, 0|J, 0, 1, q\rangle = 0$, leading to another selection rule: if $m'_J = m_J = 0$, then $J' \neq J$.

An obvious selection rule is $s' = s$, and $m'_s = m_s$, since dipole interactions don't change spin.

The final selection rule applies only when $s = 1/2$. Then we have from Equation 2.22

$$|c - 1/2| \leq J \leq l + 1/2.$$

And similar for J', l' , since spin obviously doesn't change from dipole radiation. Now suppose that $l' = l \pm 1$ and $J' = J \mp 1$. Then for the J' condition we get

$$|c - 1/2 \pm 1| \leq J \mp 1 \leq l + 1/2 \pm 1$$

$$|c - 1/2 \pm 1| \pm 1 \leq J \leq l + 1/2 \pm 2$$

For the positive and negative versions respectively, we get

$$l + 3/2 \leq J \leq l + 5/2$$

$$|c - 3/2| - 1 \leq J \leq l - 3/2.$$

Both of these contradict the first J, J' conditions, so we have the selection rule: If $s = 1/2$ then (If $l' = l \pm 1$ then $J' \neq J \mp 1$).

So overall we have the following fine structure selection rules

$$J' = J \text{ or } J' = J \pm 1 \quad (2.49)$$

$$m'_J = m_J \text{ or } m'_J = \pm m_J \quad (2.50)$$

$$\text{If } m'_J = m_J = 0, \text{ then } J' \neq J \quad (2.51)$$

$$s' = s \text{ and } m'_s = m_s \quad (2.52)$$

$$\text{If } l' = l \pm 1, \text{ then } J' \neq J \mp 1 \quad (s = 1/2). \quad (2.53)$$

For hyperfine structure, we have similar selection rules to Equations 2.49, 2.50, 2.51. Again the nuclear spin I doesn't change, so we have an additional selection rule similar to 2.52 but regarding I and m_I . Depending on the amount of electrons contributing to the angular momentum, we may or may not have a selection rule similar to Equation 2.53 for hyperfine structure.

$6S_{1/2} \leftrightarrow 6P_{1/2}, q = +1$			
$F = 1 \leftrightarrow F' = 1$			
m_F	0	1	
$m_{F'}$	-1	0	
	0.2887	0.2887	
$F = 1 \leftrightarrow F' = 2$			
	-1	0	1
	-2	-1	0
	-0.7071	-0.5000	-0.2887
$F = 2 \leftrightarrow F' = 1$			
	0	1	2
	-1	0	1
	0.2887	0.5000	0.7071
$F = 2 \leftrightarrow F' = 2$			
	-1	0	1
	-2	-1	0
	-0.4082	-0.5000	-0.4082

$6S_{1/2} \leftrightarrow 6P_{1/2}, q = -1$			
$F = 1 \leftrightarrow F' = 1$			
m_F	-1	0	
$m_{F'}$	0	1	
	-0.2887	-0.2887	
$F = 1 \leftrightarrow F' = 2$			
	-1	0	1
	0	1	2
	-0.2887	-0.5000	-0.7071
$F = 2 \leftrightarrow F' = 1$			
	-2	-1	0
	-1	0	1
	0.7071	0.5000	0.2887
$F = 2 \leftrightarrow F' = 2$			
	-2	-1	0
	-1	0	1
	0.4082	0.5000	0.4082

Table 2.3: $^{135}\text{Ba}^+ / ^{137}\text{Ba}^+$ dipole branching ratios: $6S_{1/2} \leftrightarrow 6P_{1/2}, q = +1$

Table 2.4: $^{135}\text{Ba}^+ / ^{137}\text{Ba}^+$ dipole branching ratios: $6S_{1/2} \leftrightarrow 6P_{1/2}, q = -1$

$6S_{1/2} \leftrightarrow 6P_{1/2}, q = 0$				
$F = 1 \leftrightarrow F' = 1$				
m_F	-1	0	1	
$m_{F'}$	-1	0	1	
	0.2887	0	-0.2887	
$F = 1 \leftrightarrow F' = 2$				
	-1	0	1	
	-1	0	1	
	0.5000	0.5774	0.5000	
$F = 2 \leftrightarrow F' = 1$				
	-1	0	1	
	-1	0	1	
	0.5000	0.5774	0.5000	
$F = 2 \leftrightarrow F' = 2$				
	-2	-1	0	1
	-2	-1	0	1
	-0.5774	-0.2887	0	0.2887
				0.5774

Table 2.5: $^{135}\text{Ba}^+ / ^{137}\text{Ba}^+$ dipole branching ratios: $6S_{1/2} \leftrightarrow 6P_{1/2}, q = 0$

2.2.2 Quadrupole Transitions

Transitions between S and D states can only be driven by quadrupole interaction. To get their transition probabilities, we must look at the $\langle F, m_F | \hat{r}_i \hat{r}_j | F', m'_F \rangle$ matrix element [28, 29] multiplied by the i th polarization component ϵ_i and the j th index of refraction component n_j . Let's start out by writing it in terms of Racah Tensor operators $c_{ij}^{(q)}$:

$$\langle F, m_F | \hat{r}_i \hat{r}_j | F', m'_F \rangle \epsilon_i n_j = \sum_{q=-2}^2 \langle F, m_F | r^2 C_q^{(2)} | F', m'_F \rangle c_{ij}^{(q)} \epsilon_i n_j. \quad (2.54)$$

Next, we use the Wigner Eckart Theorem 2.34, and the Wigner 3-j symbol notation to write

$$\langle F, m_F | \hat{r}_i \hat{r}_j | F', m'_F \rangle \epsilon_i n_j = \langle F || r^2 C^2 || F' \rangle \sum_{q=-2}^2 \begin{pmatrix} F & 2 & F' \\ -m_F & q & m'_F \end{pmatrix} c_{ij}^{(q)} \epsilon_i n_j. \quad (2.55)$$

Finally, we decompose the reduced matrix element

$$\langle F || r^2 C^2 || F' \rangle = (-1)^{F'+2+J+I} \sqrt{(2J+1)(2F'+1)} \begin{Bmatrix} 2 & J' & J \\ I & F & F' \end{Bmatrix} \langle J || r^2 C^2 || J' \rangle. \quad (2.56)$$

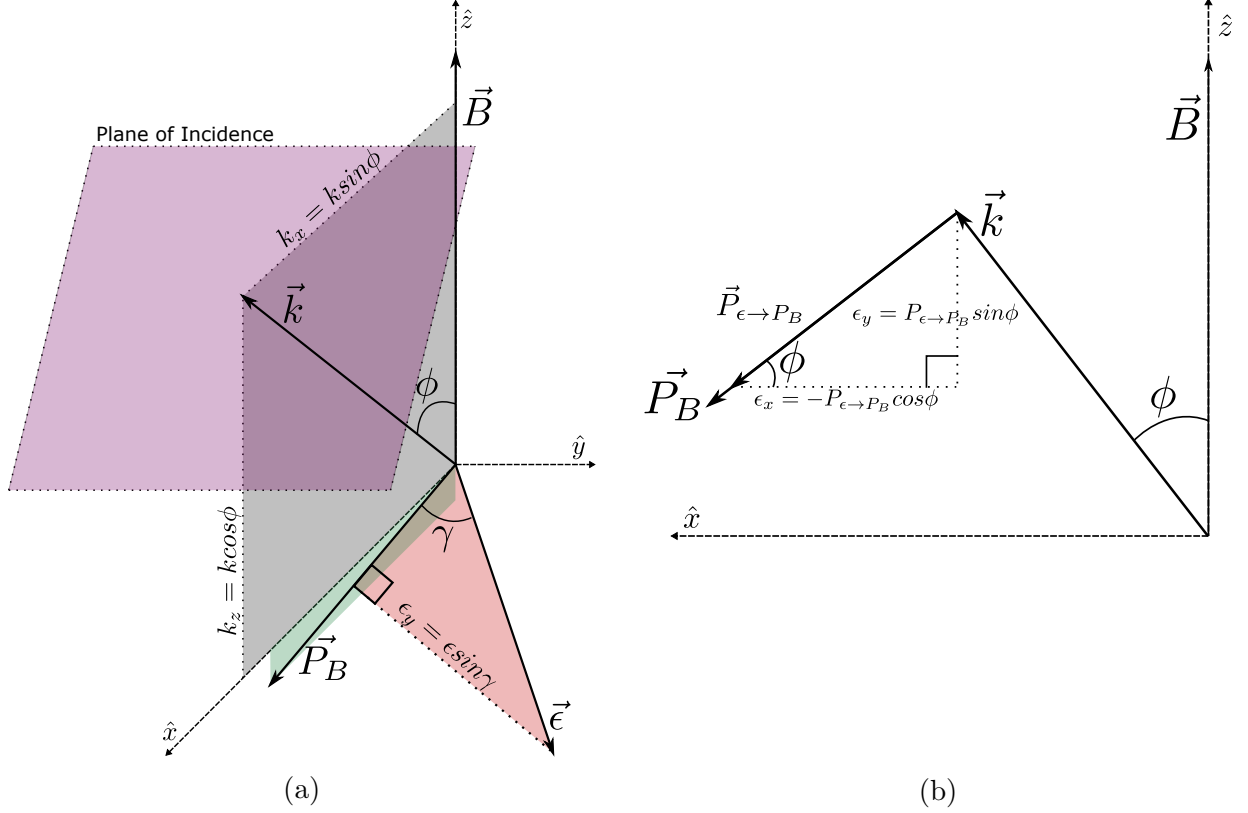


Figure 2.6: Quadrupole transition laser orientation: describing the magnetic field, wave vector, and polarization with ϕ and γ (a) magnetic field \vec{B} , wavevector \vec{k} , polarization $\vec{\epsilon}$, plane of incidence, and the negative projection of the magnetic field onto the plane of incidence \vec{P}_B . (b) projection of the polarization onto \vec{P}_B , labeled $\vec{P}_{\epsilon \rightarrow P_B}$.

The selection rules for Quadrupole transitions are quite a lot more work to derive, but they are analogous to the dipole selection rules:

$$F' = F \text{ or } F' = F \pm 1 \text{ or } F' = F \pm 2$$

$$m'_F = m_F \text{ or } m'_F = F \pm 1 \text{ or } m'_F = m_F \pm 2. \quad (2.57)$$

We can describe the wave vector ($k = \omega n/c$) and the polarization with just two angles ϕ and γ . We first define the coordinate system by the magnetic field so that $B = B_0 \hat{z}$. Next, we can choose the wave vector to be confined to the $x - z$ plane, and define ϕ as the angle between the magnetic field and the wave vector. From Figure 2.6a, we see that the wave vector is $\vec{k} = k(\sin \phi \hat{x} + \cos \phi \hat{z})$. In order to define γ we first project the magnetic field onto the plane of incidence shown in Figure 2.6(a). We define γ as the angle between the negative vector of this projection (Shown as \vec{P}_B) and the polarization $\vec{\epsilon}$. From Figure

2.6(b), we see that $\vec{\epsilon} = \cos \gamma \cos \phi \hat{x} + \sin \gamma \hat{y} + \cos \gamma \sin \phi \hat{z}$. Overall, we have

$$\vec{k} = \begin{pmatrix} \sin \phi \\ 0 \\ \cos \phi \end{pmatrix}, \quad \vec{\epsilon} = \begin{pmatrix} \cos \gamma \cos \phi \\ \sin \gamma \\ \cos \gamma \sin \phi \end{pmatrix}. \quad (2.58)$$

Now, we can look at the directionally dependent part of the matrix element: $g^a \equiv c_{ij}^a \epsilon_i n_j = \frac{1}{k} c_{ij}^a \epsilon_i k_j$. We first write out all possibilities for $\frac{1}{k} \epsilon_i k_j$:

$$\begin{aligned} \epsilon_i k_y &= 0 \\ \epsilon_x k_z &= k \cos \gamma \cos \phi \cos \phi = k \cos \gamma \cos^2 \phi \\ \epsilon_z k_x &= -k \cos \gamma \sin \phi \sin \phi = -k \cos \gamma \sin^2 \phi \\ \epsilon_y k_x &= k \sin \phi \sin \gamma \\ \epsilon_y k_z &= k \cos \phi \sin \gamma \\ \epsilon_x k_x &= k \cos \gamma \sin \phi \cos \phi = k \cos \gamma \sin 2\phi \\ \epsilon_z k_z &= -k \cos \gamma \cos \phi \sin \phi = -k \cos \gamma \sin 2\phi. \end{aligned}$$

The Racah Tensors can be written as the following:

$$c_{ij}^{(0)} = \frac{1}{3} \begin{pmatrix} -1 & 0 & 0 \\ 0 & -1 & 0 \\ 0 & 0 & 2 \end{pmatrix}, \quad c_{ij}^{(\pm 1)} = \frac{1}{\sqrt{6}} \begin{pmatrix} 0 & 0 & \mp 1 \\ 0 & 0 & i \\ \mp 1 & i & 0 \end{pmatrix}, \quad c_{ij}^{(\pm 2)} = \frac{1}{\sqrt{6}} \begin{pmatrix} 1 & \mp i & 0 \\ \mp i & -1 & 0 \\ 0 & 0 & 0 \end{pmatrix}. \quad (2.59)$$

So for the rank zero geometrical operator elements, we have

$$\begin{aligned} g_{xx}^{(0)} &= \frac{-1}{3} \cos \gamma \sin 2\phi \\ g_{zz}^{(0)} &= \frac{-2}{3} \cos \gamma \sin 2\phi. \end{aligned}$$

And finally for the overall operator, we have

$$g^{(0)} = |g_{xx}^{(0)} + g_{zz}^{(0)}| = \frac{1}{2} |\cos \gamma \sin 2\phi|. \quad (2.60)$$

For the rank one geometrical operator elements, we have

$$\begin{aligned} g_{xz}^{(\pm 1)} &= \frac{\mp 1}{\sqrt{6}} \cos \gamma \cos^2 \phi \\ g_{zx}^{(\pm 1)} &= \frac{\pm 1}{\sqrt{6}} \cos \gamma \sin^2 \phi \\ g_{yz}^{(\pm 1)} &= \frac{i}{\sqrt{6}} \sin \gamma \cos \phi, \end{aligned}$$

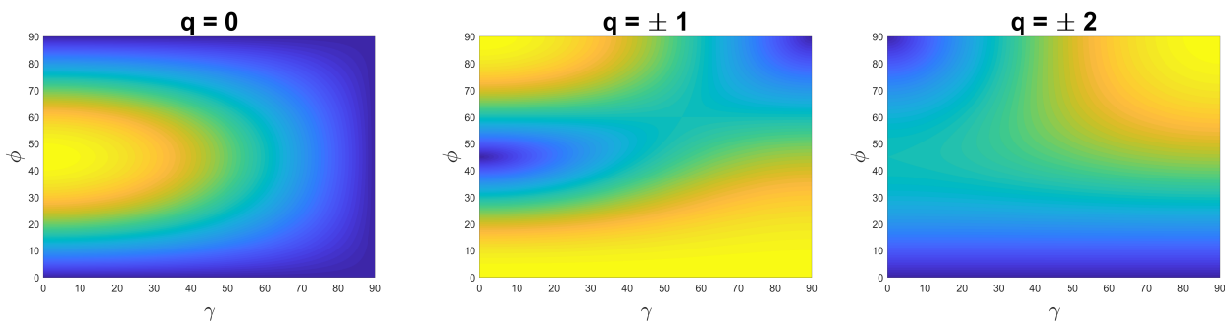


Figure 2.7: Quadrupole geometrical constants: yellow areas have a high probability of driving the transition and blue areas have a low probability. Two orientations are notable: $\phi = 45^\circ$, $\gamma = 0^\circ$ and $\phi = 90^\circ$, $\gamma = 90^\circ$.

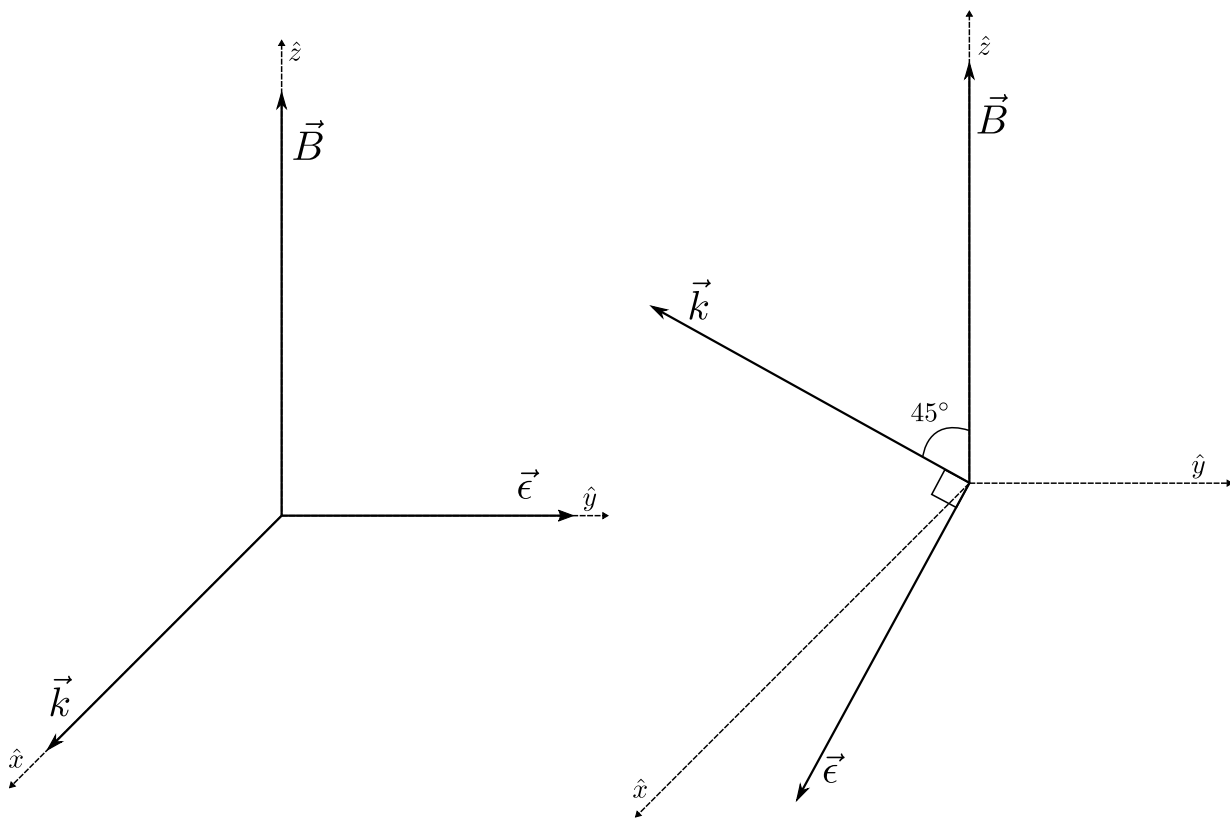


Figure 2.8: Quadrupole useful orientations: (a) $\phi = 90^\circ$, $\gamma = 90^\circ$: only $m \rightarrow m \pm 2$ transitions coupled (b) $\phi = 45^\circ$, $\gamma = 0^\circ$: $m \rightarrow m$ strongly coupled, $m \rightarrow m \pm 2$ weakly coupled.

and for the overall operator, we get

$$\begin{aligned} g^{(\pm 1)} &= |g_{xz}^{(\pm 1)} + g_{zx}^{(\pm 1)} + g_{yz}^{(\pm 1)}| = \frac{1}{\sqrt{6}} |i \sin \gamma \cos \phi \mp \cos \gamma (\cos^2 \phi - \sin^2 \phi)| \\ &= \frac{1}{\sqrt{6}} |\mp \cos \gamma \cos 2\phi + i \sin \gamma \cos \phi|. \end{aligned} \quad (2.61)$$

Similarly, for the rank two geometrical operator elements, we have

$$\begin{aligned} g_{xx}^{(\pm 2)} &= \frac{1}{2\sqrt{6}} \cos \gamma \sin 2\phi \\ g_{yx}^{(\pm 2)} &= \frac{\mp i}{\sqrt{6}} \sin \gamma \sin \phi. \end{aligned}$$

And for the overall operator, we get

$$g^{(\pm 2)} = |g_{xx}^{(\pm 2)} + g_{yx}^{(\pm 2)}| = \frac{1}{\sqrt{6}} \left| \frac{1}{2} \cos \gamma \sin 2\phi \mp i \sin \gamma \sin \phi \right|. \quad (2.62)$$

In summary, all of the geometrical operators are

$$\begin{aligned} g^{(0)} &= \frac{1}{2} |\cos \gamma \sin 2\phi| \\ g^{(\pm 1)} &= \frac{1}{\sqrt{6}} |\mp \cos \gamma \cos 2\phi + i \sin \gamma \cos \phi| \\ g^{(\pm 2)} &= |g_{xx}^{(\pm 2)} + g_{yx}^{(\pm 2)}| = \frac{1}{\sqrt{6}} \left| \frac{1}{2} \cos \gamma \sin 2\phi \mp i \sin \gamma \sin \phi \right|. \end{aligned} \quad (2.63)$$

As can be seen from Figure 2.7, there are two particularly useful orientations. If $\phi = 90^\circ$ and $\gamma = 90^\circ$, then only the $m \rightarrow m \pm 2$ transitions are coupled. We call this orientation orthogonal. If $\phi = 45^\circ$ and $\gamma = 0^\circ$, the $m \rightarrow m$ transitions are strongly coupled while the $m \rightarrow m \pm 2$ transitions are weakly coupled and $m \rightarrow m \pm 1$ are completely suppressed. We call this orientation XZ. The polarizations and wave vectors for these orientations are shown in Figure 2.8.

Overall, when looking at $J \leftrightarrow J'$ transitions, the coefficient we care about is

$$(-1)^{F'} \sqrt{2F' + 1} \begin{Bmatrix} 2 & J' & J \\ I & F & F' \end{Bmatrix} \sum_{q=-2}^2 \begin{pmatrix} F & 2 & F' \\ -m_F & q & m'_F \end{pmatrix} c_{ij}^{(q)} \epsilon_i n_j. \quad (2.64)$$

So for the branching ratios, we look at Equation 2.64 and the geometrical constants in Equation 2.63. For averaged values, you just assume that the geometrical constant is equal to 1. For $^{133}\text{Ba}^+$ and $\text{Ba } ^{135}\text{Ba}^+ / ^{137}\text{Ba}^+$, these branching ratios are displayed in Tables A.13 through A.24 for the case of averaged and the two interesting orientations we mentioned earlier. In particular, for the shelving transition useful in chapter 3, the XZ orientation branching ratios are displayed here in Table 2.6.

$6S_{1/2} \leftrightarrow 5D_{5/2}$										
$\phi = 45^\circ, \gamma = 0^\circ$										
$F = 1 \leftrightarrow F' = 1$										
m_F	-1	-1	0	1	1	1	1	1	1	
$m_{F'}$	-1	1	0	-1	1					
	0.0354	0.0354	0.0707	0.0354	0.0354					
$F = 1 \leftrightarrow F' = 2$										
	-1	-1	0	0	1	1	1	1	1	
	-1	1	-2	2	-1	1				
	0.0697	0.0232	0.0329	-0.0329	-0.0232	-0.0697				
$F = 1 \leftrightarrow F' = 3$										
	-1	-1	0	0	1	1	1	1	1	
	-3	1	-2	0	2	-1	1	3		
	0.0304	0.0471	0.0079	-0.0176	-0.0577	-0.0176	0.0079	0.0471	0.0304	
$F = 1 \leftrightarrow F' = 4$										
Forbidden										
$F = 2 \leftrightarrow F' = 1$										
	-2	-1	-1	1	1	1	2			
	0	-1	1	-1	1	0				
	0.0075	0.0158	-0.0053	0.0053	-0.0158	-0.0075				
$F = 2 \leftrightarrow F' = 2$										
	-2	-1	0	0	1	1	2	2		
	-2	1	-2	0	2	-1	1	0	2	
	0.0267	0.0109	0.0134	0.0109	-0.0267	0.0109	-0.0134	0.0134	0.0109	0.0267
$F = 2 \leftrightarrow F' = 3$										
	-2	-1	-1	0	0	1	1	2	2	
	-2	0	-3	1	-2	2	-1	3	0	2
	0.05	0.0091	0.0204	-0.0316	-0.0204	0.0204	0.0158	0.0316	-0.0204	-0.0091
										-0.05
$F = 2 \leftrightarrow F' = 4$										
	-2	-2	-1	-1	0	0	1	1	2	2
	-2	0	-3	-1	1	-2	2	-1	3	0
	0.0373	0.0045	-0.0264	-0.0598	-0.01	0.0173	0.0655	0.0173	-0.01	-0.0598
										-0.0264
										0.0045
										0.0423
										0.0373

Table 2.6: $^{135}\text{Ba}^+ / ^{137}\text{Ba}^+$ quadrupole branching ratios: XZ orientation

2.3 Saturation Intensity

As we drive a two-level system with more power, the average population in the excited state increases. However, the population asymptotes at 0.5, giving diminishing gains as we increase the power. Furthermore, the linewidth of the transition increases with the power after a point called the saturation point [27, 30].

For a two-level system, the Hamiltonian can be written as

$$\hat{H} = \hbar \begin{bmatrix} 0 & \Omega e^{i\omega t}/2 \\ \Omega e^{-i\omega t}/2 & \omega_0 \end{bmatrix}, \quad (2.65)$$

where Ω is the Rabi frequency of the transition, ω is the frequency of the laser, and ω_0 is the frequency of the transition between the two levels. Solving Schrödinger's equation, and going into a rotating frame $\tilde{c}_e = c_e e^{i\omega t}$, where c_i are populations of the levels, we end up with the following differential equations:

$$\begin{aligned} \frac{\partial}{\partial t} c_g &= -\frac{i\Omega}{2} \tilde{c}_e \\ \frac{\partial}{\partial t} \tilde{c}_e &= i\Delta \tilde{c}_e - \frac{i\Omega}{2} c_g. \end{aligned} \quad (2.66)$$

The population dynamics of driving a two-level system depends on how the spontaneous emission from the excited state balances the stimulated absorption driven by the laser. Spontaneous emission is much easier to model if we switch to the density matrix formulation for the populations:

$$\begin{aligned} \tilde{\rho}_{gg} &= c_g c_g^* = \rho_{gg} \\ \tilde{\rho}_{ee} &= \tilde{c}_e \tilde{c}_e^* = c_e c_e^* = \rho_{ee} \\ \tilde{\rho}_{ge} &= c_g \tilde{c}_e^* = c_g c_e^* e^{-i\omega t} = \rho_{ge} e^{-i\omega t} \\ \tilde{\rho}_{eg} &= \tilde{c}_e c_g^* = c_e c_g^* e^{i\omega t} = \rho_{eg} e^{i\omega t}. \end{aligned} \quad (2.67)$$

The ρ_{ii} terms are called the populations, and the ρ_{ij} terms are called the coherences.

Now, we can take the derivatives and substitute Equation 2.66 to get the following differential equations:

$$\begin{aligned} \frac{\partial}{\partial t} \rho_{gg} &= -\frac{i\Omega}{2} (\tilde{\rho}_{eg} - \tilde{\rho}_{ge}) \\ \frac{\partial}{\partial t} \rho_{ee} &= \frac{i\Omega}{2} (\tilde{\rho}_{eg} - \tilde{\rho}_{ge}) \\ \frac{\partial}{\partial t} \tilde{\rho}_{eg} &= i\Delta \tilde{\rho}_{eg} + \frac{i\Omega}{2} (\tilde{\rho}_{ee} - \tilde{\rho}_{gg}) \\ \frac{\partial}{\partial t} \tilde{\rho}_{ge} &= -i\Delta \tilde{\rho}_{ge} - \frac{i\Omega}{2} (\tilde{\rho}_{ee} - \tilde{\rho}_{gg}). \end{aligned} \quad (2.68)$$

We can a priori introduce spontaneous emission as follows:

$$\begin{aligned}
\frac{\partial}{\partial t}\rho_{gg} &= -\frac{i\Omega}{2}(\tilde{\rho}_{eg} - \tilde{\rho}_{ge}) + \Gamma\rho_{ee} \\
\frac{\partial}{\partial t}\rho_{ee} &= \frac{i\Omega}{2}(\tilde{\rho}_{eg} - \tilde{\rho}_{ge}) - \Gamma\rho_{ee} \\
\frac{\partial}{\partial t}\tilde{\rho}_{eg} &= (i\Delta - \gamma_{\perp})\tilde{\rho}_{eg} + \frac{i\Omega}{2}(\tilde{\rho}_{ee} - \tilde{\rho}_{gg}) \\
\frac{\partial}{\partial t}\tilde{\rho}_{ge} &= (-i\Delta - \gamma_{\perp})\tilde{\rho}_{ge} - \frac{i\Omega}{2}(\tilde{\rho}_{ee} - \tilde{\rho}_{gg}).
\end{aligned} \tag{2.69}$$

These are called the Optical Bloch Equations, and the decay rates Γ and γ_{\perp} are called the longitudinal and transverse decay rates respectively. In general, the transverse decay rate can be written as $\gamma_{\perp} = \Gamma/2 + \gamma_c$, where γ_c is a generic term for any form of decay besides spontaneous emission. For our discussion, we assume that $\gamma_c = 0$.

A useful quantity to define is the population difference w between the levels, so that

$$\frac{\partial}{\partial t}w = -\left(\frac{\partial}{\partial t}\rho_{ee} - \frac{\partial}{\partial t}\rho_{gg}\right) = \dots = -i\Omega(\tilde{\rho}_{eg} - \tilde{\rho}_{eg}^*) + \Gamma - \Gamma w. \tag{2.70}$$

Finally, we assume that we have a steady state, so that all derivatives are equal to zero. After some substitution, we can solve for our population difference at steady state:

$$w = \frac{1}{1 + s},$$

where

$$s = \frac{\Omega^2}{2\Gamma^2(1/4 + \frac{\Delta^2}{\Gamma^2})} = \frac{s_0}{\left(1 + \left(\frac{2\Delta}{\Gamma}\right)^2\right)} \tag{2.71}$$

is the saturation parameter. The total scattering rate is given by

$$\gamma_p = \Gamma\rho_{ee} = \Gamma\frac{1}{2}(1 + w) = \frac{s_0\Gamma/2}{1 + \left(\frac{\Delta}{\gamma_{\perp}}\right)^2 + s_0}. \tag{2.72}$$

If we assume that our laser has a high intensity, we can approximate the denominator as

$$1 + \left(\frac{\Delta}{\gamma_{\perp}}\right)^2 + s_0 \approx (1 + s_0) \left(1 + \left(\frac{\Delta}{\gamma_{\perp}}\right)^2\right),$$

giving us the result of

$$\gamma_p = \left(\frac{s_0}{1 + s_0}\right) \left(\frac{\Gamma/2}{1 + \left(\frac{\Delta}{\gamma_{\perp}}\right)^2}\right), \tag{2.73}$$

where $\gamma'_\perp = \gamma_\perp \sqrt{1 + s_0}$ is the power broadened linewidth. So as we increase the power, the linewidth of the transition is increased. Using more power to collect more scattered light has a disadvantage of broadening the linewidth of the transition. This is undesirable because it could make it harder to select certain transitions and perform Doppler cooling. So we need to make sure the intensity we are applying to our ions is reasonably low.

We assume that our detuning is zero $\Delta = 0$, $s = s_0$; we can define saturation intensity as

$$s = \frac{I}{I_s} = \frac{2\Omega^2}{\Gamma^2}. \quad (2.74)$$

Noting that $\Omega = -\langle 0 | \hat{\epsilon} \cdot \vec{d} | 1 \rangle E_0 / \hbar$, and $I = (\epsilon_0 c / 2) E_0^2$ (where $\hat{\epsilon}$ is the polarization of the field and \vec{d} is the dipole moment of the electron), we can solve for the saturation intensity:

$$I_s = \frac{c \epsilon_0 \Gamma^2 \hbar^2}{4 |\langle 0 | \hat{\epsilon} \cdot \vec{d} | 1 \rangle|^2}. \quad (2.75)$$

Lastly, we make use of an expression for the longitudinal decay rate that comes from a full quantum electrodynamics treatment:

$$\Gamma = \frac{\omega_0^2}{\pi \epsilon_0 c^2 \hbar} |\langle 0 | \hat{\epsilon} \cdot \vec{d} | 1 \rangle|^2, \quad (2.76)$$

where c is the speed of light. This equation assumes that we're using linearly polarized light. There is a way to derive this form simply using the formalism we've already developed, however it must be assumed that there is strong collisional damping, so that $\gamma_\perp \gg \Omega, \Gamma$. It just turns out from quantum electrodynamics that this form holds even without this approximation. Using Equation 2.76, we end up with the saturation intensity

$$I_s = \frac{\hbar \Gamma \omega_0^2}{4 \pi c^2}. \quad (2.77)$$

Assuming a focused beam waist of $30 \mu\text{m}$ at the barium ions, the saturation intensity for the 493 nm, 553 nm, 614 nm, and 650 nm transitions are $0.62 \mu\text{W}$, $0.416 \mu\text{W}$, $0.397 \mu\text{W}$, and $0.207 \mu\text{W}$ respectively. In the lab, these powers are a good guideline to aim for to get optimal performance.

2.4 Isotope Selectivity

There are many different ways to ionize a neutral atom for trapping in an ion trap, including electron bombardment, applying strong electric fields, and using lasers. We chose to use a two-step laser ionization process to ionize barium because of the isotope selectivity it offers. Natural barium has many stable isotopes, with the highest abundance being $^{138}\text{Ba}^+$ at 72%; this ion is useful for calibration and as a Zeeman qubit. $^{137}\text{Ba}^+$, at an abundance

Level	First Step		Second Step	
	Wavenumber(cm ⁻¹)	Wavelength (nm)	Wavenumber(cm ⁻¹)	Wavelength(nm)
$6s^2\ ^1S_0$	0	-	42034.91	237.8975
$6s6p\ ^1P_1$	18060.261	553.7019	23974.649	417.1073
$5d6p\ ^3D_1$	24192.033	413.3592	17842.877	560.4477
$6s6p\ ^3P_1$	12636.623	791.3507	29398.287	340.1559
ionized	42034.91	237.8975	0	-

Table 2.7: Barium ionization energy levels: in the first step, we drive a coherent transition to an intermediate state. In the second step, we eject the electron with a laser of higher frequency than listed. [16,31]

of 11%, is useful because it's relatively common and has a nuclear spin of 3/2, giving us up to eight hyperfine levels to work with. $^{133}\text{Ba}^+$ is a radioactive isotope with a half-life of ~ 10 years; it has a nuclear spin of 1/2 making it an excellent choice for a qubit.

The energy needed to ionize neutral barium corresponds to a laser wavelength of around 238 nm - very low in the UV range. UV beams are more difficult to work with, giving us another reason to use a two-step ionization process. There are hundreds of different intermediate levels that we can use. Table 2.7 shows many different intermediate levels for this two-step ionization process. The first step of the ionization has to be coherent and resonant so that we reliably transfer to the intermediate state, but the second step can be a cheap, noisy, incoherent laser: the wavelength of which just needs to be lower than the wavelengths listed in Table 2.7. We chose to use the 553 nm ionization scheme with a 405 nm second step ionization laser, because the first step transition is the fastest transition based on selection rules; this allows us to ionize and trap more quickly.

It turns out that different isotopes of neutral barium have a slight isotope shift on the coherent 553 nm transition. If the linewidth of our laser is small enough, this allows us to essentially pick which isotope we wish to ionize.

The position of the different resonances are shown in Figure 2.9. $^{138}\text{Ba}^+$ has the lowest frequency, and is the easiest to trap. One thing to note is that $^{135,137}\text{Ba}^+$ both have three different hyperfine levels on this transition, since the nuclear spin is 3/2. The frequencies of all of these transitions are shown in Table 2.8.

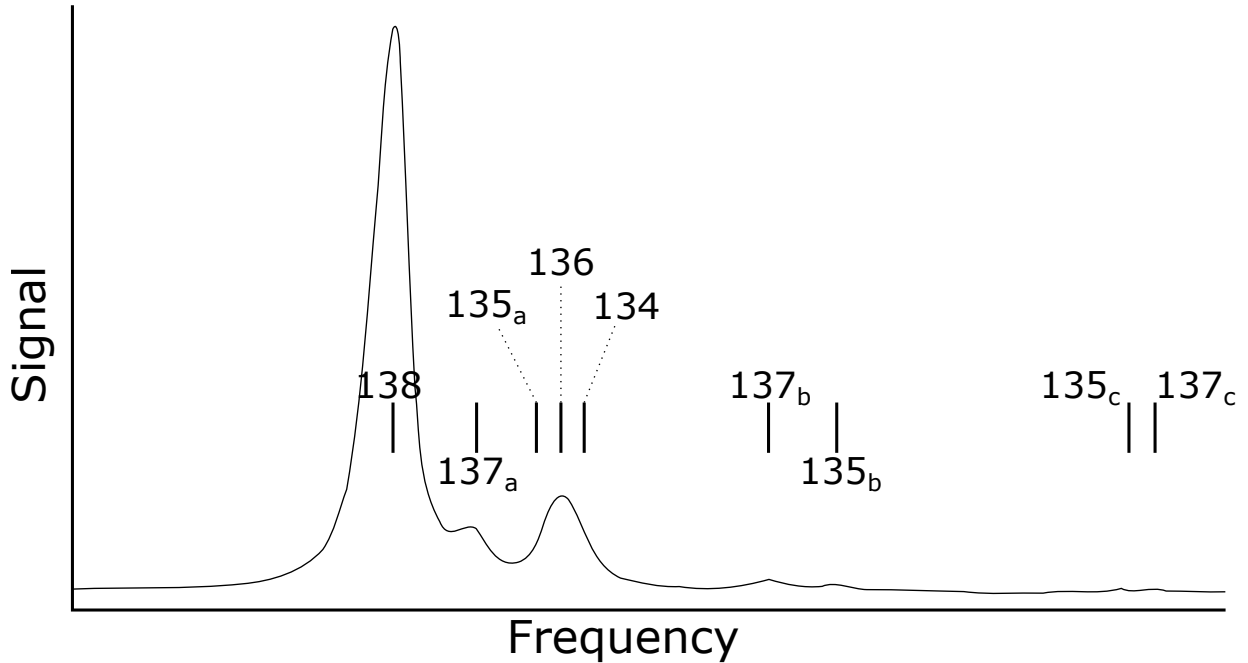


Figure 2.9: Natural barium transition spectrum: each isotope has a shifted first-step ionization frequency, allowing us to select which isotope we wish to ionize and trap. a, b, and c mean hyperfine level $F = 5/2, 3/2, 1/2$ respectively. Adapted from reference [32].

Isotope	Freq. (MHz)	Isotope	Freq. (MHz)	Isotope	Freq. (MHz)
$^{133}\text{g}(1/2)$	-23.3	134	142.8	$^{137}(3/2)$	274.56
138	0	132	167.9	$^{135}(3/2)$	323.44
$^{131}(1/2)$	0	$^{133}\text{m}(1/2)$	172.9	$^{131}(3/2)$	373.8
$^{137}(5/2)$	63.43	$^{133}\text{m}(3/2)$	216.55	$^{133}\text{g}(3/2)$	386.65
$^{135}(5/2)$	120.55	131	249.2	$^{137}(1/2)$	549.47
136	128.02	128	271.1	$^{135}(1/2)$	549.47

Table 2.8: Ionization selectivity: exact frequencies of the first step ionization transition for different isotopes of barium. The hyperfine structure of the 135 and 137 isotopes give us three different transitions each. The center-of-mass of these transitions are also given. g and m states are the ground and excited nuclear states. [32–35]

Qudit Measurement

In this chapter, I discuss a method for measuring out the state of qudits with a shelving scheme, which utilizes a metastable state with a long lifetime to store qudit states during measurement. This work is also described in a paper co-written with Pei-Jiang Low describing all the protocols necessary for doing qudit quantum computation with $^{137}\text{Ba}^+$ [36].

3.1 Shelving

State measurement for trapped ion qubits is typically done by driving a closed transition on one of the qubit states and collecting the fluorescence on a detector. A closed transition is one in which the set of energy levels involved does not overlap with the other qubit state. For $^{137}\text{Ba}^+$, if we encode each qubit state into one of the hyperfine states, we can do this by driving the $S_{1/2} \leftrightarrow P_{3/2}$ transition. We can either drive the $F = 2$ qubit to the $F = 3$ $P_{3/2}$ state, or the $F = 1$ qubit to the $F = 0$ $P_{3/2}$ state. When we consider qudits with more than two levels, we see that we cannot drive a closed transition on each qudit state using fluorescence.

Our solution is to use the metastable $D_{5/2}$ state to “shelve” the qudit state. This state has a long lifetime of ~ 30 s, and when we store states there, they are no longer driven by the fluorescence laser. The shelving approach to measuring a qudit is illustrated in Figure 3.1 for 3-levels. It consists of shelving all but one state in the metastable state, measuring the remaining state, then repeatedly de-shelving and measuring states until the overall state of the qudit is completely known.

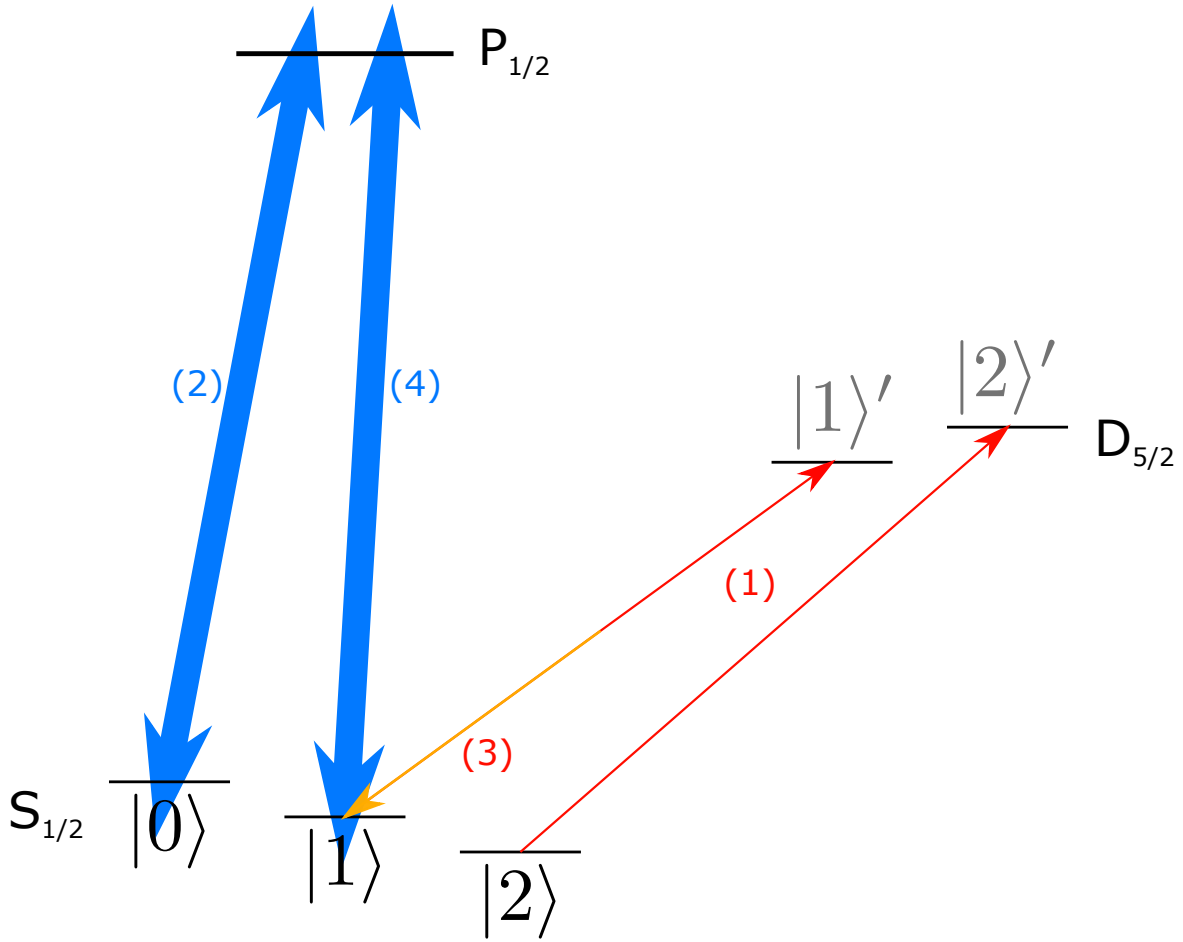


Figure 3.1: Shelving procedure: three-level qudit. (1): Map states $|1\rangle, |2\rangle$ to the metastable state. (2): Fluoresce on the cycling transition $S_{1/2} \leftrightarrow P_{1/2}$. (3): If no fluorescence detected, return one state from the metastable state and (4): measure it with fluorescence.

			$D_{5/2}$								
			$F' = 1$		$F' = 2$						
			-1	0	1	-2	-1	0	1	2	
			91.7507785	105.727	119.265	19.191	25.977	33.139	40.537	48.0933	
$S_{1/2}$	$F = 1$	-1	5020.300	4020.051	4034.027	4047.565	3947.490	3954.277	3961.439	3968.837	3976.393
		0	5023.594	4023.345	4037.322	4050.859	3950.785	3957.571	3964.733	3972.131	3979.687
	$F = 2$	1	5026.886	4026.637	4040.613	4054.151	3954.076	3960.863	3968.024	3975.423	3982.979
		-2	3007.567	4007.817	3993.840	3980.302	4080.377	4073.590	4066.429	4059.030	4051.474
	$F = 2$	-1	3010.864	4011.114	3997.137	3983.599	4083.674	4076.887	4069.726	4062.327	4054.771
		0	3014.159	4014.408	4000.431	3986.894	4086.968	4080.181	4073.020	4065.621	4058.065
		1	3017.450	4017.699	4003.723	3990.185	4090.260	4083.473	4076.312	4068.913	4061.357
		2	3020.739	4020.988	4007.012	3993.474	4093.548	4086.762	4079.600	4072.202	4064.646

Table 3.1: Shelving transitions: the units are in MHz. We set the carrier to $-1090MHz$ detuned from the $^{138}\text{Ba}^+$ transition; the transitions listed are relative to the carrier. The blue transitions are what we wish to drive for the shelving procedure. The yellow transitions have frequencies within $1MHz$ of one of the desired transitions. However, these can be suppressed (see text). The red transitions are within $20MHz$ of the shelving transitions, have nonzero Clebsch-Gordan coefficients, and cannot be suppressed by polarization, so we must consider the errors from indirectly driving them.

From Figure 2.5, we see that the $F = 3, 4$ levels in the metastable state overlap one another quite a bit. So we chose to use only the $F = 1, 2$ levels to store our qudit states. We transfer each F, m_F state in the $6S_{1/2}$ level to the $F' = F, m'_F = m_F$ state in the $5D_{5/2}$ level. Table 3.1 shows these transitions in blue, along with all of the other possible transitions. Note that we set the carrier to be $-1090MHz$ detuned from the $^{138}\text{Ba}^+$ transition. This was chosen so that we could hit all of the transitions within a window of less than 200 MHz, and the transitions don't run into each other at all. The yellow transitions have frequencies near one of the desired transitions, and will reduce our transfer probability. However, if we orient our shelving beam to be in the $\phi = 45^\circ, \gamma = 0^\circ$ direction, these transitions are completely suppressed, as shown in section 2.2.2, Figures 2.7. Transitions in red are not suppressed by this technique, so there will be off-resonant coupling to these.

Next, we need to decide how to perform these population transfers from the ground state $|g\rangle$ to the metastable state $|e\rangle$. We propose to use rapid adiabatic passage, since it's very robust against frequency noise, amplitude noise, and timing errors. A similar scheme was used in [37] for $^{138}\text{Ba}^+$.

Adiabatic passage works as follows: start by driving the transition off-resonantly with detuning from the transition $\Delta(0) = \omega(0) - \omega_0$, where $\omega(t)$ is the laser frequency at time t and ω_0 is the transition frequency. Next, sweep the detuning $\Delta(t) = \omega(t) - \omega_0$ through resonance, stopping at $-\Delta(0)$. For a 2-level system, the Hamiltonian in the rotating frame $\tilde{H} = UHU^\dagger + i\hbar(\frac{\partial U}{\partial t})U^\dagger$ (where $U = \exp\left(i\int_0^t \omega(t')dt'\right)$) can be written as

$$\tilde{H} = \hbar \begin{bmatrix} 0 & \Omega/2 \\ \Omega/2 & -\Delta(t) \end{bmatrix}, \quad (3.1)$$

where Ω is the resulting Rabi frequency of the transition. The eigenstates of the system are called the adiabatic or dressed states. The eigenvalues of this Hamiltonian are

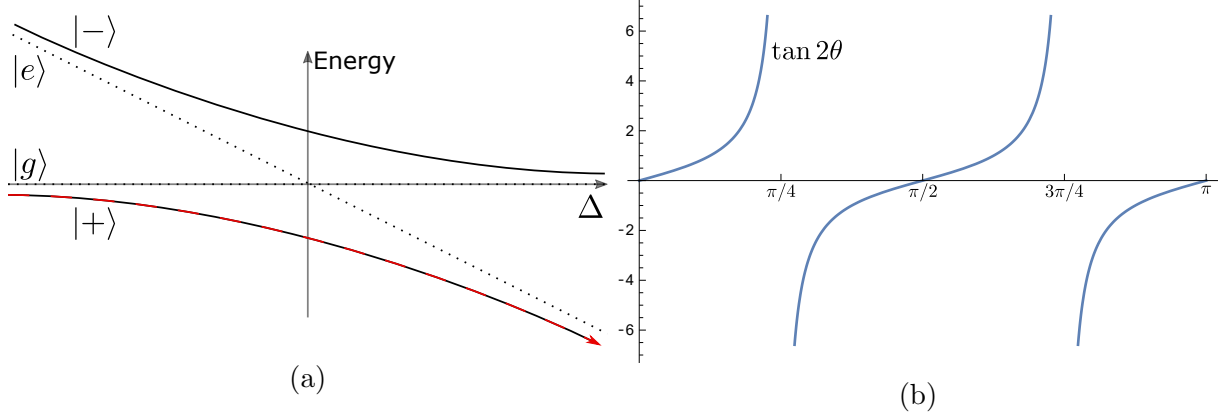


Figure 3.2: Adiabatic passage: (a) diabatic and adiabatic states energy vs detuning Δ . There's an avoided crossing between the adiabatic states. (b) Graph of $\tan 2\theta$

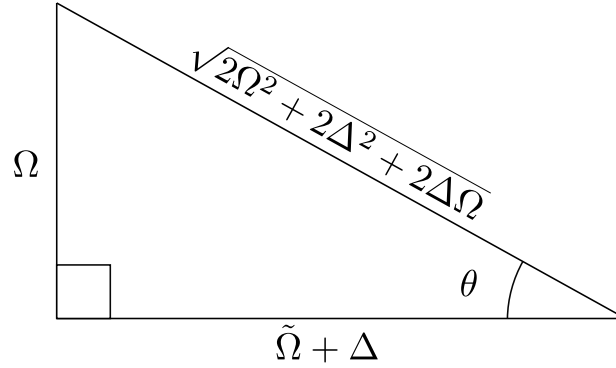


Figure 3.3: Adiabatic passage triangle

$\lambda_{\pm} = \frac{\Delta(t)}{2} + \frac{\tilde{\Omega}}{2}$, where $\tilde{\Omega} = \sqrt{\Delta^2 + \Omega^2}$ is the effective Rabi frequency. These are the energies of each adiabatic state. The adiabatic states can be written as

$$\begin{aligned} |+\rangle &= \sin \theta |g\rangle + \cos \theta |e\rangle \\ |-\rangle &= \cos \theta |g\rangle - \sin \theta |e\rangle, \end{aligned} \quad (3.2)$$

where θ is defined in Figure 3.3. Using trigonometric identities, we can simplify and write θ as $\tan 2\theta = \frac{\Omega}{\Delta}$. We can also get the diabatic state $|g\rangle$ ($|e\rangle$) in terms of the adiabatic states. This is done by multiplying one state by $\sin \theta$ ($\cos \theta$), the other by $\cos \theta$ ($\sin \theta$) and adding (subtracting) them from each other. The result is

$$\begin{aligned} |g\rangle &= \sin \theta |+\rangle + \cos \theta |-\rangle \\ |e\rangle &= \cos \theta |+\rangle - \sin \theta |-\rangle. \end{aligned} \quad (3.3)$$

In adiabatic passage, we start with a large detuning so that $|\Delta| \gg \Omega$. From Figure 3.2(a), we see that the $| \pm \rangle$ adiabatic states approach the $|g\rangle$ ($|e\rangle$) state for $\mp \Delta$. We see the

same thing if we consider the trigonometric tan graph in Figure 3.2(b): If we sweep the detuning adiabatically, then we will remain in the adiabatic state, following the solid lines in Figure 3.2(a), and transferring population between the ground and metastable states.

Finally, what exactly does it mean to sweep the frequency adiabatically? The Adiabatic Theorem tells us that the adiabatic regime for a two-level system is defined by [38]

$$\frac{1}{2} \left| \dot{\Omega}\Delta - \Omega\dot{\Delta} \right| \ll (\Omega^2 + \Delta^2)^{3/2}. \quad (3.4)$$

So for our two-level system with only the detuning varying linearly with α , and starting with a detuning $\Delta(0)$, we have

$$\frac{1}{2}\Omega\alpha \ll (\Omega^2 + \Delta(0)^2)^{3/2}. \quad (3.5)$$

Essentially, we need to perform the sweep slowly, and have a comparatively large initial detuning and/or Rabi frequency.

3.2 Errors

Using Schrödinger's equation $i\hbar\frac{\partial}{\partial t}|\psi\rangle = \hat{H}|\psi\rangle$, we get the following differential equations for the ground and excited states:

$$\begin{aligned} \frac{\partial}{\partial t}c_g &= -\frac{i\Omega}{2}\tilde{c}_e \\ \frac{\partial}{\partial t}\tilde{c}_e &= i\Delta(t)\tilde{c}_e - \frac{i\Omega}{2}c_g, \end{aligned} \quad (3.6)$$

where $\tilde{c}_e = c_e e^{i\int_0^t \omega(t')dt'}$ is the rotating frame excited population and c_g and c_e are the populations of the ground and excited states respectively.

We can take derivatives and substitute to end up with the following decoupled differential equations

$$\begin{aligned} \left(\frac{\partial^2}{\partial t^2} - i\Delta(t)\frac{\partial}{\partial t} + \frac{\Omega^2}{4} \right) c_g &= 0 \\ \left(\frac{\partial^2}{\partial t^2} - i\Delta(t)\frac{\partial}{\partial t} - i\left(\frac{\partial}{\partial t}\Delta(t) \right) + \frac{\Omega^2}{4} \right) \tilde{c}_e &= 0. \end{aligned} \quad (3.7)$$

We transform into the following rotating frame: $c'_g = c_g \exp\left(\frac{i}{2}\int_0^t \Delta(t')dt'\right)$, $c'_e = \tilde{c}_e \exp\left(\frac{i}{2}\int_0^t \Delta(t')dt'\right)$. We also use a linear sweep $\Delta(t) = \alpha t$, where α is the sweep rate. We now have the following differential equations:

$$\begin{aligned} \left(\frac{\partial^2}{\partial t^2} + \frac{\Omega^2}{4} + \frac{i\alpha}{2} + \frac{t^2}{4} \right) c'_g &= 0 \\ \left(\frac{\partial^2}{\partial t^2} + \frac{\Omega^2}{4} - \frac{i\alpha}{2} + \frac{t^2}{4} \right) c'_e &= 0. \end{aligned} \quad (3.8)$$

If we do a change of variables: $\nu = \frac{i\Omega^2}{4\alpha}$, $z = e^{-i\pi/4}\sqrt{\alpha t}$, we end up with the following differential equations:

$$\begin{aligned} \left(\frac{\partial^2}{\partial z^2} + (\nu - 1) + \frac{1}{2} - \frac{t^2}{4} \right) c'_g &= 0 \\ \left(\frac{\partial^2}{\partial z^2} + \nu + \frac{1}{2} - \frac{t^2}{4} \right) c'_e &= 0. \end{aligned} \quad (3.9)$$

These are in the form of Weber's Equation, which can be solved analytically [39, 40]. The main way of solving these differential equations is by a lot of unintuitive substitution and difficult calculus [41]. Alternatively, the part of the solution we are interested in can be more easily found using Contour integrals as shown in reference [42]. The result is the probability that we successfully transfer population from the ground to the excited state:

$$P_{LZ} = e^{-\pi^2\Omega^2/|\dot{\Delta}|}. \quad (3.10)$$

This is called the Landau-Zener probability, and it only describes the errors from how quickly the transfer was performed, or, how adiabatic the passage was.

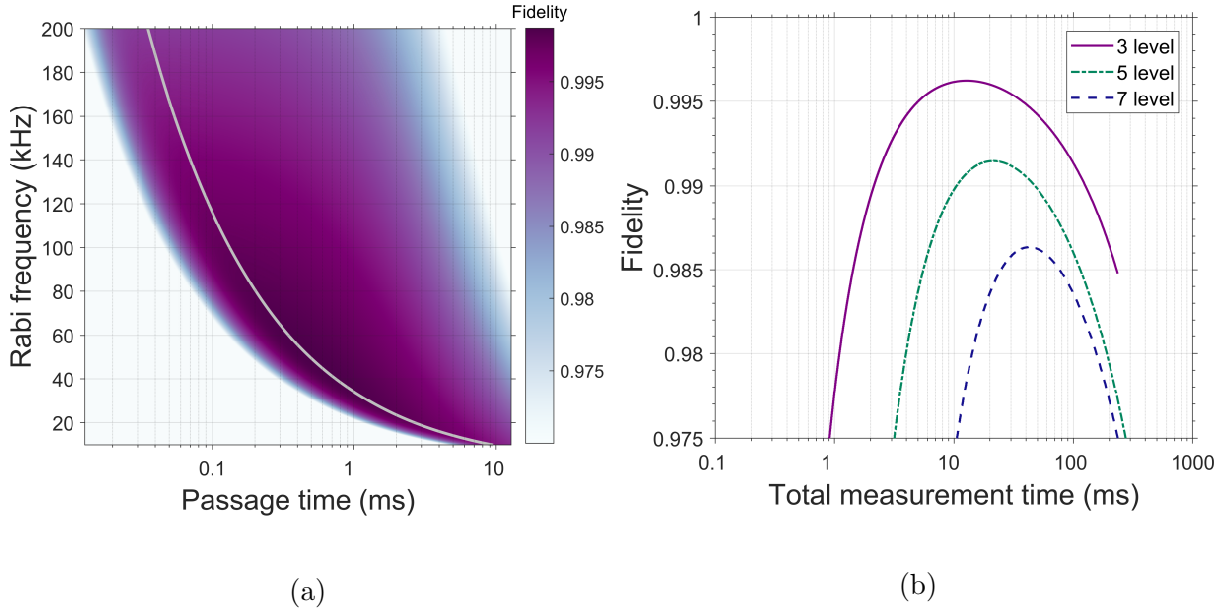


Figure 3.4: Shelving adiabatic passage and measurement error: (a) Equation 3.11 plotted for various applied Rabi frequencies and passage times $t = \frac{2\Delta}{\alpha}$. The horizontal axis is a log-scale. The grey line gives the optimal parameters. (b) The passage time and fidelity for different prime-dimensional qudits. Fluorescence time is included in the passage time, and we assume that the amount of adiabatic passages needed is $2d - 3$ (the maximum amount of transfers we would need to do for an arbitrary measurement).

There are several additional sources for error. The overall fidelity is given by

$$F = (1 - \sin^2 \theta)^2 \left(1 - \sum_i C_i^2 \frac{\Omega}{2\tilde{\Omega}'_i} \right)^2 \left(1/2 + e^{-2\pi^3 \Delta\nu\Omega/\alpha} (P_{LZ} - 1/2) \right) e^{-t/t_{dec}}, \quad (3.11)$$

where i is the set of all unwanted transitions each transfer can couple to at the start end end of the adiabatic passage, C_i is the relative branching ratio of an unwanted transition compared to the desired transition branching ratio, $\tilde{\Omega}' = \sqrt{\Delta'_i{}^2 + \Omega^2}$ is the effective Rabi-Frequency of the laser coupling with one of the other transitions, and $\Delta\nu$ is the FWHM laser linewidth.

The first term comes from imperfect adiabatic state preparation. For a constant Rabi frequency, we would have to start the frequency sweep at detuning $\Delta = \pm\infty$ to achieve one of the adiabatic states perfectly. This is obviously unrealistic, mostly because we have a plethora of other transition frequencies surrounding the desired transition. This can be seen from Equations 3.2 and 3.3: with a finite detuning Δ , the diabatic states do not correspond perfectly to either of the adiabatic states.

The second term comes from coupling to all of the other transitions colored red in Table 3.1. We model these contributions to the error as off-resonant Rabi flopping at detuning Δ'_i . The excited state population of this off-resonant coupling is in general $P_e = \frac{\Omega}{\tilde{\Omega}'} \sin^2 \Omega t/2$. We assume a time average $\sin^2 xt \approx 1/2$. Finally, we must multiply this population by the overall branching ratio C_i squared of the transition compared to the desired transition. These branching ratios are listed in Table 2.6.

The third term is the dephasing and transfer-time error, derived in reference [43], and it includes the Landau-Zener adiabaticity error. Lastly, we have to consider decay of the shelving state from its finite lifetime (~ 30 s for Ba^+).

For our experiment, we park our quantization magnetic field at $470 \mu\text{T}$. We transfer $|S_{1/2}; F, m_F\rangle$ states to $|D_{5/2}; F' = F, m'_F = m_F\rangle$ states in the shelving manifold. $m_F \leftrightarrow m'_F$ transitions are, in the smallest case, ≈ 3.9 MHz apart in frequency.

There are additional motional sidebands on this transition at the secular trap frequency. In a proposed blade trap, we expect this frequency to be $\omega_s \approx 2$ MHz. In this case, for some shelving transitions, the second motional sideband is less than 1 MHz away from the transitions we wish to drive. The Lamb-Dicke parameter for the $6S_{1/2} \leftrightarrow 5D_{5/2}$ transition is $\eta = k\sqrt{\frac{\hbar}{2m\omega_s}} = \frac{2\pi}{\lambda}\sqrt{\frac{\hbar}{2m\omega_s}} \approx 0.0243 \ll 1$. Because the Lamb-Dicke parameter is so small, the second (and higher) order sideband coupling will be negligible, and we ignore them.

To avoid sweeping through a first order sideband, we set the initial detuning at 1.6 MHz, which is 200 kHz below the tilt mode frequency. We sweep across the level and ending with equal but opposite detuning. Our laser will have a linewidth of less than 1 Hz [44]; we use this for the following calculations.

With these properties, we calculated the fidelity of population transfer for different Rabi frequency and overall passage time for the transition with the closest adjacent level

in Figure 3.4(a). There is a trade-off between the two variables and fidelity. As long as we can provide a Rabi frequency of greater than 110kHz, we can perform this passage in under 1 ms with better than 99.94% fidelity.

For our overall measurement process, we also have to consider each fluorescence measurement. The time for each fluorescence is given by

$$t_{fluorescence} \approx \frac{N_{photons}}{\gamma_{Detection}} = \frac{N_{photons}}{f_{fluorescence} CE \cdot QE}, \quad (3.12)$$

where $N_{photons}$ is the number of photons needed to discriminate between a positive or negative reading, $f_{fluorescence}$ is the frequency we drive our fluorescence transition at, CE is the collection efficiency of our imaging system, and QE is the quantum efficiency of our camera or PMT. We assume that our imaging system has $NA = 0.5$ and a quantum efficiency of 80%. A good estimate for our fluorescence rate is $f_{fluorescence} \approx \frac{1}{2\pi T_{P12}} \times 1/4 \approx 5$ MHz, where $T_{P12} = 7.92$ ns is the lifetime of the $6P_{1/2}$ state. Assuming we need around 10 bright-state photons to discriminate between a bright or dark reading, each fluorescence step takes $\sim 37 \mu s$.

Figure 3.4(b) considers the entire shelving measurement process for different qudits up to 7-levels. During a measurement, we can stop once fluorescence has been seen, so we usually don't have to do all of the transfers described in the shelving procedure. Here we assume the worst case where we end up having to do all of the transfers (for d levels, this is $2d - 3$ transfers). As can be seen in the figure, it's possible to get better than 98.5% overall measurement fidelity for even 7-level qudits. Both the 3- and 5- level qudits can be measured with better than 99% fidelity. Furthermore, because we can measure all of the states in the ground manifold with little error, state tomography for 3- and 5-level qudits is straightforward using this shelving technique.

Harty [45] was able to discriminate between a qubit state in the $S_{1/2}$ and the $D_{5/2}$ states with fluorescence in $^{43}\text{Ca}^+$; their overall state preparation and measurement fidelity was better than 99.9%. An important distinction is that their transfer to the shelving state was not coherent like our proposed shelving operation. If we assume that their 99.9% error is mostly coming from the measurement, and that we see similar results, then our overall measurement error will increase by a factor of $(99.9\%)^n$, where n is the number of fluorescence measurements.

To improve the adiabatic state preparation, we could instead use chirped pulses, where both the Rabi frequency and detuning are swept. Starting with a Rabi frequency of zero and a large detuning will give us a near perfect correspondence between the diabatic states and one of the adiabatic states. This technique could give us better than 99% fidelities in a shorter measurement time [46]. Alternatively, we could focus on improving our magnetic field stabilization, laser frequency and intensity stabilization and do normal Rabi transfers for an even shorter measurement time. Finally, when we do statistical measurements, we can use an adaptive algorithm to do state fluorescence on the state that the qudit is most likely in, based on the previous measurements. Such an adaptive measurement would make

the number of adiabatic passages necessary approach $d - 1$, dramatically decreasing the measurement error.

Four-Rod Paul Trap Optics

Since our lab is relatively new, and I am a part of the first round of graduate students, there was a lot of optics infrastructure to be done. The main scope of my work for my first year in the program was to pick out opto-mechanics for laser paths, pick out active optical components such as AOMs(Acousto-Optic Modulators) and EOMs(Electro-Optic Modulators), test lasers and optics, and come up with a plan for how to put it all together on the optics table for trapping ions in a four-rod paul trap.

This chapter describes my work towards getting the lab set up for trapping ions. In the first section of this chapter, I discuss the overall plan for the lasers and optics. Next, I present a successful frequency-locking scheme using a wavemeter. Finally, I discuss a system for distributing and controlling rf for driving the optical modulators.

4.1 Lasers and Optics

4.1.1 Lasers

To trap and manipulate ions, you need many different lasers in the lab. First, we need to ionize the neutral atoms. Lasers at 553 nm and 405 nm are used for the two-step ionization procedure described in section 2.4. The 553 nm light is generated by an 1107 nm laser built by Time Base [47], while the 405 nm laser is a very broad linewidth laser pointer. These lasers have powers of ~ 5 mW(after frequency doubling) and ~ 100 mW respectively.

Other lasers are used to drive the various transitions shown in the energy structure of barium in Figure 2.1. The 493 nm transition is useful for Doppler cooling, optical pumping,

and fluorescence measurement of spin states. We split this laser into two paths: one for cooling and the other for pumping and fluorescence. A 650 nm laser is necessary for re-pumping from the $5D_{3/2}$ state, since the probability of decaying to this state from the $6P_{1/2}$ state is around 24% [24]. Both of these lasers are from Toptica [48], and provide around 10-20 mW and 15-25 mW of power, respectively, depending on how well we can couple them. We found the Toptica fiberdock used to couple them to be unreliable at times: every couple of months, we have to re-align to the fiber, because the output suddenly dropped to under 1 mW. We use a 1228 nm laser frequency-doubled to 650 nm to de-populate the $5D_{5/2}$ level. This laser, like the 1107 nm laser, was obtained from Time Base [47]. After frequency doubling, this laser has ~ 1 mW output power.

Finally, we will use a 1762 nm laser built by Toptica [48] and stabilized by Stable Laser Systems [44] to perform our shelving measurement as described in chapter 3. This laser will be stabilized to a linewidth of ~ 1 Hz, with a power of around 30 mW. One big advantage with our necessary lasers is the fact that none of them are in the UV range, therefore it's possible to do much of the optics manipulation with fiber devices. This is a distinct advantage to using barium over other ions.

4.1.2 Optics Paths

There are a number of components which need to be placed in the path between the lasers and the ions in order to gain control of different aspects of the light. To generate 553 nm and 650 nm light, we must use a frequency-doubler immediately after a 1107 nm and 1228 nm laser respectively. Each laser's output needs to be picked off for monitoring its wavelength. Most lasers need to be frequency modulated using an EOM. For lasers which need fast switching off/on, we have to place an AOM in the path. We need various waveplates to control the polarization of each beam. We need to pick off part of the light just before the trap to measure its intensity. Finally, we must focus each beam down to a single point where the ion is using a lens or concave mirror.

The details of all of the components we need for each laser are illustrated in Figure 4.1. There are three levels of control necessary for different lasers: the 405 nm ionization needs very little control, and simply needs to be turned on and guided to the trap. The 553 nm ionization laser needs some basic frequency control. All other lasers need full control of frequency, switching, polarization, and amplitude.

Following the optical paths in Figure 4.1, the first component is the frequency doubler for the 1107 nm and 1228 nm lasers. This component doubles the frequencies of these lasers to 553 nm and 650 nm respectively. Since these lasers are fiber coupled, we use HC Photonics fiber frequency-doublers. With 80 mW of 1107 nm input power, we get around 5 mW of output 553 nm power: around 5% conversion. For 1228 nm, with 34 mW of input power, we get around 1 mW of output 650 nm power: around 3% conversion.

We use Thorlabs 99:1 PM fiber splitters [49] to pick off 1% of most paths, for measuring the wavelength.

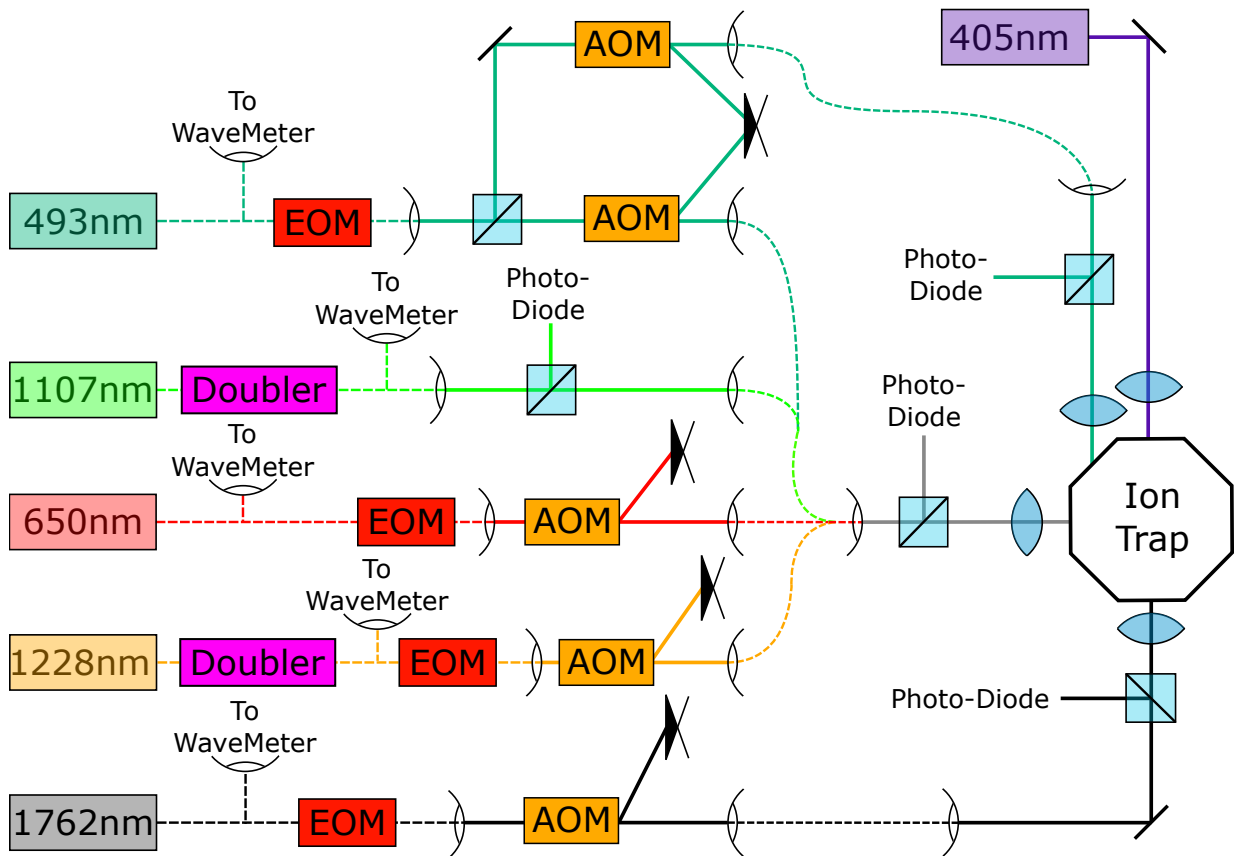


Figure 4.1: Overall beam paths: each eyeball shape is a fiber coupler or collimator, and each solid black object is a beam block. Dotted lines are fiber cables and solid lines are free laser beams.

Since $^{137}\text{Ba}^+$ has hyperfine structure, each level is split into many different F hyperfine levels. In order to drive all F levels, we need to use an EOM to impose sidebands on the lasers. For the ground state $6S_{1/2}$, this hyperfine splitting is on the order of 8 GHz, which is relevant for 493 nm and 1762 nm transitions. For the 493 nm laser, we decided to use an ADVR [50] fiber-coupled EOM, which has an insertion loss of around 6.5 dB. With 20 dBm of rf power, the power of the first sideband is around 36% of the carrier power. The 1762 nm laser hasn't arrived yet, but we will use an EOSpace [51] EOM with an expected insertion loss of 3 dB. For the 650 nm and 650 nm transitions, we need to generate sidebands on the order of 1 GHz; we went with Jenoptik [52] fiber-coupled EOMs for both of these. The insertion loss is around 6 dB, and with around 15 dBm of rf power, we can get around 50% power in the first sideband.

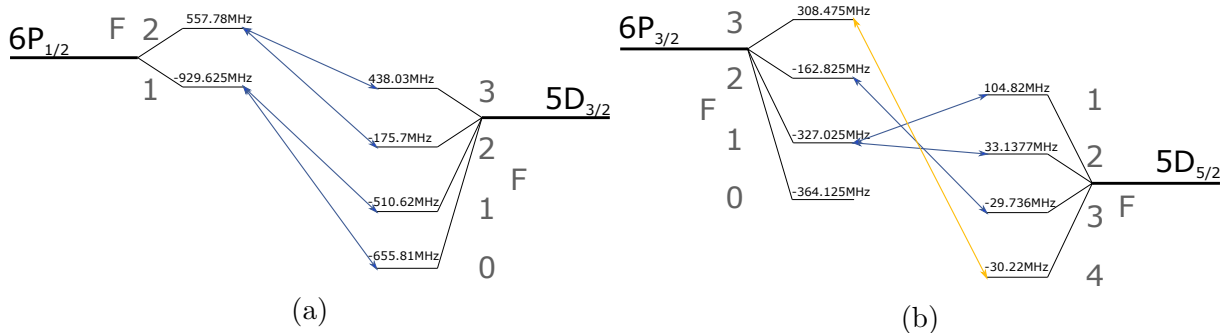


Figure 4.2: EOM transition frequencies: transitions driven with (a) $5D_{3/2} \leftrightarrow 6P_{1/2}$ and (b) $5D_{5/2} \leftrightarrow 6P_{3/2}$ lasers. Blue transitions are always driven. Orange transitions are usually not necessary because the lower state is not likely to be populated.

To gain additional frequency control as well as the ability to switch the beams on/off more quickly, we use AOMs in most beam paths. AOMs don't generate sidebands like EOMs, rather, they offset the frequency by some fixed amount. Typically, an AOM can convert around 60 – 80% of the input intensity into a diffracted output. The frequency offset gives us fine control of the overall frequency of the light, and the diffraction allows us to quickly turn the path on/off by simply turning off the rf power to the AOM. This switching speed is limited by either the TTL (Transistor-Transistor Logic) signal or how the speed of sound in the nonlinear crystal within the AOM device - either of which is much faster than any physical shutter. Since the 405 nm and 553 nm timing requirements are much less critical, we use physical shutters [53] to switch these beams on/off.

We combine the cooling 493 nm, de-populating 650 nm, re-pumping 650 nm, and ionization 553 nm beams into one optical fiber using a wavelength division multiplexor. This allows us to align all of these beams together, simplifying the alignment procedure. It also reduces the amount of optics needed for these beams around the trap, giving us extra space to work with or expand the experiment with more optics.

Finally, we use a beamsplitter to pick off part of each beam for measuring the intensity just before the trap. Eventually this measurement will be used to feedback to the lasers

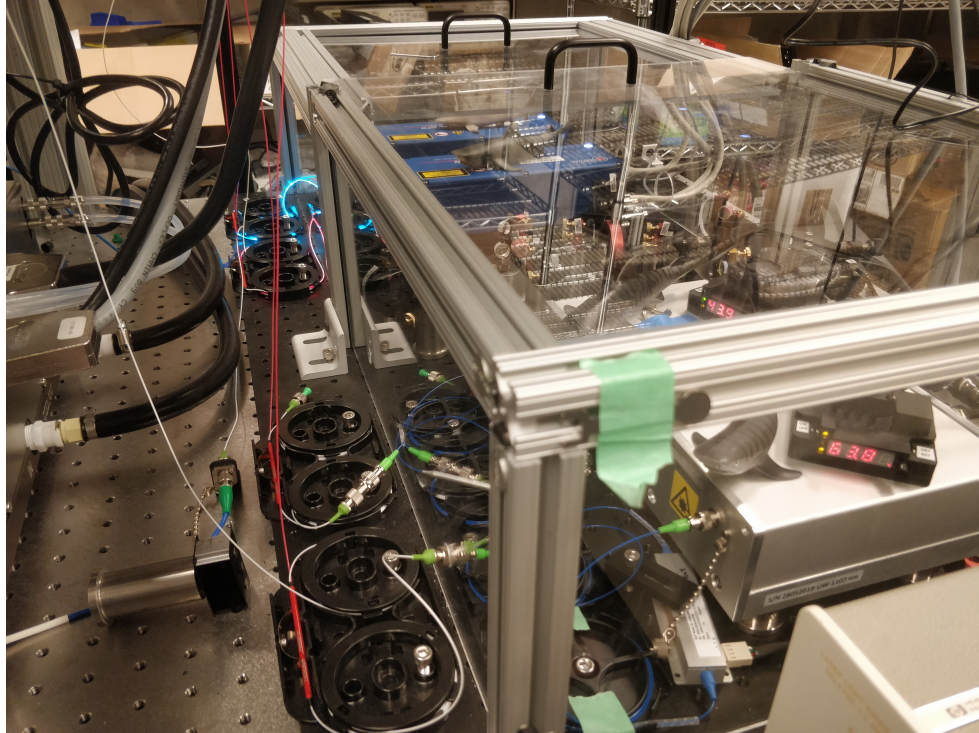


Figure 4.3: Lasers enclosure: having sharks on top of each laser helps.

for intensity stabilization.

To shield the lasers from temperature and humidity fluctuations, a lasers enclosure, shown in Figure 4.3, was designed and built. This enclosure currently houses the 493 nm, 650 nm, 1107 nm, and 1228 nm lasers. For free optics paths, we designed and built enclosures for each laser. These modular enclosures are portable (on aluminum breadboards), and have many other advantages. With enclosures, there's less risk of optical injury from stray lasers, and the optics is less prone to shifting from temperature and humidity fluctuations. Furthermore, the optics doesn't need to be cleaned as often. Finally, you can easily move the enclosure elsewhere if you want to work on a particular path in a more convenient location. Optics paths for the 493 nm, 650 nm, and ionization lasers within the enclosures are shown in Figures 4.5 and 4.6. The 650 nm and 1762 nm paths are almost identical to the 650 nm path. A picture of the 493 nm optics enclosure is shown in Figure 4.4.

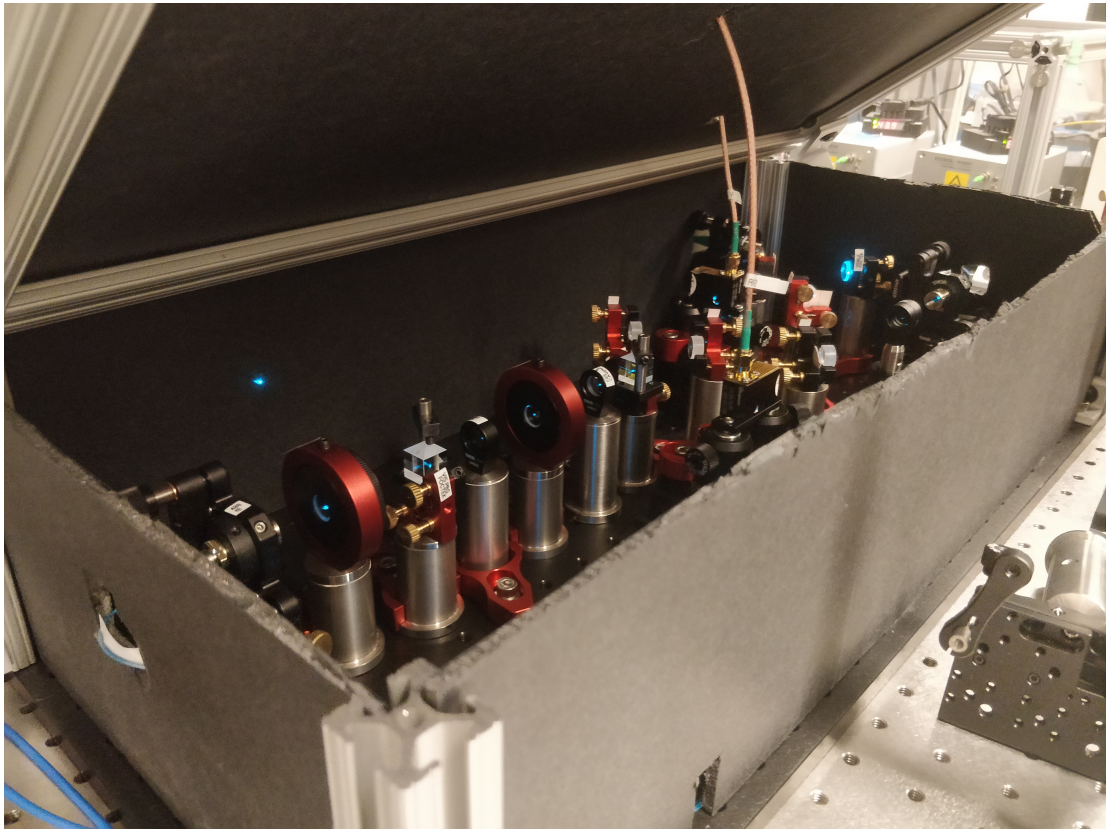


Figure 4.4: 493 nm optics enclosure

4.2 Frequency Locking

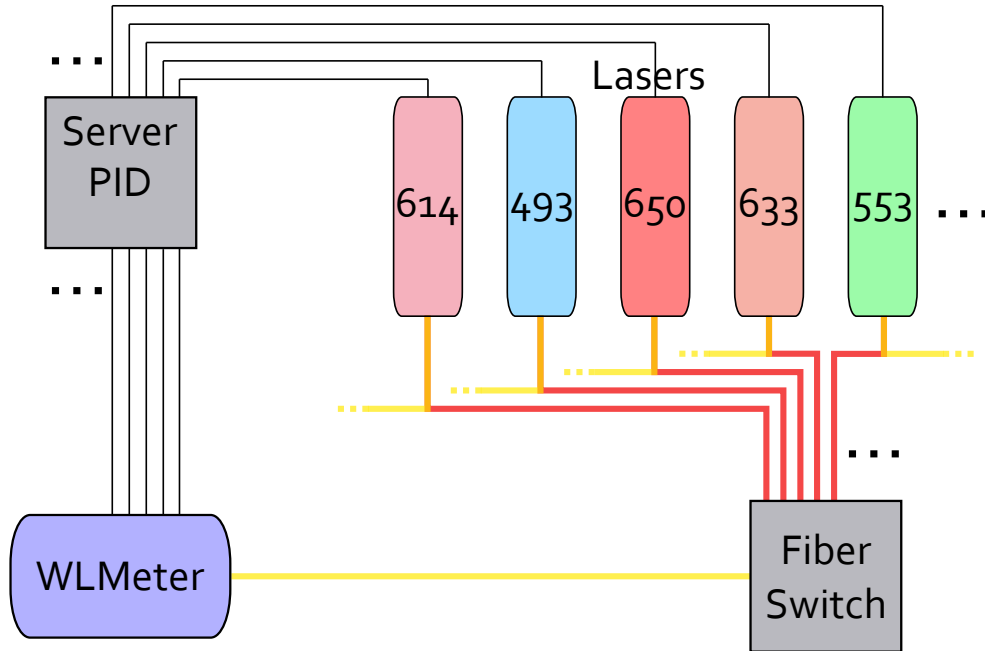


Figure 4.7: Frequency locking setup: a wavemeter reads the wavelength of various lasers through a fiber switch, and outputs an error signal. A PID generates feedback for the lasers via grating piezo voltage, allowing us to lock lasers to a arbitrary frequency profiles.

For reading the wavelengths of our lasers, we use the HighFinesse Wavelength Meter WS-8-30 [54]. This wavelength meter uses Fizeau interferometers to measure an interference pattern; the software included displays the interferometer outputs and also analyzes them to output a wavelength or frequency with an absolute accuracy of 60 MHz and a precision of 1 MHz. Using an optical switch, we can monitor up to 8 different continuous wave channels. This wavelength meter only works from 330nm up to 1180nm, so we will get another wavelength meter for measuring the 1762 nm laser.

With the additional regulation upgrade, the software can use a PID to regulate all of the lasers to any arbitrary function. For the toptica lasers, piezo amplifiers are included in the controller. For the Time-Base lasers, we use a PiezoDrive [55] 6-channel amplifier, which has a gain of $25V/V$ and maximum output of $\pm 250V$. This entire process is illustrated in Figure 4.7. We use 99:1 fiber splitters to pick off 1% for measuring with the wavelength meter. The wavelength meter software reads the wavelength and uses a PID to generate feedback, which we amplify and use to modulate the piezo of each laser cavity, thereby changing the cavity length and output wavelength.

The optimal PID settings for the 493 nm, 553 nm, and 650 nm lasers are shown in Table 4.1. For the Toptica lasers, the PID works like a dream; however, the 553 nm has some issues. Sometimes, the laser will mode-hop while being regulated with the PID. This

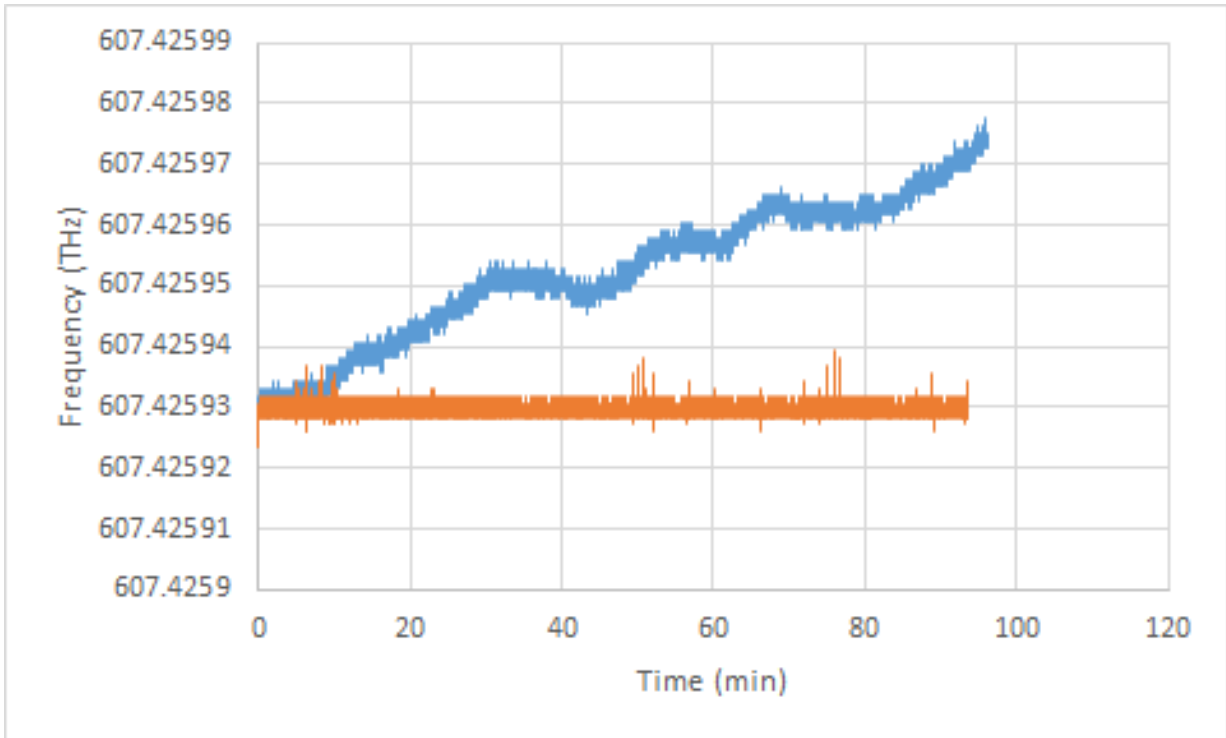


Figure 4.8: Wavelength meter frequency locking: Measuring the 493nm laser - the orange signal is locked, and the blue signal is unlocked.

wouldn't be an issue, as the PID is meant to turn off when this sort of a thing happens. However, sometimes this causes the polarity to change creating a positive feedback loop, exasperating the issue and pushing the laser far from the previous frequency. When this happens, we must manually adjust the piezo position with a hex key to re-tune the laser to near the locking frequency. Then, we must relax the PID parameters and turn on regulation to find the correct polarity. Once we've set the polarity correctly, we can slowly ramp back up to the original PID settings and hopefully resume experiments with a well-behaved laser.

Laser	Gain (V/V)	PID Sensitivity	P	I	D	Constant dt?	Use ta?
493 nm	1	-1 V/pm	0.5	8.0	0	no	1.0 s
553 nm	25	1 V/100GHz	4.0	8.0	0	1.0 s	no
650 nm	1.4286	-1 V/pm	0.65	2.01	0	no	no

Table 4.1: Wavelength meter PID settings: these are the current optimal parameters for the wavelength meter lock.

Figure 4.8 shows data from frequency locking our 493 nm, 553 nm, and 650 nm lasers using this technique.

4.3 RF sources

In order to drive the EOMs and AOMs, we need frequency sources which can be frequency tuned and amplitude tuned. We chose to build a system of phase-locked loop(PLL) Evaluation Boards and attenuator evaluation boards for their low cost. ADF-41020 [56] PLLs provide microwave frequencies of around 8 GHz for the 493 nm and 1762 nm laser EOMs, while ADF-4355-2 [57] PLLs provide rf frequencies between 100 MHz and 2000 MHz for all AOMs as well as the 614 nm and 650 nm laser EOMs. With the ADF-41020, the default VCO (Voltage Controlled Oscillator), the HMC515, isn't compatible with the 8 GHz we need it to produce. So with this Evaluation Board, we must replace the VCO chip with an HCM509.

The EVB-EK4312 [58] attenuator boards allow us to reduce the rf power from the ADF-4355-2 boards. This can be important to make sure we don't exceed an AOM or EOM's power handling, or to reduce the overall diffraction efficiency of an AOM, thereby changing the output optical power. However, they don't work for frequencies as high as 8 GHz. For these microwave synthesizers, we must manually insert fixed attenuators in the line as desired due to a lack of suitable attenuator Evaluation Boards for these higher frequencies.

To combine many different frequency signals into one wire, we designed RF combiner boards. These are used for transitions such as the repumping $5D_{3/2} \leftrightarrow 6P_{1/2}$ transition and the de-populating $5D_{5/2} \leftrightarrow 6P_{3/2}$ transition, where there are more than 2 hyperfine levels. The details of which frequencies are combined together on each line are given in Figure 4.2. The PLL oscillators and attenuators are controlled via a Raspberry Pi 3 control board [59]. They are controlled through a serial peripheral interface (SPI) bus along with individual general-purpose I/O (GPIO) pins for Latch Enable.

The final drive to the appropriate AOM or EOM is provided by four types of Mini-Circuits and RF-Bay amplifiers. The MPA-11-40 and MPA-40-40 amplifiers [60, 61] are used for rf in the range 1-1000 MHz, the ZHL4240 amplifier [62] is used for rf between 10-4200 MHz, and the ZVE-3W-183+ amplifier [63] drives microwave signals between 5.9-18 GHz. The MPA-11-40 and MPA-40-40 are used for AOMs and lower frequency EOMs, and can amplify up to 4 W and 1 W respectively; typically, the higher wavelength AOMs require more power, so we use the MPA-11-40 for these. The ZHL4240 is used for medium frequency EOMs, and the ZVE-3W-183+ is used for high frequency EOMs.

For switching lines on and off, we use the ZX80-DR230+ [64] Mini-Circuits rf switch. For flexibility of switching, we built a front panel with triple pole double throw switches, so we can use either BNC TTL input or manual switching. Again, there were no suitable switches for the microwave lines, so we must directly turn these PLLs off.

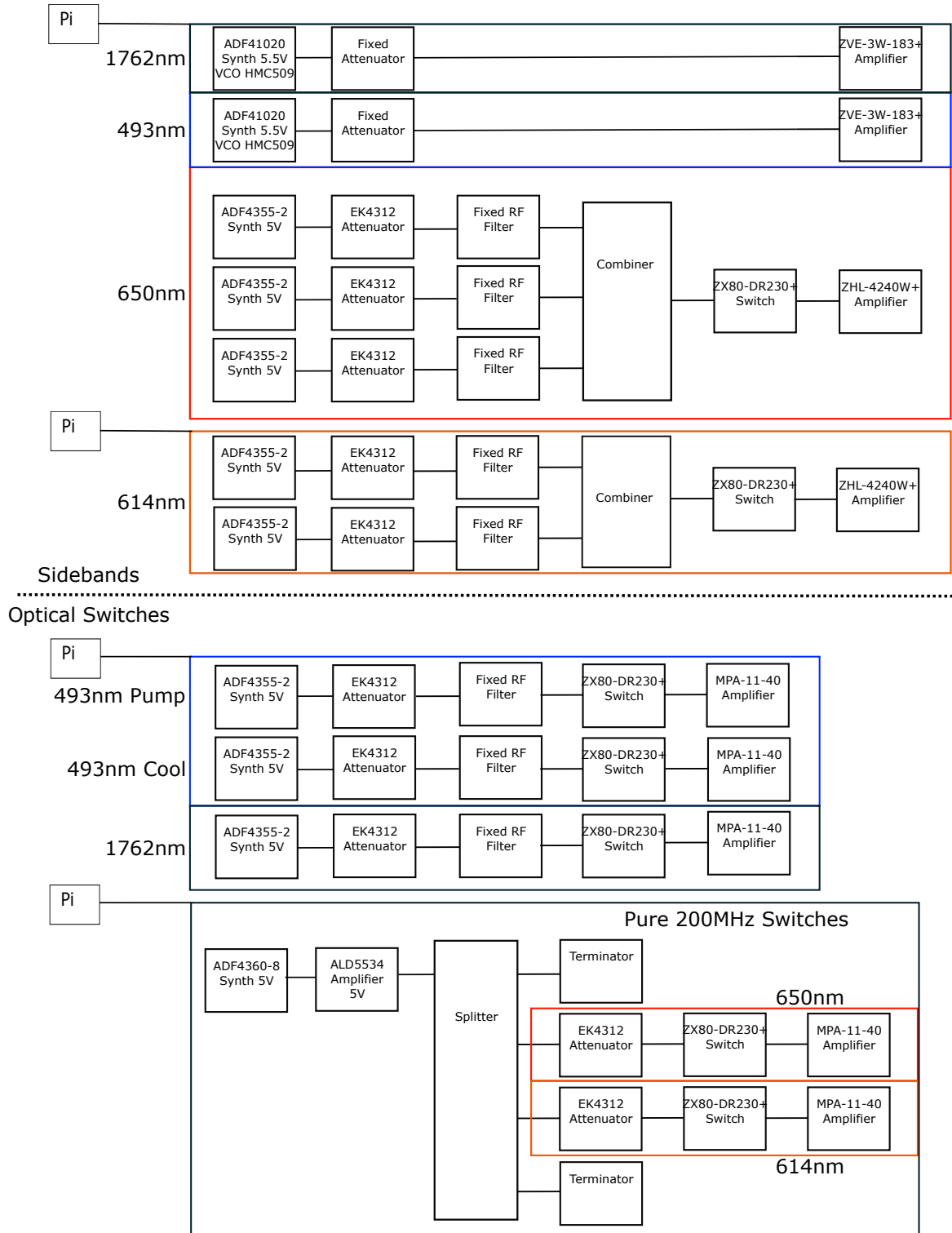


Figure 4.9: Frequency sources: a Raspberry Pi computer controls PLLs and attenuators which generate rf for EOMs and AOMs for the various optics paths.

Conclusion

In this thesis, I have introduced our lab's plan for improving the scalability of trapped ion quantum information - utilizing more than two levels to form qudits. I have laid out much of the basic atomic physics necessary for working with our chosen ion - $^{137}\text{Ba}^+$ - including energy structure for an applied magnetic field, transition strengths, and saturation intensity. Information on the energy levels and how they are affected by magnetic fields are shown in Figures 2.3, 2.4, and 2.5. All of the transition strengths derived in section 2.2 have been calculated and tabulated in Tables A.1 through A.24 in the appendix. I also have discussed how we can utilize the isotope shift to be able to pick between trapping different isotopes of barium. In chapter 3, I have described a scheme for measuring out all of the different states of our qudits in $^{137}\text{Ba}^+$ and discussed different error mechanisms that come into play. The overall measurement error for 3- and 5-level qudits was estimated to be less than 1%. In the final chapter, I have presented many of the optics projects I completed in order to actually trap barium in our group's first four-rod Paul trap, including optics design and planning, frequency locking, and rf source design.

Our lab has just started actually trapping ions in our four-rod trap (see figure 5.1), so there is a lot of work to be done immediately. Now that we have ions to work with, we need to test many of the barium characterization I presented in chapter 2. One of our goals is to prove out the isotope selectivity, so that we can choose what flavor of barium to work with in situ. While we wait for our shelving laser to arrive, a frequency mixer needs to be devised for performing the frequency modulation necessary for the qudit measurement procedure. After it arrives and we have the means to do population transfers to the shelving state using adiabatic passage, we can test out the measurement scheme. Of course once we can reliably trap and measure qudits, we can begin to actually characterize and use them for exploring qudit quantum information.

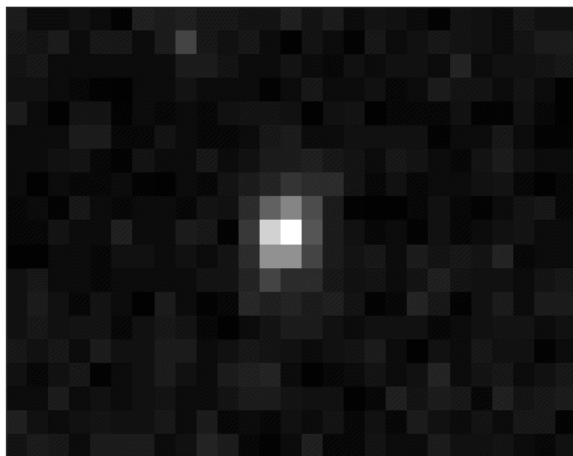


Figure 5.1: We were able to trap $^{137}\text{Ba}^+$ with our four-rod trap! It took a lot of brainstorming and stabbing in the dark to overcome many challenges along the way, but we finally managed to trap ions! This is all thanks to the concerted effort of everybody in Senkolab - especially those that helped with the bring-up of the four-rod trap including Pei Jiang Low, Rich Rademacher, Noah Greenberg, and Matthew Day. Acknowledgement is also owed to Nigel Anderson and of course our PI Dr. Crystal Senko, who helped us in coming up with new directions when we inevitably found ourselves fumbling around in the dark.

References

- [1] A. P. Lund, M. J. Bremner, and T. C. Ralph. [Quantum sampling problems, Boson-Sampling and quantum supremacy](#). *Quantum Inf. Comput.*, 3, Apr 2017.
- [2] D. Kielpinski, C. Monroe, and D. J. Wineland. [Observation of a many-body dynamical phase transition with a 53-qubit quantum simulator](#). *Nature*, 551:601–604, November 2017.
- [3] G. Pagano, P. W. Hess, H. B. Kaplan, W. L. Tan, Richerme P., P. Becker, Kyprianidis A., J. Zhang, E. Birckelbaw, M. R. Hernandez, Y. Wu, and C. Monroe. Cryogenic trapped-ion system for large scale quantum simulation. *Quantum Science and Technology*, 4(1):014004, October 2018.
- [4] E. Knill and R. Laflamme. [Theory of quantum error-correcting codes](#). *Phys. Rev. A*, 55:900–911, Feb 1997.
- [5] R. Bowler, J. Gaebler, Y. Lin, T. R. Tan, D. Hanneke, J. D. Jost, J. P. Home, D. Leibfried, and D. J. Wineland. [Coherent Diabatic Ion Transport and Separation in a Multizone Trap Array](#). *Phys. Rev. Lett.*, 109:080502, Aug 2012.
- [6] T. Ruster, C. Warschburger, H. Kaufmann, C. T. Schmiegelow, A. Walther, M. Hettrich, A. Pfister, V. Kaushal, F. Schmidt-Kaler, and U. G. Poschinger. [Experimental realization of fast ion separation in segmented Paul traps](#). *Phys. Rev. A*, 90:033410, Sep 2014.
- [7] D. Kielpinski, C. Monroe, and D. J. Wineland. [Architecture for a large-scale ion-trap quantum computer](#). *Nature*, 417:709–711, June 2002.

- [8] C. Monroe, R. Raussendorf, A. Ruthven, K. R. Brown, P. Maunz, L.-M. Duan, and J. Kim. [Large-scale modular quantum-computer architecture with atomic memory and photonic interconnects](#). *Phys. Rev. A*, 89:022317, Feb 2014.
- [9] B. P. Lanyon, M. Barbieri, M. P. Almeida, T. Jennewein, T. C. Ralph, K. J. Resch, G. J. Pryde, J. L. O’Brien, A. Gilchrist, and A. G. White. [Simplifying quantum logic using higher-dimensional Hilbert spaces](#). *Nature Phys.*, 5:134–140, Dec 2008.
- [10] P. Gokhale, J. M. Baker, C. Duckering, N. C. Brown, K. R. Brown, and Chong F. T. [Asymptotic Improvements to Quantum Circuits via Qutrits](#). *Arxiv*, May 2019.
- [11] E. T. Campbell, H. Anwar, and D. E. Browne. [Magic-state distillation in all prime dimensions using quantum Reed-Muller codes](#). *Phys. Rev. X*, 2:041021, Dec 2012.
- [12] E. T. Campbell. [Enhanced fault-tolerant quantum computing in d-Level systems](#). *Phys. Rev. Lett.*, 113:230501, Dec 2014.
- [13] R. S. Andrist, J. R. Wootton, and H. G. Katzgraber. [Error thresholds for Abelian quantum double models: Increasing the bit-flip stability of topological quantum memory](#). *Phys. Rev. A*, 91:042331, Apr 2015.
- [14] J. D. Bjorken and S. D. Chuang. *Relativistic Quantum Mechanics*. McGraw-Hill, 1994. Section 8.7: The Lamb Shift.
- [15] G. K. Woodgate. *Elementary Atomic Structure*. Oxford Science Publications, 1980. Chapter 9: Hyperfine Structure and Isotope Shift.
- [16] J. J. Curry. [Compilation of wavelengths, energy levels, and transition probabilities for Ba I and Ba II](#). *J. Phys. Chem. Ref. Data*, 33(3):725–746, 2004.
- [17] R. Blatt and G. Werth. [Precision determination of the ground-state hyperfine splitting in \$^{137}\text{Ba}^+\$ using the ion-storage technique](#). *Phys. Rev. A*, 25:1476–1482, Mar 1982.
- [18] R. E. Silverans, G. Borghs, P. De Bisschop, and M. Van Hove. [Hyperfine structure of the \$5d\ ^2D_J\$ states in the alkaline-earth Ba ion by fast-ion-beam laser-rf spectroscopy](#). *Phys. Rev. A*, 33:2117–2120, Mar 1986.
- [19] P. Villemoes, A. Arnesen, F. Hejlskov, and A. Wannstrom. [Isotope shifts and hyperfine structure of \$^{134-138}\text{Ba II}\$ by fast ion beam-laser spectroscopy](#). *Journal of Physics B: Atomic, Molecular and Optical Physics*, 26(22):4289–4299, nov 1993.
- [20] D. Hucul, J. E. Christensen, E. R. Hudson, and W. C. Campbell. [Spectroscopy of a synthetic trapped ion qubit](#). *Phys. Rev. Lett.*, 119:100501, Sep 2017.
- [21] R. G. DeVoe and C. Kurtsiefer. [Experimental study of anomalous heating and trap instabilities in a microscopic \$^{137}\text{Ba}\$ ion trap](#). *Phys. Rev. A*, 65:063407, Jun 2002.

- [22] T. W. Koerber, M. H. Schacht, K. R. G. Hendrickson, W. Nagourney, and E. N. Fortson. [rf spectroscopy with a single Ba⁺ ion](#). *Phys. Rev. Lett.*, 88:143002, Mar 2002.
- [23] M. R. Dietrich, A. Avril, R. Bowler, N. Kurz, J. S. Salacka, G. Shu, and B. B. Blinov. [Barium ions for quantum computation](#). *AIP Conference Proceedings*, 1114(1):25–30, 2009.
- [24] M. D. Davidson, L.C. Snoek, H. Volten, and A. Doenzelmann. [Oscillator strengths and branching ratios of transitions between low-lying levels in the barium II spectrum](#). *Astron. Astrophys.*, 255:457–458, Feb 1992.
- [25] N. Kurz, M. R. Dietrich, Gang Shu, R. Bowler, J. Salacka, V. Mirgon, and B. B. Blinov. [Measurement of the branching ratio in the 6P_{3/2} decay of Ba II with a single trapped ion](#). *Phys. Rev. A*, 77:060501, Jun 2008.
- [26] C. Auchter, T. W. Noel, M. R. Hoffman, S. R. Williams, and B. B. Blinov. [Measurement of the branching fractions and lifetime of the 5D_{5/2} level of Ba⁺](#). *Phys. Rev. A*, 90:060501, Dec 2014.
- [27] D. A. Steck. *Quantum and Atom Optics*. None, 2007. Chapter 7: Atomic Angular-Momentum Structure.
- [28] D. F. V. James. [Quantum dynamics of cold trapped ions with application to quantum computation](#). *Appl. Phys. B*, 66(2):181–190, 1998.
- [29] C. Roos. [Controlling the quantum state of trapped ions](#). PhD thesis, University of Innsbruck, 2000.
- [30] H. J. Metcalf and P. van der Straten. *Laser Cooling and Trapping*. Springer, 1999. Chapter 2: The Density Matrix.
- [31] Post B. H., Vassen W., Hogervorst W., Aymar M., and Robaux O. [Odd-parity Rydberg levels in neutral barium: term values and multichannel quantum defect theory analysis](#). *J. Phys. B*, 18(2):187–206, jan 1985.
- [32] P. E. G. Baird, R. J. Brambley, K. Burnett, D. N. Stacey, D. M. Warrington, G. K. Woodgate, and H. G. Kuhn. [Optical isotope shifts and hyperfine structure in \$\lambda 553.5\text{nm}\$ of barium](#). *Proc. R. Soc. London, Ser. A*, 365(1723), 1979.
- [33] C. Nazé, J. G. Li, and M. Godefroid. [Theoretical isotope shifts in neutral barium](#). *Phys. Rev. A*, 91:032511, Mar 2015.
- [34] K. Bekk, A. Andl, S. Göring, A. Hanser, G. Nowicki, H. Rebel, and G. Schatz. [Laser-spectroscopic studies of collective properties of neutron deficient Ba Nuclei](#). *Z. Phys. A*, 291(3):219–230, Sep 1979.

- [35] W. A. van Wijngaarden and J. Li. [Hyperfine splittings and isotope shifts of \$\(6s\)21S0 \rightarrow \(6s6p\)1P1\$ transition in barium.](#) *Can. J. Phys.*, 73(7-8):484–488, 1995.
- [36] P. Low, B. M. White, A. A. Cox, M. L. Day, and C. Senko. [Practical trapped-ion protocols for universal qudit-based quantum computing.](#) *Arxiv*, July 2019.
- [37] T. Noel, M. R. Dietrich, N. Kurz, G. Shu, J. Wright, and B. B. Blinov. [Adiabatic passage in the presence of noise.](#) *Phys. Rev. A*, 85:023401, Feb 2012.
- [38] N. V. Vitanov, T. Halfmann, B. W. Shore, and K. Bergmann. [Laser-induced population transfer by adiabatic passage techniques.](#) *Ann. Rev. Phys. Chem.*, 52(1):763–809, 2001.
- [39] C. Zener. [Non-adiabatic crossing of energy levels.](#) *Proc. Royal Soc. A*, 137(833):696–702, 1932.
- [40] L. D. Landau. A theory of energy transfer II. *Phys. Z. Sowjetunion*, 2(46), 1932.
- [41] E. T. Whittaker and G. N. Watson. *A Course of Modern Analysis*. Cambridge University Press, 1927. Section 16.5: The Parabolic Cylinder Functions. Weber’s Equation.
- [42] C. Wittig. [The Landau-Zener Formula.](#) *J. Phys. Chem. B*, 109(17):8428–8430, 2005. PMID: 16851989.
- [43] X. Lacour, S. Guérin, L. P. Yatsenko, N. V. Vitanov, and H. R. Jauslin. [Uniform analytic description of dephasing effects in two-state transitions.](#) *Phys. Rev. A*, 75:033417, Mar 2007.
- [44] Stable laser systems. <http://www.stablelasers.com/>, 2019.
- [45] T. P. Harty, D. T. C. Allcock, C. J. Ballance, L. Guidoni, H. A. Janacek, N. M. Linke, D. N. Stacey, and D. M. Lucas. [High-fidelity preparation, gates, memory, and readout of a trapped-ion quantum bit.](#) *Phys. Rev. Lett.*, 113:220501, Nov 2014.
- [46] C. Wunderlich, T. Hannemann, T. Körber, H. Häffner, C. Roos, W. Hänsel, R. Blatt, and F. Schmidt-Kaler. [Robust state preparation of a single trapped ion by adiabatic passage.](#) *J. Mod. Opt.*, 54(11):1541–1549, 2007.
- [47] Time base. <http://www.time-base.de/images/Manuals/ECQDL/Specs-ECQDL.pdf>, 2019.
- [48] Toptica. <https://www.toptica.com/products/tunable-diode-lasers/ecdl-dfb-lasers/dl-pro/>, 2019.
- [49] Thorlabs. https://www.thorlabs.com/navigation.cfm?guide_id=2211, 2019.
- [50] Advr. <http://www.advr-inc.com/ktpmodulators/>, 2019.

- [51] Eospace. <https://www.eospace.com/phase-modulator>, 2019.
- [52] Jenoptik. <https://www.jenoptik.com/products/optoelectronic-systems/light-modulation/integrated-optical-modulators-fiber-coupled>, 2019.
- [53] Thorlabs. https://www.thorlabs.com/NewGroupPage9.cfm?ObjectGroup_ID=927, 2019.
- [54] Highfinesse. <https://www.highfinesse.com/en/wavelengthmeter/wavelengthmeter-ws-8-30.html>, 2019.
- [55] Piezodrive. <https://www.piezodrive.com/drivers/td250-six-channel-250v-amplifier-for-driving-piezo-tubes/>, 2019.
- [56] Adf-41020. <https://www.analog.com/en/products/adf41020.html>, 2019.
- [57] Adf-4355. <https://www.analog.com/en/products/adf4355.html>, 2019.
- [58] Pe4312. <https://www.psemi.com/products/digital-step-attenuators-dsa/pe4312>, 2019.
- [59] Raspberry pi 3. <https://www.raspberrypi.org/products/raspberry-pi-3-model-b/>, 2019.
- [60] Mpa-11-40. http://rfbayinc.com/product_info.php?cPath=55&products_id=670, 2019.
- [61] Mpa-40-40. http://rfbayinc.com/product_info.php?cPath=55&products_id=186, 2019.
- [62] Zhl-4240. <https://www.minicircuits.com/WebStore/dashboard.html?model=ZHL-4240%2B>, 2019.
- [63] Zve-3w-183+. <https://www.minicircuits.com/WebStore/dashboard.html?model=ZVE-3W-183%2B>, 2019.
- [64] Zx80-dr230+. <https://www.minicircuits.com/WebStore/dashboard.html?model=ZX80-DR230-S%2B>, 2019.

APPENDIX A

Appendix

A.1 Dipole Transition Branching Ratios/Strengths

$6S_{1/2} \leftrightarrow 6P_{1/2}, q = +1$	
$F = 0 \leftrightarrow F' = 0$	
None	
$F = 0 \leftrightarrow F' = 1$	
m_F	0
$m_{F'}$	-1
-0.5774	
$F = 1 \leftrightarrow F' = 0$	
1	
0	
0.5774	
$F = 1 \leftrightarrow F' = 1$	
0	1
-1	0
-0.5774	-0.5774

$6S_{1/2} \leftrightarrow 6P_{1/2}, q = -1$	
$F = 0 \leftrightarrow F' = 0$	
None	
$F = 0 \leftrightarrow F' = 1$	
m_F	0
$m_{F'}$	1
-0.5774	
$F = 1 \leftrightarrow F' = 0$	
-1	
0	
0.5774	
$F = 1 \leftrightarrow F' = 1$	
-1	0
0	1
0.5774	0.5774

Table A.1: $^{133}\text{Ba}^+$ dipole branching ratios: $6S_{1/2} \leftrightarrow 6P_{1/2}, q = +1$

Table A.2: $^{133}\text{Ba}^+$ dipole branching ratios: $6S_{1/2} \leftrightarrow 6P_{1/2}, q = -1$

$6S_{1/2} \leftrightarrow 6P_{1/2}, q = 0$	
$F = 0 \leftrightarrow F' = 0$	
Forbidden	
$F = 0 \leftrightarrow F' = 1$	
m_F	0
$m_{F'}$	0
0.5774	
$F = 1 \leftrightarrow F' = 0$	
0	
0	
0.5774	
$F = 1 \leftrightarrow F' = 1$	
-1	0
-1	0
-0.5774	0

Table A.3: $^{133}\text{Ba}^+$ dipole branching ratios: $6S_{1/2} \leftrightarrow 6P_{1/2}, q = 0$

$6S_{1/2} \leftrightarrow 6P_{3/2}, q = +1$		
$F = 0 \leftrightarrow F' = 1$		
m_F	0	
$m_{F'}$	-1	
0.5774		
$F = 0 \leftrightarrow F' = 2$		
Forbidden		
$F = 1 \leftrightarrow F' = 1$		
0	1	
-1	0	
-0.2887	-0.2887	
$F = 1 \leftrightarrow F' = 2$		
-1	0	1
-2	-1	0
0.7071	0.5000	0.2887

$6S_{1/2} \leftrightarrow 6P_{3/2}, q = -1$		
$F = 0 \leftrightarrow F' = 1$		
m_F	0	
$m_{F'}$	1	
0.5774		
$F = 0 \leftrightarrow F' = 2$		
Forbidden		
$F = 1 \leftrightarrow F' = 1$		
-1	0	
0	1	
0.2887	0.2887	
$F = 1 \leftrightarrow F' = 2$		
-1	0	1
0	1	2
0.2887	0.5000	0.7071

Table A.4: $^{133}\text{Ba}^+$ dipole branching ratios: $6S_{1/2} \leftrightarrow 6P_{3/2}, q = +1$

Table A.5: $^{133}\text{Ba}^+$ dipole branching ratios: $6S_{1/2} \leftrightarrow 6P_{3/2}, q = -1$

$6S_{1/2} \leftrightarrow 6P_{3/2}, q = 0$		
$F = 0 \leftrightarrow F' = 1$		
m_F	0	
$m_{F'}$	0	
-0.5774		
$F = 0 \leftrightarrow F' = 2$		
Forbidden		
$F = 1 \leftrightarrow F' = 1$		
-1	0	1
-1	0	1
-0.2887	0	-0.2887
$F = 1 \leftrightarrow F' = 2$		
-1	0	1
-1	0	1
-0.5000	-0.5774	-0.5000

Table A.6: $^{133}\text{Ba}^+$ dipole branching ratios: $6S_{1/2} \leftrightarrow 6P_{3/2}, q = 0$

$6S_{1/2} \leftrightarrow 6P_{1/2}, q = +1$			
$F = 1 \leftrightarrow F' = 1$			
m_F	0	1	
$m_{F'}$	-1	0	
	0.2887	0.2887	
$F = 1 \leftrightarrow F' = 2$			
	-1	0	1
	-2	-1	0
	-0.7071	-0.5000	-0.2887
$F = 2 \leftrightarrow F' = 1$			
	0	1	2
	-1	0	1
	0.2887	0.5000	0.7071
$F = 2 \leftrightarrow F' = 2$			
	-1	0	1
	-2	-1	0
	-0.4082	-0.5000	-0.5000
			-0.4082

$6S_{1/2} \leftrightarrow 6P_{1/2}, q = -1$			
$F = 1 \leftrightarrow F' = 1$			
m_F	-1	0	
$m_{F'}$	0	1	
	-0.2887	-0.2887	
$F = 1 \leftrightarrow F' = 2$			
	-1	0	1
	0	1	2
	-0.2887	-0.5000	-0.7071
$F = 2 \leftrightarrow F' = 1$			
	-2	-1	0
	-1	0	1
	0.7071	0.5000	0.2887
$F = 2 \leftrightarrow F' = 2$			
	-2	-1	0
	-1	0	1
	0.4082	0.5000	0.5000
			0.4082

Table A.7: $^{135}\text{Ba}^+ / ^{137}\text{Ba}^+$ dipole branching ratios: $6S_{1/2} \leftrightarrow 6P_{1/2}, q = +1$ (repeated from page 21) Table A.8: $^{135}\text{Ba}^+ / ^{137}\text{Ba}^+$ dipole branching ratios: $6S_{1/2} \leftrightarrow 6P_{1/2}, q = -1$ (repeated from page 21)

$6S_{1/2} \leftrightarrow 6P_{1/2}, q = 0$				
$F = 1 \leftrightarrow F' = 1$				
m_F	-1	0	1	
$m_{F'}$	-1	0	1	
	0.2887	0	-0.2887	
$F = 1 \leftrightarrow F' = 2$				
	-1	0	1	
	-1	0	1	
	0.5000	0.5774	0.5000	
$F = 2 \leftrightarrow F' = 1$				
	-1	0	1	
	-1	0	1	
	0.5000	0.5774	0.5000	
$F = 2 \leftrightarrow F' = 2$				
	-2	-1	0	1
	-2	-1	0	1
	-0.5774	-0.2887	0	0.2887
				0.5774

Table A.9: $^{135}\text{Ba}^+ / ^{137}\text{Ba}^+$ dipole branching ratios: $6S_{1/2} \leftrightarrow 6P_{1/2}, q = 0$ (repeated from page 22)

$6S_{1/2} \leftrightarrow 6P_{3/2}, q = +1$				
$F = 1 \leftrightarrow F' = 0$				
m_F	1			
$m_{F'}$	0			
0.4082				
$F = 1 \leftrightarrow F' = 1$				
0		1		
-1		0		
-0.4564		-0.4564		
$F = 1 \leftrightarrow F' = 2$				
-1		0		1
-2		-1		0
0.5000		0.3536		0.2041
$F = 1 \leftrightarrow F' = 3$				
Forbidden				
$F = 2 \leftrightarrow F' = 0$				
Forbidden				
$F = 2 \leftrightarrow F' = 1$				
0		1		2
-1		0		1
0.0913		0.1581		0.2236
$F = 2 \leftrightarrow F' = 2$				
-1		0		1
-2		-1		0
-0.2887		-0.3536		-0.3536
				-0.2887
$F = 2 \leftrightarrow F' = 3$				
-2		-1		0
-3		-2		-1
0.7071		0.5774		0.4472
				0.3162
				0.1826

Table A.10: $^{135}\text{Ba}^+ / ^{137}\text{Ba}^+$ dipole branching ratios: $6S_{1/2} \leftrightarrow 6P_{3/2}, q = +1$

$6S_{1/2} \leftrightarrow 6P_{3/2}, q = -1$				
$F = 1 \leftrightarrow F' = 0$				
m_F	-1			
$m_{F'}$	0			
0.4082				
$F = 1 \leftrightarrow F' = 1$				
	-1	0		
	0	1		
	0.4564	0.4564		
$F = 1 \leftrightarrow F' = 2$				
	-1	0	1	
	0	1	2	
	0.2041	0.3536	0.5000	
$F = 1 \leftrightarrow F' = 3$				
Forbidden				
$F = 2 \leftrightarrow F' = 0$				
Forbidden				
$F = 2 \leftrightarrow F' = 1$				
	-2	-1	0	
	-1	0	1	
	0.2236	0.1581	0.0913	
$F = 2 \leftrightarrow F' = 2$				
	-2	-1	0	1
	-1	0	1	2
	0.2887	0.3536	0.3536	0.2887
$F = 2 \leftrightarrow F' = 3$				
	-2	-1	0	1
	-1	0	1	2
	0.1826	0.3162	0.4472	0.5774
			0.7071	

Table A.11: $^{135}\text{Ba}^+ / ^{137}\text{Ba}^+$ dipole branching ratios: $6S_{1/2} \leftrightarrow 6P_{3/2}, q = -1$

$6S_{1/2} \leftrightarrow 6P_{3/2}, q = 0$				
$F = 1 \leftrightarrow F' = 0$				
m_F	0			
$m_{F'}$	0			
0.4082				
$F = 1 \leftrightarrow F' = 1$				
-1	0	1		
-1	0	1		
-0.4564	0	0.4564		
$F = 1 \leftrightarrow F' = 2$				
-1	0	1		
-1	0	1		
-0.3536	-0.4082	-0.3536		
$F = 1 \leftrightarrow F' = 3$				
Forbidden				
$F = 2 \leftrightarrow F' = 0$				
Forbidden				
$F = 2 \leftrightarrow F' = 1$				
-1	0	1		
-1	0	1		
0.1581	0.1826	0.1581		
$F = 2 \leftrightarrow F' = 2$				
-2	-1	0	1	2
-2	-1	0	1	2
-0.4082	-0.2041	0	0.2041	0.4082
$F = 2 \leftrightarrow F' = 3$				
-2	-1	0	1	2
-2	-1	0	1	2
-0.4082	-0.5164	-0.5477	-0.5164	-0.4082

Table A.12: $^{135}\text{Ba}^+ / ^{137}\text{Ba}^+$ dipole branching ratios: $6S_{1/2} \leftrightarrow 6P_{3/2}, q = 0$

A.2 Quadrupole Transition Branching Ratios/Strengths

6S _{1/2} ↔ 5D _{3/2}											
F = 1 ↔ F' = 0											
No Transitions											
F = 1 ↔ F' = 1											
<i>m_F</i>	-1	-1	-1	0	0	0	0	0	1	1	1
<i>m_{F'}</i>	-1	0	1	-1	0	1	-1	0	1	0	1
	-.029	.05	-.071	.05	-.056	.05	-.071	.05	-.029		
F = 1 ↔ F' = 2											
<i>m_F</i>	-1	-1	-1	0	0	0	0	0	1	1	1
<i>m_{F'}</i>	-1	0	1	-2	-1	0	1	2	-1	0	1
	.091	-.112	.112	-.091	-.129	.065	-.065	.129	.091	-.112	.112
											-.091
F = 1 ↔ F' = 3											
<i>m_F</i>	-1	-1	-1	0	0	0	0	0	1	1	1
<i>m_{F'}</i>	-3	-2	-1	0	1	-2	-1	0	1	2	1
	-.224	.183	-.141	.1	-.058	.129	-.163	.173	-.163	.129	-.058
											.1
											-.141
											.183
											-.224
F = 2 ↔ F' = 0											
<i>m_F</i>	-2	-1	0	0	0	1	2				
<i>m_{F'}</i>	0	0	0	0	0	0	0				
	.1	-.1	.1	-.1	.1	-.1	.1				
F = 2 ↔ F' = 1											
<i>m_F</i>	-2	-2	-1	-1	0	0	0	1	1	2	2
<i>m_{F'}</i>	-1	0	-1	0	1	-1	1	-1	0	1	0
	-.095	.134	.116	-.067	-.095	-.116	.116	.095	.067	-.116	-.134
											.095
F = 2 ↔ F' = 2											
<i>m_F</i>	-2	-2	-1	-1	0	0	0	0	1	1	2
<i>m_{F'}</i>	-2	-1	0	1	-2	-1	0	1	2	-1	0
	.1	-.123	.05	-.123	.1	-.05	-.1	.05	.1	-.123	.05
											-.123
											.1
F = 2 ↔ F' = 3											
<i>m_F</i>	-2	-2	-1	-1	0	0	0	0	1	1	2
<i>m_{F'}</i>	-3	-2	-1	0	1	-2	-1	1	2	-1	0
	-.1	-.078	.045	.1	-.063	.089	-.078	-.1	.063	-.063	.1
											.078
											-.045
											.078
											-.1
											.078
											-.1

Table A.15: ¹³⁵Ba⁺/¹³⁷Ba⁺ quadrupole branching ratios: 6S_{1/2} ↔ 5D_{3/2} averaged

$6S_{1/2} \leftrightarrow 5D_{5/2}$												
$F = 1 \leftrightarrow F' = 1$												
m_F	-1	-1	-1	0	0	0	1	1	1	1	1	1
$m_{F'}$	-1	0	1	-1	0	1	-1	0	1	0	1	1
	.071	-.123	.173	-.123	.141	-.123	.173	-.123	.071			
$F = 1 \leftrightarrow F' = 2$												
	-1	-1	-1	0	0	0	1	1	1	1	1	1
	-2	1	0	-2	-1	1	2	-1	0	1	2	2
	-.114	.139	-.139	.114	.161	-.081	.081	-.161	-.114	.139	-.139	.114
$F = 1 \leftrightarrow F' = 3$												
	-1	-1	-1	0	0	0	1	1	1	1	1	1
	-3	-2	-1	0	1	-2	-1	0	1	2	-1	0
	.149	-.122	.094	-.067	.039	-.086	.109	-.116	.109	-.086	.039	-.067
												.094
												-.122
												.149
$F = 1 \leftrightarrow F' = 4$												
Forbidden												
$F = 2 \leftrightarrow F' = 1$												
	-2	-2	-1	-1	0	0	1	1	1	2	2	2
	-1	0	-1	0	1	-1	1	-1	0	1	0	1
	-.026	.037	.032	-.018	-.026	-.032	.032	.026	.018	-.032	-.037	.026
$F = 2 \leftrightarrow F' = 2$												
	-2	-2	-1	-1	0	0	1	1	1	1	1	2
	-2	-1	0	1	-2	-1	0	1	2	-1	0	1
	.054	-.066	.027	-.027	.054	.027	-.054	.027	.054	-.066	.027	-.066
												.054
												-.066
												.054
$F = 2 \leftrightarrow F' = 3$												
	-2	-2	-1	-1	0	0	1	1	1	1	2	2
	-3	-2	-1	0	1	-2	-1	0	1	2	0	1
	-.1	-.078	.045	.1	-.063	.089	-.078	-.1	.078	-.089	.063	-.1
												.078
												-.1
												.1
$F = 2 \leftrightarrow F' = 4$												
	-2	-2	-2	-1	-1	-1	0	0	0	1	1	1
	-4	-3	-2	-1	0	-3	-2	-1	0	-1	0	1
	.183	-.129	.085	-.049	.022	-.129	.138	-.12	.087	-.049	.085	-.12
												.087
												-.12
												.138
												-.129
												.183

Table A.16: $^{135}\text{Ba}^+ / ^{137}\text{Ba}^+$ quadrupole branching ratios: $6S_{1/2} \leftrightarrow 5D_{5/2}$ averaged

$6S_{1/2} \leftrightarrow 5D_{3/2}$				
$\phi = 90^\circ, \gamma = 90^\circ$				
$F = 0 \leftrightarrow F' = 1$				
No Transitions				
$F = 0 \leftrightarrow F' = 2$				
m_F	0	0		
$m_{F'}$	-2	2		
	0.1291	0.1291		
$F = 1 \leftrightarrow F' = 1$				
	-1	1		
	1	-1		
	-0.0913	-0.0913		
$F = 1 \leftrightarrow F' = 2$				
	-1	0	0	1
	1	-2	2	-1
	-0.0527	-0.0745	0.0745	0.0527

Table A.17: $^{133}\text{Ba}^+$ quadrupole branching ratios: $6S_{1/2} \leftrightarrow 5D_{3/2}$ orthogonal orientation

$6S_{1/2} \leftrightarrow 5D_{5/2}$						
$\phi = 90^\circ, \gamma = 90^\circ$						
$F = 0 \leftrightarrow F' = 2$						
m_F	0	0				
$m_{F'}$	-2	2				
	-0.1291	-0.1291				
$F = 0 \leftrightarrow F' = 3$						
Forbidden						
$F = 1 \leftrightarrow F' = 2$						
	-1	0	0	1		
	1	-2	2	-1		
	-0.0351	-0.0497	0.0497	0.0351		
$F = 1 \leftrightarrow F' = 3$						
	-1	-1	0	0	1	1
	-3	1	-2	2	-1	3
	-0.0962	-0.0248	0.0556	0.0556	-0.0248	-0.0962

Table A.18: $^{133}\text{Ba}^+$ quadrupole branching ratios: $6S_{1/2} \leftrightarrow 5D_{5/2}$ orthogonal orientation

$6S_{1/2} \leftrightarrow 5D_{3/2}$								
$\phi = 90^\circ, \gamma = 90^\circ$								
$F = 1 \leftrightarrow F' = 0$								
No Transitions								
$F = 1 \leftrightarrow F' = 1$								
m_F	-1	1						
$m_{F'}$	1	-1						
	-0.0289	-0.0289						
$F = 1 \leftrightarrow F' = 2$								
	-1	0	0	1				
	1	-2	2	-1				
	-0.0373	-0.0527	0.0527	0.0373				
$F = 1 \leftrightarrow F' = 3$								
	-1	-1	0	0	1	1		
	-3	1	-2	2	-1	3		
	-0.0913	-0.0236	0.0527	0.0527	-0.0236	-0.0913		
$F = 2 \leftrightarrow F' = 0$								
	-2	2						
	0	0						
	0.0408	0.0408						
$F = 2 \leftrightarrow F' = 1$								
	-2	-1	1	2				
	0	1	-1	0				
	0.0548	-0.0387	0.0387	-0.0548				
$F = 2 \leftrightarrow F' = 2$								
	-2	-1	0	0	1	2		
	0	1	-2	2	-1	0		
	0.0408	-0.05	0.0408	0.0408	-0.05	0.0408		
$F = 2 \leftrightarrow F' = 3$								
	-2	-1	-1	0	0	1	1	2
	0	-3	1	-2	2	-1	3	0
	0.0183	0.0408	-0.0316	-0.0408	0.0408	0.0316	-0.0408	-0.0183

Table A.19: $^{135}\text{Ba}^+ / ^{137}\text{Ba}^+$ quadrupole branching ratios: $6S_{1/2} \leftrightarrow 5D_{3/2}$ orthogonal orientation

$6S_{1/2} \leftrightarrow 5D_{5/2}$											
$\phi = 90^\circ, \gamma = 90^\circ$											
$F = 1 \leftrightarrow F' = 1$											
	m_F	-1	1								
	$m_{F'}$	1	-1								
		0.0707	0.0707								
$F = 1 \leftrightarrow F' = 2$											
		-1	0	0	1						
		1	-2	2	-1						
		0.0465	0.0657	-0.0657	-0.0465						
$F = 1 \leftrightarrow F' = 3$											
		-1	-1	0	0	1	1				
		-3	1	-2	2	-1	3				
		0.0609	0.0157	-0.0351	-0.0351	0.0157	0.0609				
$F = 1 \leftrightarrow F' = 4$											
Forbidden											
$F = 2 \leftrightarrow F' = 1$											
		-2	-1	1	2						
		0	1	-1	0						
		0.0149	-0.0105	0.0105	-0.0149						
$F = 2 \leftrightarrow F' = 2$											
		-2	-1	0	0	1	2				
		0	1	-2	2	-1	0				
		0.0218	-0.0267	0.0218	0.0218	-0.0267	0.0218				
$F = 2 \leftrightarrow F' = 3$											
		-2	-1	-1	0	0	1	1	2		
		0	-3	1	-2	2	-1	3	0		
		0.0183	0.0408	-0.0316	-0.0408	0.0408	0.0316	-0.0408	-0.0183		
$F = 2 \leftrightarrow F' = 4$											
		-2	-2	-1	-1	0	0	1	1	2	2
		-4	0	-3	1	-2	2	-1	3	0	4
		0.0745	0.0089	-0.0527	-0.0199	0.0345	0.0345	-0.0199	-0.0527	0.0089	0.0745

Table A.20: $^{135}\text{Ba}^+ / ^{137}\text{Ba}^+$ quadrupole branching ratios: $6S_{1/2} \leftrightarrow 5D_{5/2}$ orthogonal orientation

$6S_{1/2} \leftrightarrow 5D_{3/2}$						
$\phi = 90^\circ, \gamma = 90^\circ$						
$F = 0 \leftrightarrow F' = 1$						
No Transitions						
$F = 0 \leftrightarrow F' = 2$						
m_F	0	0	0			
$m_{F'}$	-2	0	2			
	0.0645	0.1581	0.0645			
$F = 1 \leftrightarrow F' = 1$						
	-1	-1	0	1	1	
	-1	1	0	-1	1	
	-0.0456	-0.0456	-0.0913	-0.0456	-0.0456	
$F = 1 \leftrightarrow F' = 2$						
	-1	-1	0	0	1	1
	-1	1	-2	2	-1	1
	-0.0791	-0.0264	-0.0373	0.0373	0.0264	0.0791

Table A.21: $^{133}\text{Ba}^+$ quadrupole branching ratios: $6S_{1/2} \leftrightarrow 5D_{3/2}$ XZ orientation

$6S_{1/2} \leftrightarrow 5D_{5/2}$									
$\phi = 45^\circ, \gamma = 0^\circ$									
$F = 0 \leftrightarrow F' = 2$									
m_F	0	0	0						
$m_{F'}$	-2	0	2						
	-0.0645	-0.1581	-0.0645						
$F = 0 \leftrightarrow F' = 3$									
Forbidden									
$F = 1 \leftrightarrow F' = 2$									
	-1	-1	0	0	1	1			
	-1	1	-2	2	-1	1			
	-0.0527	-0.0176	-0.0248	0.0248	0.0176	0.0527			
$F = 1 \leftrightarrow F' = 3$									
	-1	-1	-1	0	0	0	1	1	1
	-3	-1	1	-2	0	2	-1	1	3
	-0.0481	-0.0745	-0.0124	0.0278	0.0913	0.0278	-0.0124	-0.0745	-0.0481

Table A.22: $^{133}\text{Ba}^+$ quadrupole branching ratios: $6S_{1/2} \leftrightarrow 5D_{5/2}$ XZ orientation

$6S_{1/2} \leftrightarrow 5D_{3/2}$												
$\phi = 45^\circ, \gamma = 0^\circ$												
$F = 1 \leftrightarrow F' = 0$												
No Transitions												
$F = 1 \leftrightarrow F' = 1$												
m_F	-1	-1	0	1	1							
$m_{F'}$	-1	1	0	-1	1							
	-0.0144	-0.0144	-0.0289	-0.0144	-0.0144							
$F = 1 \leftrightarrow F' = 2$												
	-1	-1	0	0	1	1						
	-1	1	-2	2	-1	1						
	-0.0559	-0.0186	-0.0264	0.0264	0.0186	0.0559						
$F = 1 \leftrightarrow F' = 3$												
	-1	-1	-1	0	0	0	1	1	1			
	-3	-1	1	-2	0	2	-1	1	3			
	-0.0456	-0.0707	-0.0118	0.0264	0.0866	0.0264	-0.0118	-0.0707	-0.0456			
$F = 2 \leftrightarrow F' = 0$												
			-2	0	2							
			0	0	0							
			0.0204	0.05	0.0204							
$F = 2 \leftrightarrow F' = 1$												
	-2	-1	-1	1	1	2						
	0	-1	1	-1	1	0						
	0.0274	0.0581	-0.0194	0.0194	-0.0581	-0.0274						
$F = 2 \leftrightarrow F' = 2$												
	-2	-2	-1	-1	0	0	0	1	1	2	2	
	-2	0	-1	1	-2	0	2	-1	1	0	2	
	0.05	0.0204	0.025	-0.025	0.0204	-0.05	0.0204	-0.025	0.025	0.0204	0.05	
$F = 2 \leftrightarrow F' = 3$												
	-2	-2	-1	-1	-1	0	0	1	1	1	2	2
	-2	0	-3	-1	1	-2	2	-1	1	3	0	2
	0.05	0.0091	0.0204	-0.0316	-0.0158	-0.0204	0.0204	0.0158	0.0316	-0.0204	-0.0091	-0.05

Table A.23: $^{135}\text{Ba}^+ / ^{137}\text{Ba}^+$ quadrupole branching ratios: $6S_{1/2} \leftrightarrow 5D_{3/2}$ XZ orientation

$6S_{1/2} \leftrightarrow 5D_{5/2}$										
$\phi = 45^\circ, \gamma = 0^\circ$										
$F = 1 \leftrightarrow F' = 1$										
m_F	-1	-1	0	1	1	1				
$m_{F'}$	-1	1	0	-1	1					
	0.0354	0.0354	0.0707	0.0354	0.0354					
$F = 1 \leftrightarrow F' = 2$										
	-1	-1	0	0	1	1				
	-1	1	-2	2	-1	1				
	0.0697	0.0232	0.0329	-0.0329	-0.0232	-0.0697				
$F = 1 \leftrightarrow F' = 3$										
	-1	-1	0	0	1	1	1			
	-3	1	-2	0	2	-1	1	3		
	0.0304	0.0471	0.0079	-0.0176	-0.0577	-0.0176	0.0079	0.0471	0.0304	
$F = 1 \leftrightarrow F' = 4$										
Forbidden										
$F = 2 \leftrightarrow F' = 1$										
	-2	-1	-1	1	1	1	2			
	0	-1	1	-1	1	0				
	0.0075	0.0158	-0.0053	0.0053	-0.0158	-0.0075				
$F = 2 \leftrightarrow F' = 2$										
	-2	-1	0	0	1	1	2	2		
	-2	1	-2	0	2	-1	1	0	2	
	0.0267	0.0109	0.0109	-0.0267	0.0109	-0.0134	0.0134	0.0109	0.0267	
$F = 2 \leftrightarrow F' = 3$										
	-2	-1	-1	0	0	1	1	2	2	
	-2	0	-3	1	-2	2	-1	3	0	2
	0.05	0.0091	0.0204	-0.0316	-0.0204	0.0204	0.0158	0.0316	-0.0204	-0.0091
										-0.05
$F = 2 \leftrightarrow F' = 4$										
	-2	-2	-1	-1	0	0	1	1	2	2
	-2	0	-3	-1	1	-2	2	-1	3	0
	0.0373	0.0423	0.0045	-0.0264	-0.0598	-0.01	0.0173	0.0655	0.0173	-0.01
										-0.0598
										-0.0264
										0.0045
										0.0423
										0.0373

Table A.24: $^{135}\text{Ba}^+ / ^{137}\text{Ba}^+$ quadrupole branching ratios: $6S_{1/2} \leftrightarrow 5D_{5/2}$ XZ orientation (repeated from page 27)